Galaxies **2014**, *2*, 300-381; doi:10.3390/galaxies2030300

OPEN ACCESS

galaxies

ISSN 2075-4434

www.mdpi.com/journal/galaxies

Review

Monolithic View of Galaxy Formation and Evolution

Cesare Chiosi [1,*], Emiliano Merlin [1,2], Lorenzo Piovan [1] and Rosaria Tantalo [1]

[1] Department of Physics & Astronomy, University of Padua, Vicolo Osservatorio 2, Padua 35122, Italy; E-Mails: emiliano.merlin@oa-roma.inaf.it (E.M.); lorenzo.piovan@gmail.com (L.P.); rosaria.tantalo@unipd.it (R.T.)

[2] National Institute for Astrophysics (INAF), Astronomical Observatory of Rome, Via Frascati 33, Monte Porzio Catone (RM) 00040, Italy

* Author to whom correspondence should be addressed; E-Mail: cesare.chiosi@unipd.it; Tel.: +39-049-827-8220; Fax: +39-049-827-8212.

Received: 4 March 2014; in revised form: 19 May 2014 / Accepted: 27 May 2014 / Published: 14 July 2014

Abstract: We review and critically discuss the current understanding of galaxy formation and evolution limited to Early Type Galaxies (ETGs) as inferred from the observational data and briefly contrast the hierarchical and quasi-monolithic paradigms of formation and evolution. Since in Cold Dark Matter (CDM) cosmogony small scale structures typically collapse early and form low-mass haloes that subsequently can merge to assembly larger haloes, galaxies formed in the gravitational potential well of a halo are also expected to merge thus assembling their mass hierarchically. Mergers should occur all over the Hubble time and large mass galaxies should be in place only recently. However, recent observations of high redshift galaxies tell a different story: massive ETGs are already in place at high redshift. To this aim, we propose here a revision of the quasi-monolithic scenario as an alternative to the hierarchical one, in which mass assembling should occur in early stages of a galaxy lifetime and present recent models of ETGs made of Dark and Baryonic Matter in a Λ-CDM Universe that obey the latter scheme. The galaxies are followed from the detachment from the linear regime and Hubble flow at $z \geq 20$ down to the stage of nearly complete assembly of the stellar content ($z \sim 2-1$) and beyond. It is found that the total mass ($M_h = M_{DM} + M_{BM}$) and/or initial over-density of the proto-galaxy drive the subsequent star formation histories (SFH). Massive galaxies ($M_h \simeq 10^{12} M_{\odot}$) experience a single, intense burst of star formation (with rates $\geq 10^3 M_{\odot}$/yr) at early epochs, consistently with observations, with a weak dependence on the initial over-density; intermediate mass haloes ($M_h \simeq 10^{10} - 10^{11} M_{\odot}$) have star formation histories that strongly depend on their

initial over-density; finally, low mass haloes ($M_h \simeq 10^9 M_\odot$) always have erratic, burst-like star forming histories. The present-day properties (morphology, structure, chemistry and photometry) of the model galaxies closely resemble those of the real galaxies. In this context, we also try to cast light on the physical causes of the Stellar Mass-Radius Relation (MRR) of galaxies. The MRR is the result of two complementary mechanisms: *i.e.*, local physical processes that fix the stellar mass and the radius of each galaxy and cosmological global, statistical principles, which shape the distribution of galaxies in the MR-plane. Finally, we also briefly comment on the spectro-photometric properties of the model galaxies and how nicely they match the observational data. The picture emerging from this analysis is that the initial physical conditions of a proto-galaxy, *i.e.*, *nature*, seem to play the dominant role in building up the ETGs we see today, whereas *nurture* by recurrent captures of small objects is a secondary actor of the fascinating and intriguing story of galaxy formation and evolution.

Keywords: observational data; early types; formation and evolution; mass-radius relation

1. Introduction

In a Universe containing three main components in cosmic proportions: Dark Energy (DE, 70%), Dark Matter (DM, 25%), and Baryonic Matter + Neutrinos (BM, 5%), the formation and evolution of galaxies are among the hot topics of modern astrophysics. In brief the classical paradigm of galaxy formation (the Early Type Galaxies (ETGs), in particular) stands on the following prescription: the above composition of the Universe, the hierarchical clustering of DM + BM from small size bodies to large complexes under the action of gravity, hierarchical mergers of DM + BM haloes to form "visible galaxies" all over the Hubble time, according to which massive galaxies are the end product of repeated mergers and are in place only at rather recent times. However, the observational data are currently telling us a more complicated history because massive galaxies with mass of the order of $10^{12}\ M_\odot$ are detected at high redshift ($z \geq 5$). Over the years two competing scenarios for galaxy formation have been proposed, both of which with a number of possible variants:

Hierarchical: massive ETGs are the end product of subsequent mergers of smaller sub-units over time scales almost equal to the Hubble time. Complementary alternatives to this simple scheme are the *Dry Mergers* (fusion of gas-free galaxies to avoid star formation) and the *Wet Mergers* (the same but with some stellar activity).

Monolithic: massive ETGs form at high redshift by rapid collapse and undergo a single, prominent star formation episode, ever since followed by quiescence. Over the years this view has been changed to the *Revised Monolithic* scheme: a great deal of the stars in massive ETGs are formed very early-on at high redshifts and the remaining ones at lower redshifts.

For long time, the preference has gone to the hierarchical scheme that was considered the reference frame for any theory of ETGs formation (the massive ones in particular). The success of this theory is mainly due to the achievements obtained in modeling the large scale gravitational structures like the

large scale structure of the Universe itself, galaxy groups, and galaxy clusters. However its extension to individual galaxies is still a matter of debate and often in conflict with modern observational data. To cope with the difficulties encountered by the classical hierarchical models, in the following we will introduce a new scheme named *Early Hierarchical Quasi Monolithic*, in which a great deal of mass assembly by rapid collapse and star formation occurs in the earliest epochs. In any case, both are complete by redshift $z = 1$. From now on the galaxies behave like monolithic objects. Therefore, in this review we concentrate on the models obtained with the early hierarchical quasi monolithic scheme by [1] and shortly report on how they are able to reproduce current observational data for ETGs.

The plan of the review is as follows: In Section 2, we briefly present some observational clues on the past history of galaxy formation and evolution and the fossil records of it in the chemo-spectro-photometric properties of the stellar populations, we touch upon the issue of scale relationships with particular attention to the Fundamental Plane, enlighten the properties of ETGs from the local Universe to high redshifts. These are considered as basic constraints that should be matched by any model of galaxy formation and evolution. In Section 3 we briefly review the current models of galaxy formation and companion numerical techniques. We briefly touch upon the successes and failures of the hierarchical view of galaxy formation in cosmological context. In Section 4 we set the scene for the early hierarchical, quasi monolithic view (initial conditions out of the cosmological tissue, the prescription for star formation and physical description of the interstellar medium), present the main results from recent numerical simulations of model galaxies, *i.e.*, the histories of star formation in relation to the initial total mass and over-density, the mass assembly of the whole systems, the age and metallicity distribution of the stellar populations, the gradients in metallicity, the occurrence and efficiency of galactic winds, and finally the mass-density profiles of the present-day galaxies. In Section 5 we highlight the physical origin of the MRR, present some simulations of this, and discuss some possible implications. Finally, in Section 6 we apply the spectro-photometric synthesis technique to the model galaxies and compare the theoretical magnitudes and colours to those of real galaxies in the nearby Universe and as function of the redshift. Finally, we present a preliminary comparison of the theoretical fit of the Kormendy relation. Finally, in Section 7 we draw some conclusions.

2. Observational Clues on the Galaxy Formation History

Before describing our galaxy models, we like to recall that any theory of galaxy formation and evolution must obey two different groups of constraints, *i.e.*, those provided by the Scale Relations and the pattern of properties of the Stellar Content of the galaxies. Indeed, the body of observational data acquired over the years helps us to infer the past histories of star formation, chemical enrichment, and mass assembly of galaxies of different morphological type. In some way, the kind of star formation occurring in ETGs depends on their initial total mass and density. It is early, short and intense in massive (and high density) ETGs and long, less efficient, and perhaps in bursts, in the low-mass (and low-density) ones. The key question to address and answer is: under which physical conditions either a single prominent episode or several episodes of star formations occur? Which model does best explain the whole pattern of observational data for ETGs? The hierarchical or the monolithic one? Or a complex combination of the two? To cast light on this issue, we will make use of numerical galaxy

models calculated with the so-called NB-TSPH technique (to be shortly described below) that start from realistic initial conditions derived from simulations of the primordial tissue of the Universe in the Λ-CDM Cosmology (*i.e.*, Cold Dark Matter Universe with cosmological constant Λ) and include accurate treatments of important physical processes such as star formation, heating by energy deposit from supernova explosions and stellar winds, cooling by radiative processes, and chemical enrichment.

To highlight the above issues, it is perhaps wise to review a few key observational points that need an explanation, possibly a coherent one for all of them. We present them in order of increasing complexity.

2.1. The G-Dwarf Analog

The near ultra-violet (UV) spectrum of ETGs shows that the relative percentage of old metal poor stars is small, thus indicating that the metallicity partition function N(Z), *i.e.*, number of stars per metallicity bin, cannot be the one predicted by the closed box scheme, but ought to resemble those of infall or prompt enrichment [2–4]. This is the analog of the G-Dwarf problem in the solar vicinity. It bears very much on the mechanism and timescale of galaxy formation.

2.2. The UV-Excess

All ETGs have detectable fluxes short-ward of 2000 Å. Measured by the color (1550-V) the flux correlates with Mg_2 and velocity dispersion [5]. This flux has a typical source with Teff of about 25,000 K and little percentages from above 30,000 K and below 20,000 K [6,7]. Reference [2] identified the source with the Asymptotic Giant Branch (AGB) manqué stars of high metallicity and also noted that a small percentage of high metallicity stars ($Z > 3 - 4Z_{\odot}$) can produce the right amount of flux. As the metallicity of ETGs is expected to increase with the mass, the above relations can be explained.

2.3. Enhancement of α-Elements: [X_{α}/Fe]

Absorption-line indices like Mg_2 and $[\mathrm{MgFe}]$ measured in the stellar content of galaxies (mainly ETGs) seem to vary with the position in a galaxy (see [8–11]) and from galaxy to galaxy [12–14]. Looking at the correlation between Mg_2 and $\langle\mathrm{Fe}\rangle$ (or similar indices) for ETGs, Mg_2 increases faster than $\langle\mathrm{Fe}\rangle$ which is interpreted as due to the enhancement of α-elements. Since the classical paper by [5], the index Mg_2 is also known to increase with the velocity dispersion (and hence mass and luminosity) of the galaxy. Based on the body of data for different indices, Mg_2, $[\mathrm{MgFe}]$, $\langle\mathrm{Fe}\rangle$ and others, the internal gradients and the difference in the central values from galaxy to galaxy, the conviction arose that the degree of enhancement in α-elements ought to increase both moving toward the center of a galaxy, and passing from dwarf to massive ETGs [15–19]. These findings strongly affect the theory of galaxy formation. Recalling that Fe comes from both Type Ia and Type II SNe, whereas α-elements (O, Mg, *etc.*) are mainly generated by the short lived Type II SNe (see [20], and references therein for a thorough discussion of the expected frequency of Type Ia and II SNe), those observational trends could imply (i) a different number ratio between Type Ia and II SNe, (ii) different time scales of star formation, (iii) different degrees of pre-enrichment. The most plausible explanation of the observed trend in the [α/Fe]-mass relationship is that the total duration of the star forming activity in a galaxy should decrease

both going toward the center (gradients in the star formation activity) and with the galaxy mass. This view is in contrast with the current interpretation of the Color-Magnitude Relation (CMR) in terms of the SNa driven galactic wind model by [21,22] and the correlation with the velocity dispersion, both requiring that the star formation time-scale should get longer at decreasing galaxy mass. The issues have been amply discussed by [23] to whom we refer. The subject has been examined in detail by [24] using the NB-TSPH models of ETGs by [23]. Consider two ETGs of total (DM + BM) mass equal to $1\times10^{9}\ M_{\odot}$ (bursting mode of star formation) and $1\times10^{12}\ M_{\odot}$ (prominent initial episode of star formation followed by nearly quiescence). Soon after star formation began, the ratio [O/Fe] first suddenly increases then falls down leveling off to the typical value set by the first Type II SNe. Subsequent star formation does not alter the ratio too much, it gently falls below zero over a long time scale, several Gyrs. This analysis provides also an explanation of the Mg_2 *vs.* σ (velocity dispersion) relationship as a side product. Reference [24] find that it depends more on the metallicity (say about 75%) and less on the degree of α-enhancement (remaining 25%), see also [25] for similar conclusion.

2.4. Colour-Magnitude Relation

Cluster ETGs get redder with increasing luminosity, mass, velocity dispersion [21,22,26–28]. The CMR is tight for cluster ETGs [27,28], whereas it is more dispersed for nearby field ETGs and those in small Groups [29]. The CMR is conventionally interpreted as a mass-metallicity sequence [30–32]: massive galaxies reach higher mean metallicities than the less massive ones. Long ago [21,22] proposed the galactic wind model: star formation is longer in massive ETGs, more metals are made, and the color is redder, whereas is shorter in the low mass ones. The opposite of what is required by the [α/Fe] problem! The tightness of the CMR implies for a given Hubble time (and lack of a coordination mechanism) that ETGs are old, around 13 Gyr, and nearly coeval [27,28]. The alternative that the CMR is an age sequence, with bluer galaxies younger than red ones, has been proved not to be viable by [33]. The CMR for field ETGs is more dispersed, perhaps compatible with SFs spread over long periods of time, and changing from galaxy to galaxy [29]. Mergers are compatible with all this.

2.5. Ages, Metallicities, [α/Fe], and SFHs of Field and Cluster Galaxies from Absorption Line Indices

2.5.1. Methodology, Diagnostics and Uncertainties

Over the years, many attempts have been made to infer ages, metallicities and the degree of enhancement in α-elements by means of the so-called Lick system of absorption-line indices first developed by [16,34–38]. It was originally designed to infer the age and the metallicity of stellar systems, the ETGs in particular. The Lick indices seem to have the potential of partially resolving the long known age-metallicity degeneracy affecting the spectral energy distribution of stellar populations [39] (An old metal-poor stellar population may happen to have the same spectral energy distribution as a young metal-rich one). In a few occasions they have been integrated by other broad-band colours over a wide range of wavelengths, including the far UV—e.g., (1550-V), the signature of the (UV)-excess in ETGs, and/or velocity dispersion σ (e.g., [40,41]). Thanks to it, the Lick system of indices has been extensively used and improved by many authors [13,14,40,42–57]. The main result of all those studies is that, even

in ETGs, some recent episodes of star formation should have occurred to explain the large scatter in the observational data for indices like H_β (more sensitive to age). The problem is, however, complicated further by the enhancement of α-elements, which imposes that the ages and metallicities of ETGs should be derived from indices taking this parameter into account. As noticed long ago by [37,58], indices for α-enhanced chemical mixtures of a given total metallicity are expected to differ from those of the standard case. On one hand, this spurred new generations of stellar models, isochrones, and Single Stellar Populations (SSPs) with α-enhanced mixtures [59] and, on the other hand, led to many increasingly complex attempts to simultaneously derive the age, metallicity, and degree of enhancement by fitting the observational indices to their theoretical counterparts [13,14,42,53–57]. The formal solution for ages, metallicities, and $[\alpha/Fe]$ ratios based on large samples of galaxies, e.g., the [60] list, once more yields a wide range of ages, metallicities, and abundance ratios, as amply discussed by [57]. Although the picture emerging from the above studies is a convincing one, there are still several points of weakness intrinsic to even the state-of-the-art theoretical indices that have spurred a severe revision of the whole issue, *i.e.*, (i) the foundations of the Lick indices; (ii) the various steps that are required to derive theoretical indices and their dependence on age, metallicity, and degree of enhancement; (iii) the current method of estimating these parameters from the indices; (iv) and, finally, few points of controversy among different groups. The original Lick indices coded the information contained in the stellar spectra, effective temperature, gravity and chemical composition ($\log T_e$, $\log g$, and $[\mathrm{Fe/H}]$, respectively) for a sample of nearby stars thus not encompassing the whole range of possible values. Furthermore the spectra in use had a fixed (and modest) resolution (8.4 Å), often much different from the resolution of theoretical spectra. To cope with all this, [16,38] introduced the concept of Fitting Functions ($\mathcal{FF}$s): the indices for the above reference stars are measured and expressed as empirical fits of the parameters $\log T_e$, $\log g$, and $[Fe/H]$, *i.e.*, the $\mathcal{FF}$s, which, needless to say, inherit the same limitations in parameter coverage of the reference stars. Therefore, many attempts have been made to collect data for a very large interval of the atmospheric parameters, e.g., [61–64]. Despite the α-enhancement problem has been known from long time, the reference stellar spectra and associated $\mathcal{FF}$s [37] did not allow for non-standard abundance ratios in the chemical composition. Passing now from individual stars to large assemblies of stars (clusters and galaxies), which are reduced to single stellar populations (SSPs) and manifolds of SSPs, respectively, the derivation of theoretical indices (and spectra, magnitudes, and broad-band colours) is even more complicated because other ingredients intervene: (i) the construction of realistic isochrones for SSPs including all evolutionary phases, even the unusual ones that are known to appear at very high metallicities (see [2,57]); (ii) the initial mass function of stars in each generation; (iii) the method to calculate the indices for a SSP starting from the indices of the individual component stars. Two different procedures can be found in literature: the direct synthesis star-by-star adopted by [57] and the so-called synthesis by phases adopted by [53]. Although the final results are not strictly equal, both methods can be considered as equivalent (see [53,57,65], for more details); (iv) and finally, in the case of galaxies, the past history of star formation and chemical enrichment weighing the contribution from stellar populations of different ages and chemical compositions (see e.g., [2], for all details). It is worth noting here that galaxy indices are almost always compared to SSP indices, thus neglecting the mix of stellar populations and missing important contributions from some peculiar components. For instance an old SSP of very high metallicity and/or a very old SSP of

extremely low metal content would possess strong H_β thus mimicking a young SSP of normal metallicity (see [57], for more details). Integrated indices for model galaxies have been occasionally calculated and used [43], but never systematically applied to this kind of analysis. This is a point that should be carefully investigated and kept in mind when comparing data with theory. If for solar abundance ratios the dependence of the indices on age and metallicity is currently on rather solid ground except for the effect of some unusual phases of stellar evolution, the same does not happen for non-solar abundance ratios, because of several points of controversy:

(i) First of all, the definition of enhancement in α-elements is not unique. It can be done at constant Hydrogen (X_H), Helium (X_{He}) and total metallicity Z (abundances in mass according to our notation here), and only the relative mass proportions of several α-elements with respect to Fe are varied, but their sum $\sum_j X_j = 1$ is kept constant. According to [66] the "total enhancement factor" is $\Gamma_Z = -\log\left(\frac{X'_{\rm Fe}}{X^{\odot}_{\rm Fe}}\right)$ (often simply indicated as Γ). Alternatively, the abundance of some elements heavier than Helium are varied with respect to Fe, $[X_\alpha/X_{Fe}]$ in the usual notation, the new total metallicity is derived $Z = \sum_{j>He} X_j$, and the abundances X_H and X_{He} are adjusted to match the condition $\sum_j X_j = 1$ where now j runs from H to heavy elements. In this case, the definition of "total enhancement factor" is $\Gamma_\alpha = \left[\frac{\sum X_i^{\alpha,\rm enh}}{\sum X_j^{\alpha}}\right]$ [66,67]. The issue has been widely discussed by [66,68] to whom we refer for all details. Suffice it to mention here that with the first definition (constant metallicity), indices can be simply compared for solar scaled and α-enhanced mixtures with the same Z. With the second one, for any degree of enhancement we have to establish a priori the corresponding total metallicity before making the above comparison. For the sake of illustration, let us compare the case of solar composition [$X = 0.7347$, $Y = 0.248$, $Z = 0.0170$] and solar pattern of abundances to the one in which the abundances of some heavy elements (C, N, O, *etc.*) are enhanced by +0.4 dex. Due to the effect of enhancement, the new chemical parameters become [$X = 0.7219$, $Y = 0.244$, $Z = 0.0340$]: the metallicity is almost doubled and the abundances of H and He are slightly decreased. It is worth noting that this relationship changes with the degree of enhancement. This is a point to keep in mind when comparing results from different authors and those obtained with the definition of enhancement at constant metallicity.

(ii) Very often the $\mathcal{FF}$s do not include the effect of α-enhancement or do it only for a small range of values of the enhancement parameter or a few indices. To cope with it, reference [69] introduced the so-called Response Functions, $\mathcal{RF}$s. In brief, they calculated the reference indices I_0 for the solar abundance ratios, and separately doubling the abundance X_i of a number of selected and important elements (C, N, O, Mg, Fe, Ca, Na, Si, Cr, and Ti) in steps of $\Delta[X_i/\rm H] = 0.3$ dex, derived the variation $\Delta I = I_{\rm enh} - I_0$ in units of the observational error σ_0. The generic $\mathcal{RF}$ to be used for arbitrary variations $\Delta[X_i/\rm H]$ is $\rm R_{0.3}(X_i) = \frac{1}{I_0}\frac{\Delta I}{\Delta[X_i/H]}0.3$. Using the [69] values for $\mathcal{RF}$s, references [13,54,57] transformed indices with solar abundance ratios into those for enhanced α-elements by means of two different algorithms. References [13,57] propose that the fractional variation of an index due to changes in the chemical parameters is $\frac{\Delta I}{I} = \left\{\prod_i [1 + \rm R_{0.3}(X_i)]^{\frac{[X_i/H]}{0.3}}\right\} - 1$, where $\rm R_{0.3}(X_i)$ are the $\mathcal{RF}$s we have defined above. A different reasoning was followed by [54] who found $\frac{\Delta I}{I} = \left\{\prod_i exp\left(\rm R_{0.3}(X_i)\right)^{\frac{[X_i/H]}{0.3}}\right\} - 1$. Although the two relations may look similar, actually they are not. This topic has been thoroughly discussed in [57,65] to whom the reader should refer for all details. The use of these relations has generated different and highly controversial results for some

indices, H_β in particular, under unusual enhancements in some elements. The issue can be reduced to the statement: does H_β increase (significantly) with [α/Fe] or not? Or, even worse, does it decrease with it? The question is not trivial because any effect of α-enhancement on indices like H_β would reflect onto the age determination. A galaxy with high H_β could be an object with solar partition of elements and recent star formation or an object with α-enhanced chemical composition and old stellar content (see [57,65,66,68]) and Section 2.5.5 below).

(iii) High-resolution synthetic spectra for stars with a good coverage of gravity, effective temperature, chemical composition, and degree of enhancement in α-element can greatly alleviate the above difficulties and shed light on these important issues. In principle, indices can be straightforwardly calculated from the spectra with no need of $\mathcal{FF}$s, $\mathcal{RF}$s, and suitable algorithms to take the α-element enhancement into account. The task has been undertaken by [66,68] who have generated synthetic absorption-line indices on the Lick system based on the recent library of 1- Å resolution spectra calculated by [70] over a large range of atmospheric parameters ($\log T_{\rm eff}$, $\log g$ and [Fe/H]) and both for solar and α-enhanced abundance ratios in the chemical composition. The main results of this study are: (a) A modern version of the $\mathcal{RF}$s of [69] which have been determined for wide ranges of $\log T_{\rm eff}$, $\log g$ and [Fe/H] (or $[{\rm Z}/{\rm Z}_\odot]$). Not only the $\mathcal{RF}$s vary with the type of star but also with the metallicity. The effect of metallicity is important and cannot be neglected; (b) SSP indices calculated with the new $\mathcal{RF}$s (and the $\mathcal{FF}$s of [16,38]) clearly demonstrate that not only all indices depend on the enhancement but also that H_β increases with it as already anticipated by [57]; (c) These results lend support to the suggestion made by [65] that in the H_β *versus* [MgFe] plane (and similar) galaxies with $1 < H_\beta < 1.6$, whose scatter in H_β is customarily due to age (and metallicity), could be indeed old objects of the same age (say 13 Gyr) that scatter in H_β because of differences in metallicity and enhancement from galaxy to galaxy likely caused by their individual star formation history. Only occasionally, especially for the strong H_β galaxies, more recent episodes of star formation ought to be invoked.

2.5.2. Gradients in Age, Metallicity and [α/Fe] Across Individual Galaxies

Systematic variations in the line strength indices H_β, Mg_2, and $\langle Fe\rangle$ are observed across ETGs and limited to the nuclear region from galaxy to galaxy. Furthermore, since the gradients in Mg_2 and $\langle Fe\rangle$ have often different slopes arguments are given for an enhancement of Mg (α-elements in general) with respect to Fe toward the center of these galaxies. Finally, the inferred degree of enhancement seems to increase passing from dwarfs to massive ETGs. The ability of the H_β, Mg_2 and $\langle Fe\rangle$ diagnostics to assess the metallicity, [Mg/Fe] ratios, and ages of the stellar content of ETGs has been the subject of many studies. Reference [42] first provided basic calibrations for the variations δH_β, δMg_2 and $\delta\langle Fe\rangle$ as a function of variation in age $\Delta\log(t)$, metallicity $\Delta\log({\rm Z}/{\rm Z}_\odot)$, and $\Delta[{\rm Mg}/{\rm Fe}]$ and examined the gradients observed in a small sample of galaxies (six objects in total). They analyzed how the difference δH_β, δMg_2, and $\delta\langle Fe\rangle$ between the external and central values of each index translates into $\Delta[{\rm Mg}/{\rm Fe}]$, $\Delta\log({\rm Z}/{\rm Z}_\odot)$, and $\Delta\log(t)$. The situation is shown in the panels of Figure 1. Out of six galaxies under examination, four have the nuclear region more metal-rich, more enhanced in α-elements, and younger (*i.e.*, containing a significant fraction of stars of relatively young age) than the external

regions. In contrast the remaining two galaxies have the nuclear region more metal-rich, more enhanced in α-elements but marginally older than the external zones.

Figure 1. (**a**) The $\delta\langle\mathrm{Fe}\rangle$ *versus* $\delta\mathrm{Mg}_2$ relation across individual galaxies. The three arrows centered on (0,0) indicate the *age, metallicity, and enhancement vectors* as indicated. Along the age vector, the age goes from 5 to 15 Gyr, along the metallicity vector Z ranges from 0.004 to 0.05, and along the enhancement vector [Mg/Fe] goes from -0.3 to 0.4 dex. The data are from [71] for NGC 4594, from [72] for NGC 4472, and from [10] for NGC 2434 and NGC 3706; (**b**) The same as in the Left Panel but for the $\delta\mathrm{H}_\beta$ *versus* $\delta\mathrm{Mg}_2$ relation. (Reproduced with permission from [42]. Copyright 1998 Astronomy and Astrophysics).

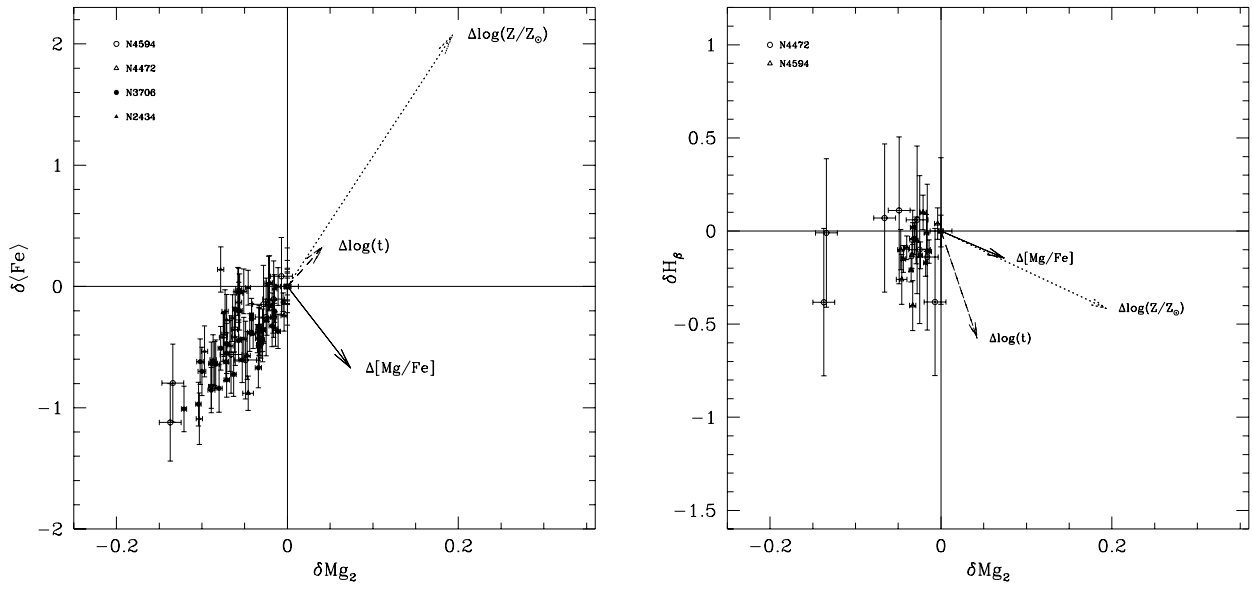

(**a**) (**b**)

Reference [42] also looked at the variations from galaxy to galaxy of the nuclear values of H_β, Mg_2, and $\langle\mathrm{Fe}\rangle$ limited to a sub-sample of the [12] list. The differences $\delta\mathrm{H}_\beta$, $\delta\mathrm{Mg}_2$, and $\delta\langle\mathrm{Fe}\rangle$ were converted into the differences $\Delta\log(\mathrm{t})$, $\Delta\log(\mathrm{Z}/\mathrm{Z}_\odot)$, and $\Delta[\mathrm{Mg}/\mathrm{Fe}]$. Various correlations among the age, metallicity, and enhancement variations were explored. In particular they thoroughly examined the relationships $\Delta\log(\mathrm{t}) - \mathrm{M_V}$, $\Delta\log(\mathrm{Z}/\mathrm{Z}_\odot) - \mathrm{M_V}$, and $\Delta[\mathrm{Mg}/\mathrm{Fe}] - \mathrm{M_V}$, where the absolute magnitude M_V was considered as a loose indicator of the galaxy mass. The correlations are shown in the three panels of Figure 2. It is found that a sort of age limit is likely to exist in the $\Delta\log(\mathrm{t}) - \mathrm{M_V}$ plane, traced by galaxies with mild or no sign of rejuvenation (in other words with no obvious signs of mergers and or interactions). In these objects, the duration of the star forming activity is likely to have increased at decreasing galactic mass. Limited to these galaxies, the mass-metallicity sequence implied by the CMR is recovered (see [40], and Section 2.5.3 below for a discussion of this issue), likewise for the α-enhancement-luminosity relation suggested by the gradients in Mg_2 and $\langle\mathrm{Fe}\rangle$. For the remaining galaxies the situation is more intriguing: sporadic episodes of star formations are likely to have occurred scattering the galaxies in the space of the age, metallicity, and [Mg/Fe]. The results are discussed with regard to predictions from the merger and isolation models of galaxy formation and evolution

highlighting points of difficulty with each scheme. Finally, the suggestion is advanced that in massive ETGs the Initial Mass Function (IMF) of the typical stellar populations at early epochs was skewed toward the massive stars, the opposite in the low mass ETGs [42,73]. This systematic change of the IMF slope with the galaxy mass might alleviate some of the difficulties encountered by the standard SN-driven galactic wind model and lead to a coherent interpretation of the data. Finally, limited to a handful of objects for which all necessary information is available, it seems that the SF process lasted longer in the centre than in the external regions [40,42].

2.5.3. Passing from Galaxy to Galaxy: The Two-Indices Diagnostics

The two-indices plane H_β *versus* [MgFe] displayed in panels (a0 and (b) of Figure 3 show the sample of normal galaxies by [12] and that of pair and shell galaxies by [74] in which some evidence of dynamical interaction is found. The two groups of galaxies show the same behaviour (the issue will be widely discussed in Section 2.6). Diagnostic planes like this are customarily used to infer the age, metallicity and degree of enhancement (see [57]) of ETGs by comparing the data with their theoretical counterparts. The technique in use is the so-called "Minimum Distance Method": as a galaxy corresponds to a point in this plane, the theoretical values of age, metallicity, (and Γ_α or Γ_Z), are given by the node of the underlying grid closest to it (see [57], for all details). There is an important issue to be clarified. Considering that the age of the Universe provided by WMAP (Wilkinson Microwave Anisotropy Probe) is 13.7 ± 0.2 Gyr [75], a significant number of galaxies fall below the 13 Gyr age-line even for the solar-scaled compositions (no enhancement in α-elements). There are several reasons for the observational H_β being too low compared to the theoretical expectation. First obvious observational uncertainties, second incompleteness of stellar models and isochrones, third strong contamination by emission in particular for H_β (it is worth recalling that the data under consideration have already been corrected for emission), e.g., [76] who have reported the presence of faint equivalent width as low as $\sim 0.1 - 1$ Å) nebular emission embedded in H_β absorption profiles. Observational errors are estimated to amount to $\Delta \mathrm{H}_\beta \pm 0.22$ and $\Delta[\mathrm{MgFe}] \pm 0.17$. Accuracy and completeness of stellar models have been examined in detail by [57] to whom the reader should refer. Emission, customarily not included in theoretical indices, is by far more uncertain to quantify. To reconcile things, the correction already applied by [60], the mean value of which amounts to about 0.1 Å, should be increased to about 0.2 Å. However, instead of arbitrarily changing the data, we prefer to drop from the sample all galaxies whose H_β falls below a suitable limit (see also the dashed line shown in the left panel of Figure 4 below). It is implicitly assumed that owing to the observational uncertainty the data for the remaining galaxies are not in conflict with the theoretical expectation.

Looking at the position of ETGs in various diagnostic planes in literature (these however are not always with the same degree of accuracy in the stellar input of the indices modelling: stellar models, isochrones, spectral libraries, inclusion and definition of α-enhancement and other details too specific to be touched upon here) the following scenario was soon evident:

Figure 2. (**a**) The $\Delta\log(\mathrm{t})$ *versus* $\mathrm{M_V}$ relation. Filled circles are the galaxies defining the age limit (*i.e.*, those with no sign of dynamical rejuvenation, see the text for details), the heavy stars are the three galaxies of this group belonging to the Virgo cluster, and the open circles are all remaining galaxies. The *eye drawn long-dashed-dotted line* is only meant to visualize the age limit. Finally, the position of M32, NGC 4649 is indicated. Superposed to this diagram are the fading lines of SSPs: the thin dotted and solid lines are for $Z = 0.004$ and $Z = 0.05$, respectively; each dot along the lines marks the age in step of 1 Gyr starting from 20 Gyr (top) down to 4 Gyr (bottom); the thin horizontal lines locate the loci of constant age (20, 15, 10, 7, and 5 Gyr starting from the top). Finally, the fading lines of SSP (in pairs because of the different metallicity) are shown for different values of the total mass, namely 10^{12}, 10^{11}, 10^{10}, 10^{9}, and $10^{8} \times \mathrm{M_\odot}$ from right to left; (**b**) The $\Delta\log(\mathrm{Z/Z_\odot})$ *versus* $\mathrm{M_V}$ relation. The *thick dashed line* is the linear regression of the results. All other symbols are as in the Top Left Panel. The position of M32 and NGC 4649 is indicated; (**c**) the same as in the Top Right Panel but for the $\Delta[\mathrm{Mg/Fe}]$ *versus* $\mathrm{M_V}$ relation. The *thick dashed line* is the linear regression of the results. (Reproduced with permission from [42]. Copyright 1998 Astronomy and Astrophysics).

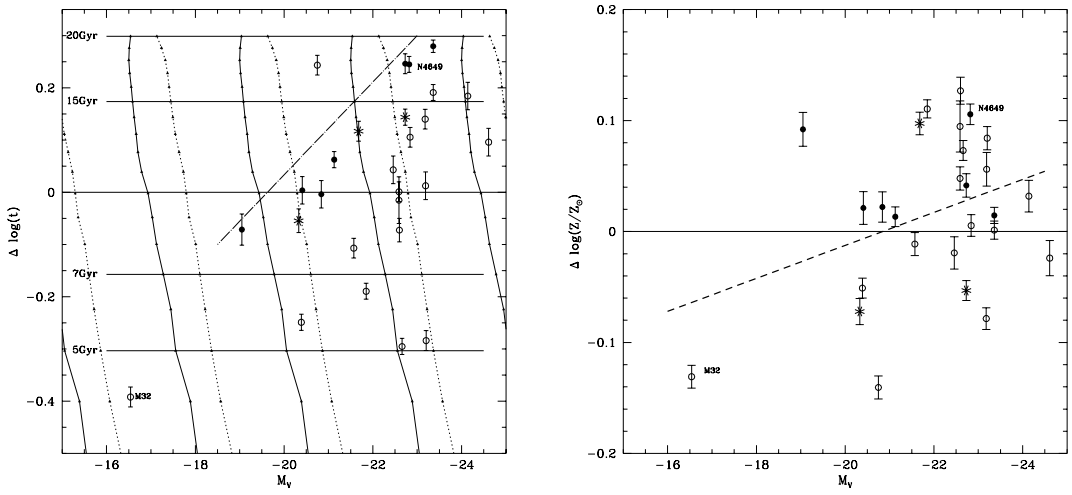

(**a**) (**b**)

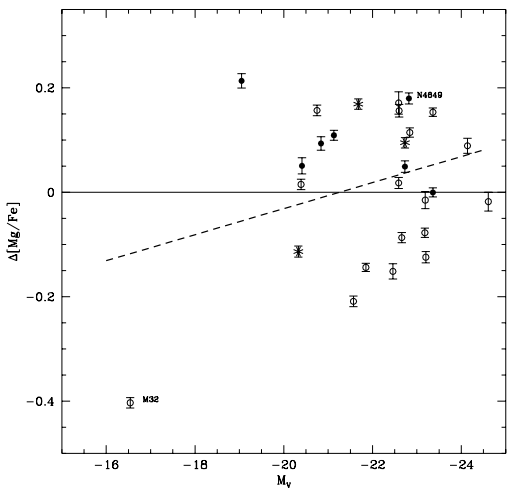

(**c**)

Figure 3. (**a**) The H_β *versus* [MgFe] plane for the galaxies (full dots) of [12] and the models (solid lines) of ETGs of [40]. Each model is labelled by its baryonic mass M_B in units of $10^{12}\,M_\odot$. The dotted lines are isochrones of different age (in Gyr) as indicated. The line called CMR-strip with the mean and maximum metallicities of the galactic models annotated along it is the analog of the CMR. The solid triangles show the evolutionary path of the $3 \times 10^{12}\,M_\odot$ model galaxy of [2] calculated with the closed-box formalism. The full dots and their mean error bars are the Re/8 data of [12]. Finally, the vectors $\Delta \log H_\beta$ and $\Delta \log[MgFe]$ display the mean shift in the data going from the R/8 data to the Re/2 data. To our knowledge this is the only case in literature where instead of SSPs, galaxy models are used; (**b**) the same as in the left panel but for the galaxies (asterisks) by [12] and the sample of shell (full circles) and pair (full squares) galaxies by [74], and SSPs from [42] of different metallicity. The dotted dashed lines are isochrones of different age. Normal and dynamically interacting galaxies have the same distribution. (**a**) is reproduced with permission from [40], Copyright 1996 Astronomy and Astrophysics. (**b**) is reproduced with permission from [74], Copyright 2000 Astronomy and Astrophysics.

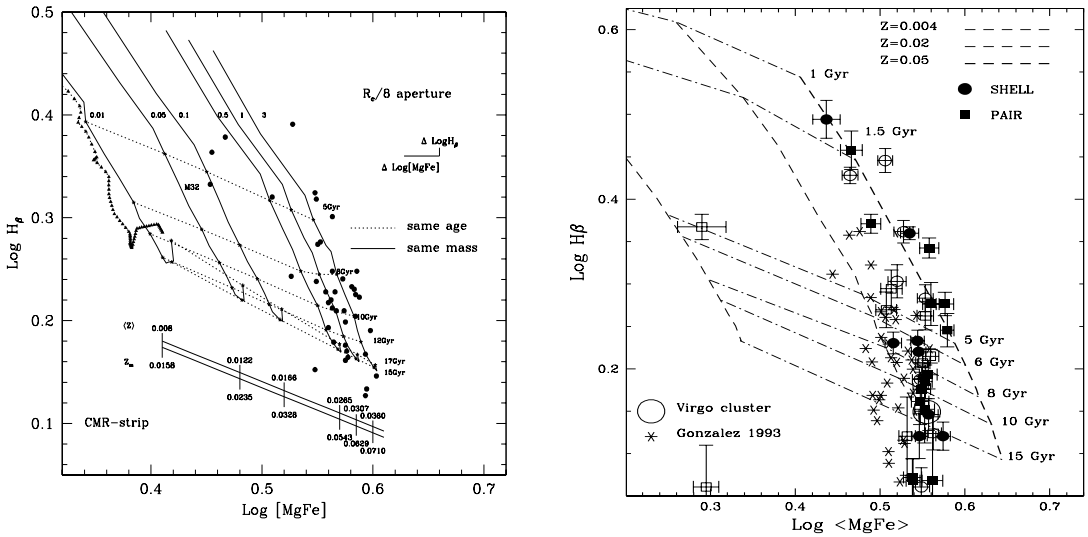

(**a**) (**b**)

Field galaxies. Looking at the field ETGs of [12] and other more recent samples, (i) there is a large scatter in H_β, perhaps as a result of the stronger sensitivity of this index to SF with respect to other indicators. Similar scatter occurs also with other indices of the same type, e.g., H_γ; (ii) The mean metallicities of ETGs probably span the range $Z_\odot \leq Z \leq 3Z_\odot$ as indicated by comparing theoretical models with data (see e.g., [4,13,14,40]); (iii) The field ETGs do not follow the relation expected in this diagram for objects matching the CMR [40] that is nicely followed by cluster ETGs, even though a significant scatter is seen [44,45,47,49,50].

Cluster galaxies. Long ago [44,45] measured the H_β and [MgFe] indices for a number of Elliptical (EGs) and S0 galaxies in the Fornax cluster. In this sample, EGs crowd toward low values of H_β and high values of [MgFe] and seem compatible with old ages, whereas S0s scatter on a much broader region perhaps indicating recent stellar activity. In addition to this, the cluster EGs of [44,45] are much less

dispersed along the H_β axis than the field EGs of [12]. Finally, compiling literature data, [77] derive the H_β *vs.* [MgFe] plane for EGs in loose and compact groups. Despite the small number of objects in total, ETGs in loose groups behave similarly to field ETGs, whereas ETGs in compact groups mimic cluster ETGs. In clusters and compact groups SFH is more concentrated, in field and loose groups SFH more diluted. Over the years many other samples became available, in general confirming the above scenario. Does all this imply that a galaxy's environment play an important role in determining its evolution? Perhaps favoring secondary activity of star formation like the one suggested by [40,42]?

Figure 4. (**a**) H_β *versus* [MgFe] plane in presence of the enhancement in α-elements and comparison between theory and observational data for galaxies in the local universe. Each hatched area is comprised between two SSPs of different metallicity ($Z = 0.008$ left-side and $Z = 0.070$ right-side). Along each SSP the age increases from 2 (top) to 13 Gyr (bottom). Each area is for a different value of the total enhancement factor Γ_α (the definition at varying metallicity is adopted). The data are the normal galaxies (open-triangles) of [60] corrected for emission (mean error bars are indicated). The dashed line is meant to provide a lower limit to H_β below which observational uncertainties may be so strong to render the comparison with theory meaningless (see the text for more details); (**b**) Γ_α *versus* T (in Gyr) plane. The data correspond to the sub-sample of the Trager catalogue selected to have $-0.30[\mathrm{MgFe}]+2.25 \leq H_\beta \leq 2.5$. Open circles are for $-0.30[\mathrm{MgFe}]+2.25 \leq H_\beta \leq 1.6$ and filled triangles for $1.6 < H_\beta \leq 2.5$. Long-dashed lines show the linear best fit for the whole sample. Mean error in age and Γ_α is shown. The top panel gives the age distribution for both sub-samples as indicated, whereas the right panel gives the Γ_α distribution. Reproduced with permission from [68]. Copyright 2007 International Astronomical Union.

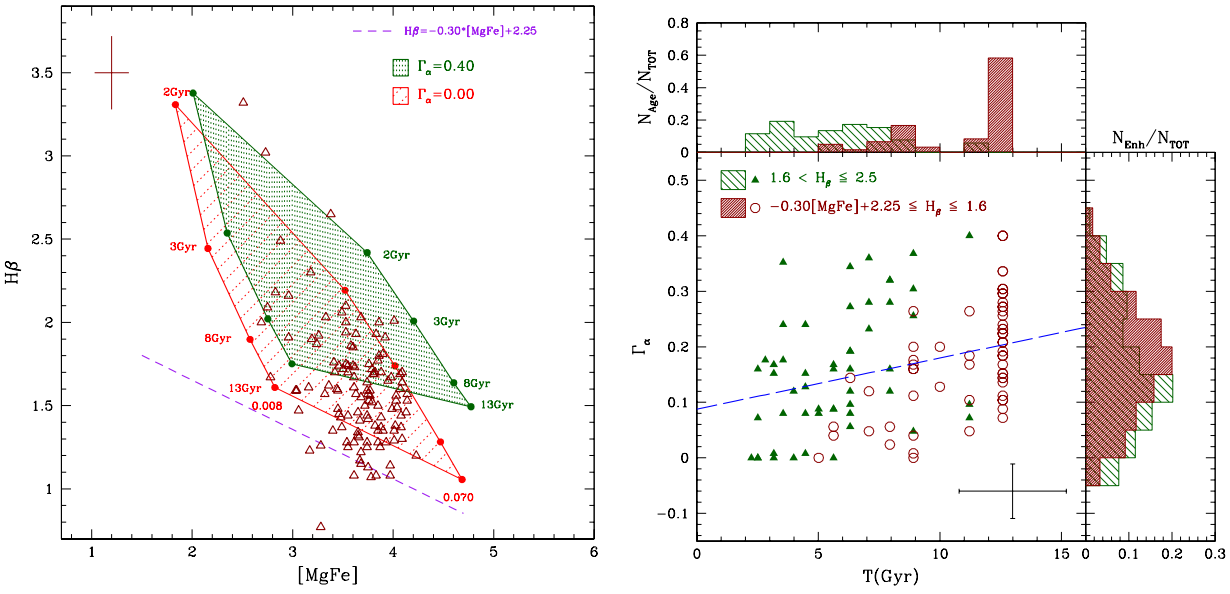

(**a**) (**b**)

Truly young or several episodes of SF? While the simplest explanation would be that some galaxies are truly young objects, the reality could be more complex in the sense that all galaxies in that sample are old but underwent different histories of SF. Some of them completed their stellar activity in the

distant past with no evidence of subsequent episodes. Others had a more prolonged SF history, perhaps in recurrent episodes of short duration and low intensity [13,14,40]. Reference [40] argued that the total duration of the star-forming activity should become longer at decreasing σ (mass). Therefore, physical conditions in low-luminosity (mass) ETGs seem to favor the occurrence of secondary stellar activity. This seems to be less probable in the bright massive ones. See also [48,78] for similar conclusions. Secondary stellar activity is also more probable in field and loose groups of ETGs than in those belonging to compact groups and clusters. References [44,45,47,49,50] measured the H_β and [MgFe] indices for a number of E and S0 galaxies in the Fornax cluster. In this sample, ETGs crowd toward low values of H_β and high values of [MgFe] and seem to be compatible with old ages, whereas S0s scatter over a much broader region, perhaps indicating recent SF activity. Furthermore, the cluster ETGs of [45] are much less dispersed in H_β than the field ETGs of [12]. Does all this imply that the environment of a galaxy may play an important role in determining its evolution?

2.5.4. Role of Enhancement of α-Elements on Age and Metallicity Determination: Another Intrinsic Degeneracy?

The large scatter in H_β shown by galaxies in the right and left of Figures 3 and 4 is commonly attributed to a large scatter in the age caused by secondary episodes of star formation. The scatter in [MgFe] is commonly attributed to metallicity. If there would be no effect of Γ_α (or Γ_Z) on H_β the scatter in age is an obvious conclusion. However, the dependence of H_β on Γ_α (or Γ_Z) makes this conclusion questionable at least for galaxies whose H_β falls in the range 1 to 1.6–1.8, *i.e.*, for the vast majority of them. Leaving aside galaxies with very strong H_β in the range 1.8 to 2.0, for which the age scatter seems to be unavoidable (looking at H_β *versus* age diagram these high values are possible only for stars younger than about 3 to 5 Gyr), let us concentrate on the region where most galaxies crowd, *i.e.*, for H_β in the range 1 to 1.6–1.8. In this interval, models predict that H_β increases when Γ_α goes from 0 to 0.4 by a factor $\Delta H_\beta = 0.2$ to about 0.4 as the metallicity increases from $Z = 0.008$ to 0.07. This variation is comparable to if not larger than that obtained by varying the age at given Z and Γ_α. Therefore, the effect of Γ_α (or Γ_Z) on H_β in particular, is far from being negligible, and we may predict that among old objects of the same age there could be a natural scatter in the diagnostic planes caused by galaxy to galaxy variations in the mean degree of enhancement due to the particular star formation history [65]. To cast light on this issue and the role played by the three parameters on the observational scatter in the H_β *versus* [MgFe] plane, the following analysis is made. We start selecting from the sample of galaxies shown in the left panel of Figure 4, a sub-set suited to our purposes: first we drop all galaxies with very large H_β (larger than 2.5) as they are very likely affected by ongoing or recent star formation; secondly, we drop all galaxies whose H_β is below the dashed line shown in left panel of Figure 4. The remaining galaxies should represent a fair sub-sample in which the effects of the three parameters are evenly balanced. We need now to specify what we mean by normal- and strong-H_β. As the range spanned by H_β for variations in Z, Γ_α (or Γ_Z) and age (we assume 1/3 of the Hubble time, *i.e.*, 4 Gyr) is of the order of 0.3 Å, we add this quantity to the mean value for a solar scaled old galaxy ($\sim$1.4 Å) and take $H_\beta = 1.6$ as the transition from typical to high values. Using the ages, metallicities and Γ_α found with the minimum-distance method for this sub-sample of galaxies,

in the right panel of Figure 4 we correlate the age with Γ_α using different symbols for galaxies with low- and high-H_β. Galaxies with $H_\beta \leq 1.6$ (empty circles) are preferentially (∼66%) old (13 Gyr) and spanning a large range of Γ_α; in this group, however, there are also a few younger objects with $\Gamma_\alpha \leq 0.2$. Galaxies with $H_\beta > 1.6$ tend to be younger (71% between 2 and 7 Gyr) (more recent episodes of star formation), less enhanced in α-elements (∼67% with $\Gamma_\alpha \leq 0.2$), and to span a narrower range of Γ_α than in the previous group. However also in this case there are objects of both old age and high Γ_α. The age and Γ_α distributions for the two groups are shown in the top and right panels in the right part of Figure 4. Finally, taking the linear best fit of the data regardless of H_β (long-dashed line) the general trend emerges: at increasing age the degree of enhancement increases as shown by the long dashed line in the central panel right part of Figure 4. Using the theoretical estimates of the three parameters we look for general correlations and find that at increasing age of the last episode of star formation the mean enhancement increases in agreement with current understanding of SNa explosions on galactic chemical enrichment. This scenario is somehow supported by the results for dynamical NB-TSPH simulations by [23] and the companion study of their chemical properties, the degree of enhancement in particular, by [24].

2.6. Indices and Broad-Band Colors as Tracers of the SF Activity

To what extent indices and broad-band colors in different photometric system would reflect the past SFH of the host galaxy as we see it today? Answering this question could somehow constrain current models of galaxy formation in the monolithic or hierarchical scheme. To this end, here we present ad hoc photometric Montecarlo simulations of SF owing to either mergers or internal causes [57,74]. The complex star formation history of an early–type galaxy is reduced to a burst of relatively recent star formation superposed to the bulk population made of old stars. The latter are in turn represented by a SSP whose age is randomly selected between the ages T_1 and T_2. The young stellar component, formed during the recent burst of star formation, is represented by a SSP whose age T_b is randomly selected between T_2 and a lower limit T_3. Typical values for the age limits are: T_1=13, T_2=10, and T_3=0.1 Gyr. The time-scale of the two star forming event are always assumed to be short compared to all other relevant timescales (ages, and Hubble time). The intensity of star formation is expressed by the parameter β giving the percentage of the galaxy baryonic mass engaged in the star forming episode. The past SFH of the simulated galaxy is schematically shown in panel (a) of Figure 5.

Since we are interested in guessing the minimum threshold above which the secondary episode gets importance in affecting the line strength indices, we will consider only the case in which the secondary episode involves a minor fraction of the galaxy mass. Typical values for the strength of the primary and secondary episodes of star formation are β_1=0.98 and β_2=0.02.

The metallicity Z_1 of the old stellar component is randomly selected between 0.008 (50% of the solar value) and 0.07 (3.25 the solar value). We have also built simulations in which the metallicity of the old component is forced to linearly increase from 0.008 and 0.07 over the age range T_1 to T_2. The metallicity Z_2 of the young component is randomly chosen over the whole range (*i.e.*, from Z=0.008 to Z=0.07), thus simulating the widest range of possibilities, going from acquisition of external less processed gas to chemical enrichment during the burst.

Figure 5. (**a**) Artistic view of the SFH in the model galaxies: an old dominant episode of intensity $I_B = \beta_1$ whose age is comprised between $T_1 = 13$ and $T_2 = 10$ Gyr ago, followed by another episode of intensity $I_B = \beta_2$ occurring at any arbitrary age comprised between $T_2 = 10$ and $T_3 = 0.1$ Gyr ago; the intensities of the two SF episodes can randomly vary; (**b**) Observational data and MonteCarlo simulations in the H_β *vs.* [MgFe] plane. *Left Insert*: The normal galaxies of [60] indicated by the open triangles and the shell- and pair-galaxies of [74] indicated by the filled squares. Note the smooth and nearly vertical distribution of both groups of galaxy. *Central Insert*: MonteCarlo simulations for the set of parameters T_1=13 Gyr, T_2=2 Gyr, β_1=1, no additional bursts of star formation. The metallicity is randomly chosen in the interval $0.008 \leq Z \leq 0.07$, no enhancement of α-element is considered (Γ_α=0). The solid lines are two SSPs with Z=0.008 (left) and Z=0.07 (right). Four values of the age, *i.e.*, 2, 3, 8 and 13 Gyr are marked. The thin dotted lines are the loci of constant age. The very large age range is required to get full coverage of the range in H_β spanned by the data. *Right Insert*: MonteCarlo simulations according to the recipe: T_1=13 Gyr, T_2=5 Gyr, random burst of star formation activity at a time in the interval $0.1 \leq T_1 \leq 5$, the same interval for the minimum and maximum metallicity and the same Γ_α as in the previous simulations. The percentage of the young population is β_2=0.02. The bulk population formed in the time interval T_3 to T_2 obeys the universal law of metal enrichment. All other symbols have the same meaning as in the Central Insert. (**c**) The same as in panel (**b**) but with the enhancement of *alpha*-elements as indicated. Reproduced with permission from [57]. Copyright 2004 John Wiley & Sons.

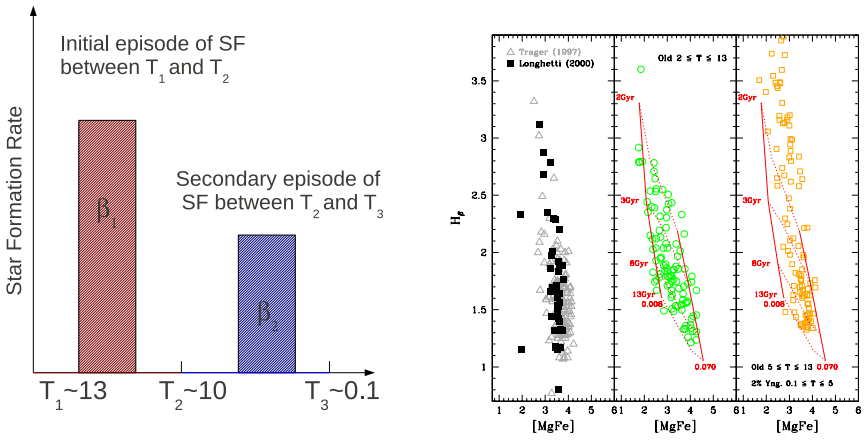

(**a**) (**b**)

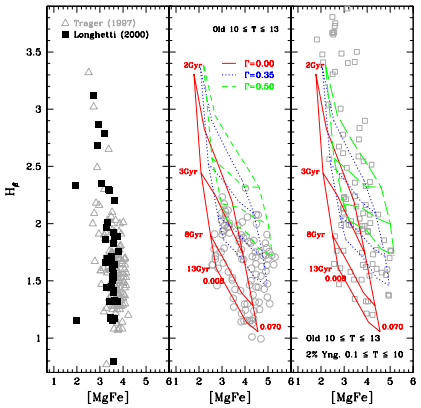

(**c**)

The simulations are first performed for SSPs with solar partition of elements, *i.e.*, Γ_α=0 (or Γ_Z=0) and then for Γ_α >0 (another dimension is added to the problem).

Finally, random errors are applied to the model line absorption indices indices to better simulate the observations (see [57] for all details). The error affecting an index is randomly evaluated according to $\Delta I = -\left\langle \frac{\Delta I}{I} \right\rangle_O I + 2 \times \epsilon \left\langle \frac{\Delta I}{I} \right\rangle_O I$ where ϵ is a random number between 0 and 1, and the subscript O stands for "observational".

The data to interpret are the line absorption indices of the normal ETGs in the [12,60] and the sample of the shell- and pair-galaxies of [74] which likely show evidences of past interaction and perhaps dynamical rejuvenation. The observational H_β vs [MgFe] plane for the [12,74] are shown in the panels (a) and (b) where we note the nearly identical distributions, and those of [60,74] in the panels (b) and (c) of Figure 5.

Large scatter in age and metallicity of the bulk population. This is the simplest interpretation of the distribution of the galaxies in the H_β *vs.* $[\mathrm{MgFe}]$ plane. Neglecting important effects due to enhancement in α-elements and recent stellar activity, matching the observational range of the data would require the bulk population of early type galaxies being formed in different epochs from galaxy to galaxy over a time-scale comparable to the Hubble time. In the central insert of panel (b) of Figure 5 we show a simulated sample of 100 objects for which the following parameters are assumed: T_1=13 Gyr, T_2=2 Gyr, β_1=1, no increase of the metallicity in this time interval, no later bursts of stellar activity, and finally Γ_α=0. The models galaxies distribute along the SSP lines of different metallicity according to their age. The simulation significantly differs from the observational data shown in left part of the same panel of Figure 5. Even if this view could be fitted into the classical hierarchical scheme of galaxy formation, it can be hardly sustained because it would predict spectro-photometric properties not fully compatible with the observational data for ETGs.

Random bursts of star formation. Bursts of star formation (from one to several) superposed to an old dominant population of stars seem to be more plausible and yield better results. Galaxies are conceived as old, nearly coeval systems, their population being approximated by a single SSP with age between T_1=13 and T_2=10 Gyr; this age range agrees with the current age estimate of ETGs in rich clusters [79]. A burst of stellar activity is added at an age T_b randomly chosen in the interval $T_2 - T_3$. Finally all the simulations are for Γ_α=0. The maximum intensity of the superposed burst amounts to 2% of the total mass, *i.e.*, β_1=0.98 and β_2=0.02. The simulations are presented in order of increasing complexity. We limit ourselves here to discuss the results and to highlight the point of disagreement with the observational data. For more detail see [57,74].

(i) Stronger bursts of star formation (*i.e.*, engaging more than 2% of the mass) are nor suited as they would predict too high values of H_β and too many *young* objects.

(ii) The expected distribution of objects with respect to the H_β index is at variance with the observational one. Indeed models of this type predict a bimodal distribution, whereby the old galaxies (those for which the burst is almost as old as the bulk of their stellar populations) clump together in the lower portion of the diagram, whereas the "young" objects (those with very young bursts) form a tail extending to high values of H_β.

(iii) Nevertheless, the burst alone cannot explain the smooth distribution observed at low H_β values. This is because the H_β index of a stellar population for which the 2% of the mass is in "young" stars and

the remaining 98% in old stars, may jump to the observed high values, but, fading very rapidly as the young stars disappear, cannot easily match the intermediate values. Slowing down the index decrease (corresponding to aging the "young" component) by increasing the percentage of mass involved by the young burst produces an uncomfortably large fraction of objects in the upper part of the diagram. A complex interplay between burst intensity and mean age of the stellar population should then take place, with the old bursts being on average stronger than the recent ones. It must be said, however, that when the burst itself is larger than a few percent of the total mass, the definition of the average age of the bulk of the stellar population becomes a problem.

(iv) The difficulty is partially cured assuming that the *old* population has an average age spreading over a significant fraction of the Hubble time ($T_2 \simeq 5$ Gyr). This is meant to indicate that either the object has been growing for such a long time with a low star formation rate, or that its major star formation activity was not confined to an early epoch. The young component is left to occur. It appears immediately that the observed smooth distribution in the H_β index together with the young tail is much better reproduced by such a kind of models (see [57,74] for details).

(v) Another problem arises if the metallicity is randomly selected. The distribution of the models galaxies in the left insert of panel (b) of Figure 5 strictly follows the path of a SSP, whereas the data run much steeper. We take this point to invoke the existence of a relation between the age of the bulk stellar population and its average metallicity. The simulations better fit the data.

The right insert of panel (b) of Figure 5 shows our final experiment incorporating all the hints we have been discussing so far. The simulations are based on the following parameters and assumptions: T_1=13 Gyr, T_2=5 Gyr, T_3=0.1 Gyr, β_1=0.98, β_2=0.02, average metallicity of the bulk of the stellar population forced to linearly increase from Z=0.008 to Z=0.070 over the time interval T_1 to T_2. Thanks to the combined effect of the large age and metallicity spread for the bulk population, the distribution in H_β *vs.* [MgFe] plane is nearly vertical. The larger range of metallicity is necessary to maintain a significant dispersion in [MgFe], because age differences tend to compensate metallicity differences. If the latter interpretation is correct, it suggests that young early-type galaxies in the field are on average more metal-rich than old systems, with an average metallicity gradient of about $\Delta\log(Z)/\Delta\log(t) \simeq -0.7$, the latter value being very dependent on the younger limit of the bulk age.

The main conclusion out of these simulations is that in addition to the mass dominating old population, which however has to be built up over a large time interval and under a suitable age-metallicity relationship, sprinkles of stellar activity in the recent or very recent past ought to considered in nearly all galaxies to reconcile theory and observations. *However, that all galaxies have undergone recent star forming activity is perhaps too demanding and other alternatives should be explored.*

The α-enhancement alternative. The results obtained by [57,65,66,68] for SSPs of the same age and metallicity but different degrees of enhancement in α-elements offer a third plausible explanation. To bottom line of the model is best explained by recalling the comparison between data and theory in the H_β *vs.* [MgFe] plane in presence of enhancement in α-elements already shown in panel (a) of Figure 4. Several points are soon evident:

(i) The majority of galaxies (those with $H_\beta \leq 2$) are fully compatible with being very old objects of the same age (say about 13 Gyr) but a different degree of enhancement in α-elements going from Γ_α=0 to Γ_α=0.5 (taking the so-called natural width caused by a possible variation in single elemental species

into account). As a matter of fact, an old galaxy (say a 10-13 Gyr object) being shifted to higher H_β by high Γ_α and/or [X_{el}/Fe] ([Ti/Fe] as a prototype) could lie in the same region occupied by a galaxy of significantly younger age and solar abundance ratios. At least part of the scatter along the H_β axis could be due to a different degree of enhancement in α-elements.

(ii) Only for galaxies with H_β>2, unless their enhancement factor Γ_α and abundance ratios [X_{el}/Fe] (like [Ti/Fe]) are larger than the above limits, the presence of secondary star forming activity ought to be invoked.

(iii) Looking at the position of models of constant metallicity and age but different Γ_α and/or [X_{el}/Fe] (for instance [Ti/Fe]), they scatter along a nearly vertical line. This implies that the metallicity relationship invoked for the bulk old population is no longer required. The *vertical* distribution of the data is simply caused by the compensatory effect of different combinations of Z, Γ_α and [X_{el}/Fe] ([Ti/Fe] in our case).

(iv) Secondary episodes of star formation are no longer a common feature to all galaxies, but an exceptional event limited to a small number of them. This agrees with the age distribution obtained by [65].

The α-Model is confirmed by the MonteCarlo simulations shown in the panel (c) of Figure 5. In the left insert we show the case of old galaxies with no secondary activity: the bulk population spans the age range given by T_1=13 Gyr and T_2=10 Gyr with β_1=1 and β_2=0, whereas the metallicity and α-enhancement span the whole range for the parameters Z, Γ_α, and [X_{el}/Fe] ([Ti/Fe] taken as a measure of the natural width). The models well match the bulk of data, *i.e.*, galaxies with $H_\beta \leq 2$, and yield a distribution in the H_β *vs.* [MgFe] plane which is nearly vertical (no memory of the SSPs path). In the right insert, we show the same but allowing for recent burst to occur at the age T_b randomly chosen in the interval T_2 to T_3. The burst intensity is for β_2=0.02. But for the few galaxies clearly caught in the burst mode (those with H_β>2), the two theoretical distributions are nearly identical and both fairly well reproduce the observational data.

These simulations open the gate to an interesting alternative explanation, *i.e.*, that the large scatter in H_β and [MgFe] is predominately caused by a spread in the chemical parameters metallicity Z and enhancement factor Γ_α rather than metallicity and age in the bulk population of a galaxy. Secondary activity of star formation is unavoidable only for a minority of objects.

The scatter in Z, Γ_α and also individual $[X_{el}/Fe]$ of the dominant old stellar component could be attributed to different kinds of star formation at the very early epochs, perhaps related to the physical conditions in the proto-galaxy affecting not only the intensity and duration of the star formation process, but also the stars' IMF and the abundance ratios in turn.

Interacting *vs.* Normal galaxies. Two important questions have been addressed by [74,80–82]: (i) Do interacting and normal galaxies differ in some properties of their spectral indices? (ii) Is there any combination of spectral indices able to date the interaction and the companion stellar activity? To this aim, they selected a sample of ETGs located in low density environments with clear signatures of interaction or fine structures (shell- and pair-galaxies). The results of those studies can be summarized as follows: (i) Normal and pair-galaxies follow the universal σ *vs.* Mg_2 relation, whereas shell-galaxies lie above it. The Fe *vs.* Mg_2 relation of normal, pair- and shell-galaxies is flatter than the theoretical prediction. Once more this fact hints for enhancement of α-elements; (ii) In the σ *vs.* H_β plane normal

galaxies seem to follow a nice relation, along which galaxies with shallower gravitational potential have stronger H_β whereas shell- and pair-galaxies scatter all over the plane. A group of galaxies with deep gravitational potential and strong H_β is also found. Is this a signature of recent star formation? (iii) Surprisingly, in the H_β *vs.* [MgFe] plane shell, pair and normal galaxies share the same distribution. There is, however, a group of peculiar galaxies with much stronger H_β as compared to the normal ones. Does it mean that the scatter seen in this diagram has a common origin, perhaps secondary episodes of star formation that can occur independently of whether or not a galaxy is interacting? (iv) The distribution of all galaxies in the H_β *vs.* [MgFe] is confined within a narrow strip (narrow range of metallicity) but it runs much steeper than the path followed by aging SSP. The latter trend was only marginally evident with the less numerous [12] sample. The explanation of the nearly vertical distribution of galaxies compared to that of SSPs was found in terms of secondary episodes of star formation of different mean age, and intensity compared to the initial (and dominant) one accompanied by chemical enrichment. The numerical simulations make soon clear that (a) the intensity of the secondary activity cannot exceed a few % (say 2%) as otherwise too many galaxies with strong H_β would be expected; (b) the age interval between the dominant and secondary episode must be much larger than about 2 Gyr otherwise we would notice a clump of low H_β galaxies followed by a tail of high H_β objects distributed along the locus of an aging SSP of suited composition; (c) only assuming a much longer age interval (say a significant fraction of the Hubble time) and important chemical enrichment for the bulk population $\mathrm{d}\log(\mathrm{Z})/\mathrm{d}\log(\mathrm{t}) = 0.7$ the observed distribution can be recovered. Therefore, the smooth and steep distribution suggests large age ranges for the bulk stars and substantial chemical enrichment (up to about two times solar).

Bursts of SF and dispersion of the Broad-Band Colors. With aid of above simulator of the SFH in galaxies, we derive the color evolution of a composite galaxy made by two episodes of star formation and compared it with the observational data. We limit ourselves here to show results for the classical (B-V) color. These are displayed in Figure 6 as a function of the age T_b and intensity β_2 of the secondary activity. The insert correlates the time T_R required by the post burst galaxy to recover its original red color as a function of the burst intensity expressed by $\beta_2 \times 100$. It turns out that for many combinations of T_b and β_2, the resulting (B-V) color would be too blue compared with the typical colors of ETGs, (B-V) = 0.95 $\pm$ 0.025. Stellar activities engaging 5% to 10% of the total mass and taking place as early as 5 to 6 Gyr ago would be detectable. The situation becomes even worse for higher β_2 and/or lower T_b. This implies that only remote or minor star-forming events are allowed.

2.6.1. Dwarf ETGs in Galaxy Groups and Clusters: The Case of Abell 851 and Coma

The situation with dwarf ETGs seems to be the same independent of the age (redshift) of the galaxy population. Indeed, the existence of blue, low-luminosity ETGs in Coma and Abell 851 (CL 0939 + 4713) detected by [83] in the far UV (F300W and F218W HST-WFPC2 observations), supports the possibility that secondary activity of SF in these galaxies occurred randomly throughout their lifetime. In contrast the bright ETGs once again seem to be very old objects undergoing passive evolution since the initial star-forming activity. Abell 851 is a rich galaxy cluster at redshift $z = 0.41$, in which the morphological classification for the majority of its galaxies is feasible. Possible evolutionary

effects in the UV from $z = 0.4$ to the present time can be investigated by comparing the rest-frame (mid-UV/optical) colors of galaxies in Abell 851 with balloon-borne data of other rich clusters such as the Coma Cluster, as well as by resorting to suitable galaxy evolution models. The combined CMD for the Abell-851 and Coma galaxies is presented in Figure 7. Mounting of the two sets of data has been made applying the relative distance modulus $\Delta(m - M) = 6.47$. The remarkable coincidence between the two sets of data means that no significant evolution between the two epochs (from $z = 0.4$ to the present) is detectable. Reference [83] assumed a Friedmann Universe with cosmological parameters $H_0 = 50$ km/s/Mpc, $q_0 = 0$ and red-shift of galaxy formation $z_{for} = 5$. Therefore, the red-shift of Abell 851 translates into the rest-frame age of 10.8 Gyr. The big filled circles show the expected CMR of passively evolving galaxies (whose mass is indicated) as it would appear at the age of 10.8 Gyr (red-shift $z = 0.41$). While bright galaxies are fully compatible with the expectation for purely passive models (mass of about $1 \times 10^{12}\, M_{\odot}$), this is not the case of those galaxies falling in the magnitude range $22 < m_{702} < 24$ and blue color (near zero or negative). In order to be observed above the detection limit (the dashed line), a recent episode of star formation is required. Owing to sensitivity of the blue pass-bands F300W and m_{UV} to the UV flux, the star forming episode in the Abell galaxies must have occurred not too long before the age interval sampled by the data (10.8 Gyr). Galaxies whose secondary activity terminated only a few 10^8 yr earlier than the reference age would fall below detection. The models correspond to burst ages $T_b = 10.0$, 10.4, and 10.7 Gyr, constant duration of 0.01 Gyr, and relative intensities $I_b = \beta_2$ (percentage of mass turned into stars) of 1%, 5% and 10%. The argument applies also to faint ETG's in Coma with the only difference that the reference age is significantly older (say about 13 Gyr). Since there is no reason why Abell 851 and Coma faint ETG's should coordinate their efforts in triggering star formation, the unavoidable conclusion is that faint (low mass) galaxies are able to undergo recent (likely current) stellar activity and only those in which the process is underway or just over are detected in this CMD.

2.7. Scale Relations: Fundamental Plane

As it is known from long time, ETGs are similar in their structural and dynamical properties and obey empirical relationships among colors, luminosities, half-light radii, surface brightness profiles, and velocity dispersions that are ultimately related to their stellar content and dynamics. They are known as the *Scaling Laws*, among which particularly important are the *Fundamental Plane* (FP), the *Kormendy Relation* (KR), the Star Mass-Radius Relation (MRR), see [84,85] for extended reviews of the subject. In the following, we briefly touch upon the so-called "Tilt of the Fundamental Plane" and postpone the discussion of the MRR and KR to Sections 5 and 6, respectively.

Figure 6. Simulations of the scatter in the (B-V) colour of ETGs, induced by secondary episodes of SF, as a function of the burst age T_B and intensity I_B. The shaded bar is (B-V) $= 0.95 \pm 0.025$, typical mean value for ETGs. The burst intensity β_2 are in fractions of the total baryonic mass, *i.e.*, the relation $\beta_1 + \beta_2 = 1$ is applied. The percentage β_2 is multiplied by 100. The age is in Gyr. Reproduced with permission from [57]. Copyright 2004 John Wiley & Sons.

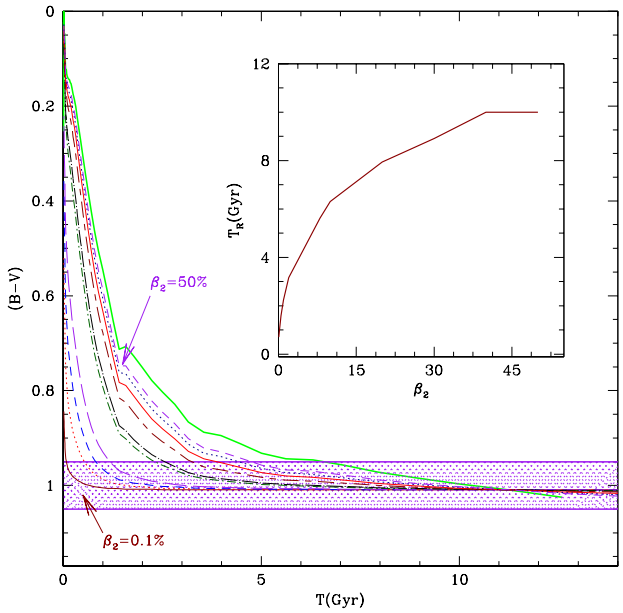

Tilt and Tightness of the Fundamental Plane. In the space of the central velocity dispersion σ, effective radius R_e, and surface brightness I_e, ETGs cluster around a plane called the Fundamental Plane. Using the coordinate system defined by [86], mere rotation in the space of σ, R_e, and I_e, the Virial Theorem, and the identities $L = c_1 I_e R_e^2$ and $M = c_2 \sigma^2 R_e$, the physical coordinates correspond to $\kappa_1 = \frac{1}{\sqrt{2}} \log[\frac{M}{c_2}]$, $\kappa_2 = \frac{1}{\sqrt{6}} \log[\frac{c_1}{c_2} (M/L) I_e^3]$, and $\kappa_3 = \frac{1}{\sqrt{3}} \log[\frac{c_1}{c_2}(M/L)]$ where c_1, and c_2 are the so-called virial coefficients. Of particular relevance is the projection of the FP onto the $\kappa_1 - \kappa_3$ plane, where the FP is seen edge on. In the case of the Virgo elliptical galaxies to avoid distance uncertainties, the relation $\kappa_3 = 0.15\kappa_1 + 0.36$ with dispersion $\sigma(k_3) = 0.05$ is found (see [87]). First the Fundamental Plane is tight, second it tilts because the ratio M/L_B increases with the galaxy mass. Reference [88] investigated two possible origins of the tilt: a systematic variation of the IMF (of power-law type) and a trend in the relative proportions and distributions of bright and dark matter. The conclusion is that in both cases, in order to explain the tilt and tightness of the FP at the same time, major changes and fine tuning are required. In brief, the IMF or relative bright/dark matter distribution should change along the FP, but at every position a small dispersion in the IMF or relative bright/dark matter distribution is required to preserve the tightness. In a subsequent paper along the same line, reference [87] looked at various effects of a structural and dynamical nature (such as orbital radial anisotropy, relative bright/dark matter distributions, shape of the light profiles) under the assumption of a constant stellar mass-to-light ratio. While anisotropy gives a marginal effect, variations in the bright/dark matter distributions and/or shape of the light profiles can produce the tilt. Also in this case fine tuning is, however, required to preserve the

tightness of the FP. The idea of an IMF varying with the physical conditions of the interstellar medium, and the galaxy type in turn, was explored systematically by [73], who reproduced the tilt of the FP. The problem was further investigated by [23] with the aid of NB-TSPH models of galaxy formation and evolution and a simplified description of their photometric properties, and the observational data of [89]. The results are shown in Figure 8. Tilt and tightness are reasonably accounted for.

Figure 7. Dwarf galaxies in Abell 851 and Coma Clusters. Models showing the expected location of both passively evolved and young population contaminated ETGs, superimposed to the UV/optical C-M diagram for ETGs of both Abell 851 and Coma Clusters. Both models and galaxy magnitudes have been scaled to $z = 0.41$. The meaning of symbols, both for data and models, is given by the key in the figure. On the right side are represented galaxy models at a fixed age of 10.8 Gyr with mass of 10^{10}, 10^{11}, and 10^{12} $M_{\odot}$ respectively, which consist of an aging, uncontaminated single-burst population. Dashed lines connect both the highest and lowest mass models to their expected location in case they have experienced recent "rectangular" bursts having constant duration (10^8 yr) and slightly different efficiencies β_2 (within 1% to 3%), centered at a time T_b of 0.1, 0.4, and 0.8 Gyr before the epoch recorded by the observations, respectively. Multiple symbols correspond to the above slightly different efficiencies of the recent burst. The dot-dashed line represents the FOCA detection limit for UV observations of Coma Cluster galaxies. Reproduced with permission from [83]. Copyright 2000 American Astronomical Society.

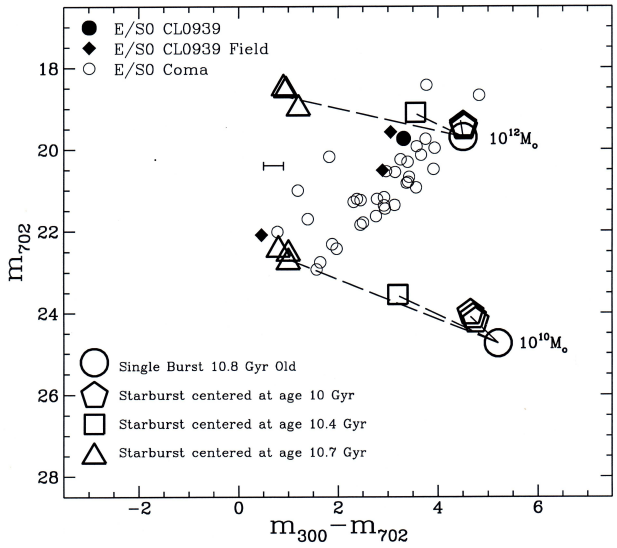

2.8. Galaxy Formation in Cosmological Context

Over the past two decades, major efforts have been made to acquire data of unprecedented richness, completeness and depth that enlightened the properties of ETGs from the local Universe to high redshift all the way to $z \simeq 2$ and beyond (see [84,85,90–93], for exhaustive and updated reviews of the subject). Thanks to this, the frontier for high-z objects has been continuously and quickly extended from $z \sim 4$–5 [94,95], and $z \sim 6$ [96,97] to $z \sim 10$ [98–100]. According to the current view, first

galaxies formed at $z \sim$ 10–20 [101] or even $z \sim$ 20–50 when DM haloes containing BM in cosmological proportions gave origin to the first sufficiently deep gravitational potential wells [102–104]. In addition to this, there is observational evidence for large and red galaxies already in place at very high redshift (see [105,106]). Furthermore this high redshift universe is obscured by copious amounts of dust (see [107–114]), whose origin and composition are a matter of debate [115–120] but surely are of stellar origin thus implying star formation activity at very early (high redshift) epochs.

Mass assembly and star formation. The analysis of this body of data has assessed the following: (i) Low- as well as high-redshift ($z \sim 1$) data indicate that cluster ETGs formed the bulk of their stars at redshifts $z \geq 3$, whereas ETGs in low-density environments did it at redshifts $z \geq 1.5 - 2$, *i.e.*, with a time delay of about 1–2 Gyr; (ii) The duration of the major star-formation phase is shorter in massive galaxies and longer in the less massive ones; the oldest stellar populations are indeed found in the most massive galaxies. Furthermore, existing data suggest that the most massive ETGs are fully assembled at $z \sim 1$; (iii) With increasing redshift the number density of ETGs, especially of the less massive ones, decreases. Beyond $z \simeq 1$ the space density of ETGs drops significantly, and ETGs are gradually replaced by a population of massive, star burst galaxies, thus suggesting that ETGs could be the descendants of these objects. In front of this observational scenario, current theoretical understanding is gasping for breath. It is indeed commonly accepted that according to the hierarchical scenario small galaxies should form prior to massive galaxies. However as already recalled, the redder colors, higher metallicities and enhanced [α/Fe] ratios are all indicative of older stellar populations with rather short star formation time scale (so called down-sizing). Stellar mass assembly favors massive ETGs at early times [121].

Luminosity and Mass distribution functions. Theory provides the mass function for DM haloes (see e.g., [122], observations yield the luminosity functions of galaxies [123]. Arguments based on the comparison of the cooling *vs.* the dynamical time fix the characteristic mass of galaxies at about $10^{12}\ M_{\odot}$ [124–126]. However the theoretical luminosity function predicts an excess of small galaxies and also an excess of massive galaxies in the nearby universe and a deficiency of high mass galaxies at high redshift (see [92]).

Star formation rate and galaxy mass. The rate of star formation measured in different samples of galaxies with a variety of methods is found to increases with the stellar mass of the galaxy along the so-called Main Sequence. There is however a rich population of outliers for stellar masses in the range $\sim 10^{10}\ M_{\odot}$ to about $6 \times 10^{11}\ M_{\odot}$ whose Start Formation Rate (SFR) may be as high as 10 times the Main Sequence value or even higher [127].

Efficiency of Star formation. In a star forming environment, like giant molecular clouds, the efficiency of star formation (SFE), defined as SFE = (SFR $\times \tau_D$)/M_g, with SFR being the star formation rate, τ_D the dynamical time scale and M_g the gas mass, is very small and nearly constant 0.2. Similar value is found for the whole Milky Way and also for all nearby and distant disk galaxies, the so-called Schmidt-Kennicutt relation [128,129] when the SFR is per unita area. In addition to this, star formation in galaxies is bimodal: Ellipticals are red and Disk galaxies are blue, with very few objects in between. This implies that either star formation is ongoing or it has quenched several Gyrs ago. In contrast, the Green Valley is populated by Seyfert galaxies with intermediate age stellar populations [130]. See [92] for a thorough discussion of the physical causes and implications.

Figure 8. (**a**) Fundamental Plane of ETGs in the B passband, *i.e.*, the relation $\log(M_s/L_B)_\odot$ *vs.* $\log M_{s,12}$, where $M_{s,12}$ is the star mass in units of $10^{12}\,M_\odot$. The small open circles and open triangles are the normal/giant and dwarf ETGs of ([89], BBFN), respectively. The thin dotted-dashed line labeled BBFN is the least square fit of the data limited to normal/giant galaxies, *i.e.*, $M > 10^{10}\,M_\odot$. The heavy dashed line shows the slope of the κ_3 *vs.* κ_1 relation for ETGs in the Virgo cluster. This line can be shifted both horizontally and vertically because its zero point has not yet been defined in the $\log(M_s/L_B)_\odot$ *vs.* $\log M_{s,12}$ plane. The filled squares are the models B of [23]. Those of $M_h = 10^9\,M_\odot$ with slightly different initial density are indicated by the labels LD (low density), ID (intermediate density) and HD (high density). The thick solid line labeled Mod-B is the least square fit of models B more massive than $M_h = 10^{10}\,M_\odot$. The agreement with the best fit of the data in the same mass range (the dotted-dashed line) is remarkable. There is a small offset in the zero point which can be attributed either to $\log(M_{s,12}/L_B)_\odot$, a factor of 1.2 larger than the mean data, or $\log M_{s,12}$, a factor of two smaller than the mean data. Also in this case, the slope agrees with that of the κ_3 *vs.* κ_1 relation. The filled triangles connected by the line labeled Mod-A are the models of type A (very high initial over-density) by [23]. Finally, the large open stars are *simple, largely analytical models* with metallicities $Z = 0.002$ and $Z = 0.02$. The dotted lines labeled by the metallicity are their linear fits (see [23], for any other detail); (**b**) Three projections of the κ-space. In all panels the small empty squares are the ETGs of [89] from dwarfs to giants, whereas the filled triangles and squares are the models of type A and B of [23], respectively. The bottom panel shows the effect of I_e which over the whole mass interval varies of a factor of about 300, whereas the mass-to-light ratio varies only by a factor of 3. The dashed lines are the best fits of the models as indicated. The solid line is the observational boundary $\kappa_1 + \kappa_2 > 8$ beyond which the zone of exclusion (ZOE) is found (see [23], for a more detailed discussion of this plane). See the text for the discussion of this panel. The mid panel is the FP seen edge on. The solid line is the best fit of the theoretical models for galaxies with $M_h \geq 10^{12} M_\odot$. Reproduced with permission from [23]. Copyright 2002 John Wiley & Sons.

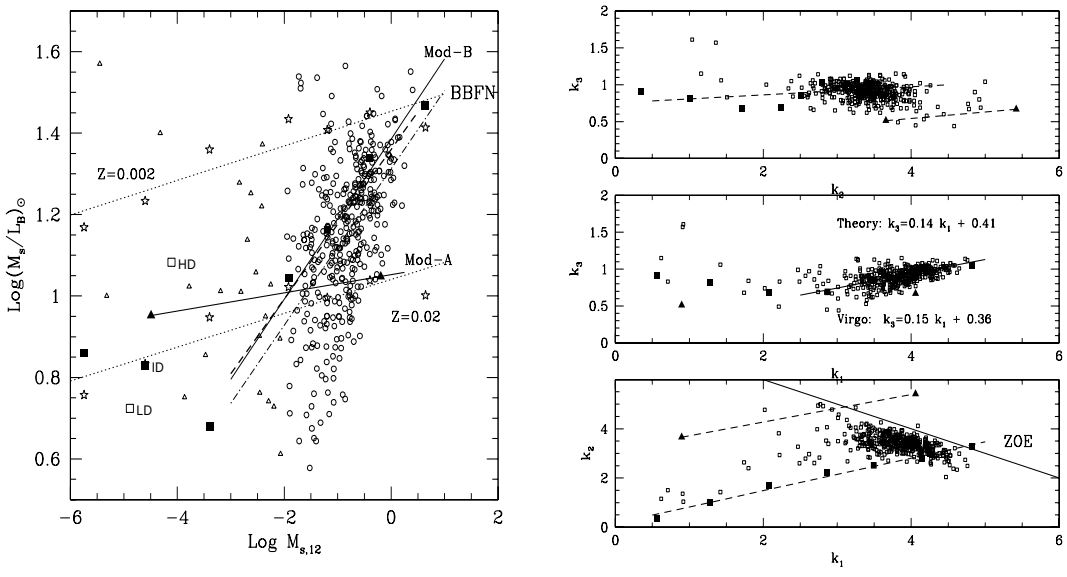

(**a**) (**b**)

The star formation time scale. The SFR per unit stellar mass, otherwise known as the specific star formation rate (SSFR) [131–133], yields the time scale of star formation ($\tau_{SF} = 1/SSFR$). The latter goes from about 10 Gyr to about 0.5 Gyr at $z = 2$ and remain constant afterwards, with a few exceptions. This can be understood as a result of different feed back regulating star formation: via only SNa explosions for $0 \leq z \leq 2$ and SNa explosions plus Active Galactic Nuclei (AGNs) for $z > 2$. Alternatively, it could be caused by much stronger inflow of gas at very early epochs triggering more intense star formation as in the monolithic-like models with no AGNs calculated by [1,23,134–137]. However, the important role of AGNs cannot be excluded. See [92] for a deeper discussion of this issue.

Luminosity-Mass-Radius relationship. A modern version of this important relation is by [138] where the radius is the half-light radius (nearly equal to the effective radius) and the mass and the luminosity refer to the stellar content enclosed by this. This relationship combines data for ETGs with those of Globular Clusters (GCs), ultra-compact dwarfs, normal dwarf galaxies and clusters of galaxies. Leaving galaxy clusters aside, there is a continuous transition from GCs to bright ETGs, which is also evident projecting the data on the mass-radius plane. The slope of this relation was explained by [23] as the subtle product of the loci of constant initial density for dissipation-less collapse and the locus drawn by the mass and radius of the maximum typical galaxy mass at different redshifts. It will be discussed in more detail in Section 5. Dwarf galaxies deviate from this relation because they suffer more of dissipative processes (e.g., galactic winds by SNe explosions) with respect to the nearly dissipation-less case of more massive galaxies.

2.9. Conclusions from the Observational Preamble

The present-day challenge with ETGs is to unravel their formation and evolution history. In a simplified picture of the issue, the problem can be cast as follows. Do ETGs form by hierarchical merging of pre-existing sub-structures (maybe dwarf or disc galaxies) made of stars and gas? Was each merging event accompanied by strong star formation? Or conversely, do they originate from the early aggregation of lumps of gas turned into stars in the remote past via a burst-like episode ever since followed by quasi quiescence so as to mimic a sort of monolithic process? In brief, the body of observational data acquired over the past two decades concerning the CMR, the chemical abundances and abundance ratios, their variation with the galaxy luminosity (mass), the line strength indices and associated diagnostic, the large scale variation of masses, radii, spectro-photometric properties as a function of the redshift, the recent discovery of downsizing of the mass assembly as a function of the redshift, and the time delay of the bulk stellar activity increasing with decreasing galaxy mass and decreasing mean density of the galaxy environments strongly suggest that:

(i) In massive ETGs, very intense activity in the remote past generated the bulk of stars perhaps followed by minor episode of star formation in recent times. In contrast in low mass ETGs the bulk of star formation occurred later in time perhaps in a number of secondary episode or even prolonged stellar activity. In the latter galaxies, the situation is the same independently of the age (red-shift) of the galaxy population. Indeed, the existence of blue, low-luminosity ETGs in clusters with different red-shift (see e.g., Coma and Abell 851), supports the fact that secondary activity of star formation in these galaxies

has randomly occurred all over their lifetime. Secondary stellar activity was also more probable in ETGs belonging to the field and loose groups than in those belonging to compact groups and clusters.

(ii) The dispersion in indices like H_β as well broad band colors suggest that subsequent episodes of star formation were of small entity otherwise much larger scatter would be present.

(iii) Interacting and non-interacting ETGs (in low density environment the former and in the field the latter) have the same distribution in some two-indices planes (e.g., H_β *vs.* $[\mathrm{MgFe}]$). This fact may suggest that dynamical interactions are not a necessary prerequisite for the occurrence of secondary activity, but internal causes are equally possible.

(iv) Major mergers and companion star formation in a relatively recent past are not likely, unless the intensity of the secondary activity is very small (*i.e.*, engaging less than a few percent of the total BM of a galaxy). Were mergers the only possible mechanism to form massive ETGs, this should have occurred in a remote past (half of the Hubble time at least). In any case, mergers with no star formation even in a recent past cannot be excluded. But is this likely?

To conclude, the emergent picture does not seem to fit the classical paradigm of galaxy formation, *i.e.*, hierarchical aggregation in which small objects form first and then merge together to form bigger and bigger objects all over the Hubble time. The observational data suggest a different scenario: early aggregation of haloes of DM and BM into objects with mass comparable to the typical galaxy size, accompanied by stellar activity followed by quiescence or quasi quiescence with the intensity and mode of stars formation suitably depending on the mass and likely other physical properties, the most important of which is the mean density of the medium out of which the galaxies are formed. We refer to this mechanism as the *early hierarchical, quasi monolithic view* of galaxy formation. Therefore, the first task here is to check whether the kind of proto-galaxies suited to our aims can be generated by the cosmological medium at high redshift, and second to understand the physical conditions driving the type and intensity of the star formation. In other words, we intend to examine whether a scenario in which all important actions of the mass aggregation and star formation of a galaxy may take place at early epochs and may yield model galaxies closely resembling the real ones.

3. Semi-Analythical and Numerical Galaxy Models

The advent of large galaxy surveys probing both the nearby (e.g., Sloan Digital Sky Survey (SDSS), Great Observatories Origins Deep Survey (GOODS), and many others) and the distant Universe (e.g., HST-deep field, Spitzer, Herschel, *etc.*) has led to unprecedented progress in the empirical understanding of galaxy formation and evolution. Nevertheless, it is difficult to link the galaxies we see at high redshift with the ones we see in the local Universe and even more difficult and challenging is to frame all this information in a coherent theoretical framework.

The current paradigm is the Λ-CDM model of the Universe, dominated by DE and DM (up to 95% of the total mass budget whose nature is still a mystery), in which under the action of gravity and via continuous mergers of small haloes of DM mass assembly of larger and larger entities of all scales are formed, the DM haloes, in which BM collapses to give rise to stars and stellar mass assembly (in a word to galaxies).

This view is confirmed by large scale cosmological simulations of typically ∼500 Mpc on a side in the framework of a given cosmological model of the Universe (nowadays the Λ-CDM) in which the appearance, growth and subsequent aggregation of perturbations of all scales are suitably described, e.g., the Millennium Simulation by [139,140]. Considering the huge number of DM haloes (proto-galaxies candidates) that come into existence, there is no room to include also BM and to follow the formation of real galaxies with the desired accuracy. Therefore, the large scale cosmological simulations usually leave BM aside. However, they are the back bone of existing models of galaxy formation with BM included because they provide the mass assembly history of haloes (MAH) and the initial conditions to the so-called monolithic-like galaxy models. Current models of galaxy formation and evolution can be grouped in semi-analytical (SAMs) and hydrodynamical (HDMs). The latter in turn split in two categories according to the numerical technique in use: the cell-based in the modern version with adaptive meshes to follow a large range of scales (see [141], and references) and the particle-based in the modern version of smoothed particle hydrodynamics (see [142], and references).

3.1. Semi-Analytical Models

Knowing the MAH of haloes, either retrieved from cosmological simulations or built up with Monte-Carlo probabilistic techniques [143], the BM is added to haloes and assuming suitable prescriptions for gas cooling and heating, star formation (often with chemical enrichment), energy feedback by SNa explosions and AGN (the central black hole), morphological transformation of disks into elliptical structures as a consequence of mergers, the population synthesis techniques to simulate luminosities, magnitudes and colors of the stellar content, *etc.* In other words, the structure and history of a galaxy are determined. Over the past two decades, SAMs have been world widely adopted to predict and possibly to explain the observational data. Modern SAMs are very sophisticated codes (e.g., [144]), however relatively easy to use, and often publicly-available together with their outputs. The advantage of SAMs is that the importance of various physical processes can be easily gaged by looking at the model response to turning a process on/off. The weakness of SAMs is that the physics is somewhat controlled by hand and largely parameterized. Recent, critical review of the successes and 'drawbacks of SAMs is by [92] to whom we refer. Suffice it to say that the SAMs theory was largely successful and in turn widely accepted [145–150] and that only recently some failures were brought into evidence. To mention a few we recall the rapid decrease in the cosmic SFR, the number of dwarf galaxies, the observed downsizing that simply opposes to the hierarchical view [151–153], the issue of gas accretion *versus* mergers in driving star formation, and the recent evidence of a systematic steepening of the initial mass function in massive ETGs (see [92,152], for all details and exhaustive referencing).

3.2. The NB-TSPH Models

As already mentioned the particle based models (combined with smoothed particle hydrodynamics) are customarily used for large scale simulations of the cosmological tissue of the Universe in presence of sole DM to determine the large scale mass assembly of the Universe (individual haloes, groups and clusters of DM haloes, filamentary structure). In literature there are many, very successful studies among which, to quote one for all, we recall ([139,140], and references therein). Combining the particle

technique (in the so-called N-Body Tree formalism used to treat the gravitational interaction [154]) with the Smooth Hydrodynamics technique to simulate a real fluid by a discrete number of particles [142,155], and implementing all physical processes that are needed to follow the complex game of formation and evolution of galaxies, one obtains the N-Body-Tree-Smoothed Particle Hydrodynamics (NB-TSPH) models. The latter have been used in much less numerous studies to model galaxies in the so-called monolithic-like scheme (see [1,23,134–137], and references therein). The merit of these models is the effort to describe the formation and evolution of individual galaxies made of DM and BM according to a given cosmological view of the Universe (e.g., S-CDM or Λ-CDM) from the time of their appearance as perturbation seeds at a certain redshift to the present. The models follow the growth of the initial seed by early aggregation of other seeds toward more and more distinct structures (maybe via the aggregation of many sub-lumps of matter), the collapse and cooling of baryons toward the stage of star formation, the conversion of gas into stars at a certain rate and specific efficiency, the chemical enrichment of the gas by self pollution via mass loss by stellar winds and SNa explosions, the decline of star formation both by gas heating due to energy feedback and gas consumption, the interplay between gas cooling and heating, the establishment of a duty cycle among the various competing physical agents, the presence of AGN phenomena (not always included because of the uncertainties and difficulties of this issue), and finally gas ejections in form of galactic. All this is taken into with the minimum number of adjustable parameters (ideally no one should be present). The goals of all those studies are the evolutionary history of a galaxy from its initial conditions to the present and the comparison of the structural and physical properties of the model galaxies with their observational counterparts.

4. The Monolithic View of Galaxy Formation and Evolution

In the so-called NB-TSPH formalism, each component of a galaxy (DM, gas and stars) is represented by a number of particles (bodies) with different properties. Furthermore, the galaxy formation process must be framed in a cosmological context for which some description is required. Galaxies continuously change their properties due to a large variety of physical processes. The three components interact each other by gravity, whereas gas undergoes some special effects caused by sources and sinks of energy, e.g., radiative cooling and inverse Compton effect, heating by stellar feedback (supernova explosions, and stellar winds), and the cosmic UV background. The gas may undergo star formation, and chemical enrichment due to nuclear processing in stellar interiors, and mixing with stellar ejecta (supernovae and stellar winds). Finally, extremely large ranges in physical values of the galaxy properties are possible. In brief, galaxy masses M_h go from 10^6 to $10^{14}\,M_\odot$ (8 orders of magnitude), gas temperature from 10 to 10^8 K (7 orders of magnitude), gas density from 10^{-33} to 10^{-18} g/cm^3 (25 orders of magnitude), length scales from 1 to 10^7 pc (7 orders of magnitude), and evolutionary time scales from 1 to 10^{10} years (10 orders of magnitude).

To suitably describe a galaxy with the NB-TSPH technique, very large numbers of particles are (would be) needed. For instance for baryonic mass of a galaxy of $10^{11}\,M_\odot$ (medium/high size object), the typical mass of the BM particle is about $10^4\,M_\odot$ whereas for a small size object with mass of $10^6\,M_\odot$, the mass of the BM particle goes from 10^4 to $10^2\,M_\odot$. Often the mass resolution is lower than those limits. Finally, galaxies may be the site of extremely violent phenomena, such as the supernova

explosions, supersonic turbulence and shocks, and AGN feedback that are still difficult to implement in NB-TSPH models.

The galaxy models we are going to describe have been calculated with the NB-TSPH code "EvoL" developed by [1,23,134–137,156–158] to whom the reader should refer for all details. Suffice to recall here that EvoL is a Lagrangian N-Body parallel code designed to study the evolution of astrophysical systems on any spatial scale, from large cosmological volumes to sub-galactic regions. In the following, we will focus the attention only on the initial conditions, the star formation efficiency, chemical enrichment, and the treatment of the interstellar medium (ISM) and leave aside all other physical and technical details of NB-TSPH simulations of model galaxies that can be found in [1,134–137].

4.1. Initial Conditions from the Cosmological Tissue

The ideal procedure to derive the initial structure of a proto-galaxy would be to start from large scale cosmological NB simulations of typically ∼500 Mpc on a side in the framework of a given cosmological model so that the appearance, growth and subsequent aggregation of perturbations of all scales can be suitably described, cfr. e.g., the Millennium Simulation by [139,140] who studied the formation, evolution and clustering of DM haloes in the ΛCDM cosmology. Of course these simulations require a huge number of particles: for instance, the Millennium run followed 2160^3 (more than 10 billions). Considering the huge number of DM haloes (proto-galaxies candidates) that come into existence, only a small number of particles will be used to describe the internal structure of many of them, the smaller ones in particular. If this way of proceeding is fully satisfactory from the point of view of a large scale cosmological simulation, it is not viable to study in detail single galaxies. These indeed will have total masses ranging from 10^8 to $10^{13}\,M_\odot$, dimensions from 1 to several tens of kpc, and M_{DM}/M_{BM} in cosmological ratio where DM is by far dominating. To be properly described a single galaxy require a large number of particles (at least 50,000) for each component. Repeated zooming in of smaller sub-portions of the whole initial grid is often applied to catch small size objects like galaxies. However, this procedure is quite expensive in terms of computational resources. Other strategies have been adopted. In particular, an isolated perturbation is artificially created and evolved without following the evolution of the much larger region of space in which it is located. (See for instance [1,134,135], and references therein). In brief, one proceeds as follows:

(i) A given cosmological model of the Universe is assumed. [1] adopt the Λ-CDM concordance cosmology, with values inferred from the WMAP-5 data [159]: flat geometry, $H_0 = 70.1$ km/s/Mpc, $\Omega_\Lambda = 0.721$, $\Omega_b = 0.046$ (giving a baryon ratio of $\simeq$0.1656), $\sigma_8 = 0.817$, and $n = 0.96$.

(ii) The growth of primordial perturbations is followed by means of COSMICS [160]. However, since we are not interested here to a full cosmological simulation containing perturbations at all scales, but only to a portion of it containing perturbations with assigned over-density, mass, and dimensions chosen a priori, the size of the sub-portion is fixed in such a way that the wavelength of the perturbation corresponding to the chosen over-density and mass is similar to (but suitably smaller than) the size of the sub-portion. The aim is to construct a reference proto-halo containing DM and BM particles in the right proportions, each of which with its own known mass, position and velocity vector. This reference proto-halo, instead of being constructed by hand as in [23], is now derived coherently with the chosen

cosmological scenario. Casting the problem in a different way, instead of searching within a large scale realistic cosmological box the perturbation most suited to our purposes, we suppose that a perturbation with the desired properties is already there, and derive the positions and velocities of all its DM and BM particles from a self-consistent, small-size cosmological box tailored to the perturbation we have chosen.

(iii) This reference halo corresponds to the largest mass of the whole sample of galaxy models calculated by [1]. The grid containing the density perturbation has the size of $\mathcal{L} = 9.2$ comoving Mpc on a side, and is populated by 46^3 particles. The regular positions of the particles are perturbed by COSMICS consistently with cosmological random gaussian fluctuations. Furthermore, a density peak is constrained to form at some very early epoch a virialized structure near to the center of the box (COSMICS allows us to specify the properties of the constrained density peak to model the density field in the desired way). A gaussian spherical over-density is imposed with average linear density contrast $\delta\rho = 3$, smoothed over a region of radius 3.5 comoving Mpc. We remind the reader that the linear density contrast is defined as $< \rho > /\rho_{bg} - 1$ (where ρ_{bg} is the average matter density of the Universe), and it can be extrapolated beyond the linear regime; it would be equal to 1.86 at the epoch of virialization. Requiring a higher value in COSMICS simply bounces back in time the epoch of virialization.

(iv) Starting from these input assumptions, COSMICS returns the initial comoving positions and the initial peculiar velocities of the particles at the time in which the highest density perturbation is exiting the linear regime (*i.e.*, it has $\rho/\rho_{bg} - 1 = 1$). This is an important point to remember. COSMICS is used only up to the exit from the linear regime. The subsequent evolution of the DM and BM haloes during the non-linear regime is followed by NB-TSPH simulations.

(v) The small cosmological box containing the perturbation eligible to become a galaxy is an approximation of the local Universe, the one subsequently affecting the evolution of the perturbation itself. The validity of this approximation will be examined in some detail below. To avoid numerical problems with sharp edges, a sphere of radius $r = \mathcal{L}/2$ centered on the center of the box is singled out, the particles coordinates are changed from comoving to proper physical values (this is simply achieved by dividing the comoving value by the initial cosmological expansion parameter $a = 1/z_i - 1$, where z_i is the initial redshift provided by COSMICS at the end of the linear regime), and a radial outward directed velocity component is added to each particle. This component of the velocity is proportional to the radial position of the particle and the initial redshift of the simulation. This velocity mimics the effects of the outward directed Hubble flow, to take the expansion of the Universe into account. (Alternatively, the equations of motion could be modified to account for the expansion. However, while this is straightforward to do in a comoving frame, it is less commonly done in physical coordinates. Moreover, virialized structures are no longer subject to the expansion of the Universe and should be described by static coordinates. Examples of the method we adopt are given in [161,162] and in other similar studies.)

(vi) To obtain the initial conditions for other model proto-haloes (galaxies) with different mass and/or mean initial densities, one starts from the reference High Density, High Mass (HDHM) halo, see also the heading of Table 1 for the explanation of the acronyms used to identify the model galaxies, and proceeds as follows:

Varying the mass. If the spatial dimensions of the box are changed, COSMICS modifies in a self-consistent fashion the size and consequently the mass of the haloes, leaving, however, the mean

density unchanged. Playing with this, a number of proto-haloes with the same mean density but smaller mass and consequently radius are generated. The initial redshifts of the proto-haloes with equal initial density but different mass are different from one another, because the exit time (redshift) from the linear regime is a function of the mass of the perturbation.

Table 1. Initial parameters and final properties (at the last computed stage of their evolution) of the NB-TSPH galaxy models. From left to right: the model identification code [xDyM, where D stands for density and M for mass; x stands for H (high), I (intermediate), L (low) and VL (very low)], the initial total halo mass M_h, the initial total baryon mass (in form of gas) $M_{g,i}$, the relative over-density with respect to the background density when the primordial perturbations exit the linear regime ($[\Delta\rho]_n = \frac{\delta\rho - \rho_u}{\rho_u} - 1$), the redshift z_i at which the proto-halo is sorted out of the background, the associated proper radius R_h, the redshift z_f of the last computed model, the age t_f at the same stage, the total galaxy mass M_s in stars, the total mass (DM + gravitationally bound BM) of the virialized halo M_{vr}, the associated virial radius R_{vr} (for all models virialization roughly occurs at about 2 Gyr), the ratio of the total star mass to the virial mass M_s/M_{vr}, the ratio of the total star mass to initial gas mass $M_s/M_{g,i}$, the half star-mass radius $R_{s,1/2}$, the axial ratio $(b/a)_{XY}$ of the stellar system projected on the XY plane. Times are in Gyr, masses in solar units $M_\odot$, and radii in kpc.

Model	M_h	$M_{g,i}$	$[\Delta\rho]_n$	z_i	R_h	z_f	t_f	M_s	M_{vr}	R_{vr}	$\frac{M_s}{M_{vr}}$	$\frac{M_s}{M_{g,i}}$	$R_{s,\frac{1}{2}}$	$(b/a)_{XY}$
HDHM	1.75×10^{13}	2.90×10^{12}	0.39	46.3	97.2	0.22	11.0	7.5×10^{11}	1.5×10^{13}	153.0	0.050	0.26	15.6	0.56
IDHM	1.75×10^{13}	2.90×10^{12}	0.30	39.2	114.3	0.77	8.0	7.4×10^{11}	1.5×10^{13}	141.8	0.050	0.26	16.5	0.48
LDHM	1.75×10^{13}	2.90×10^{12}	0.23	33.2	134.5	0.50	8.7	7.3×10^{13}	1.5×10^{13}	133.8	0.049	0.25	15.8	0.57
VLDHM	1.75×10^{13}	2.90×10^{12}	/	22.7	194.3	0.83	6.6	6.3×10^{11}	1.3×10^{13}	112.5	0.048	0.22	11.2	0.52
HDIM	2.69×10^{11}	4.45×10^{10}	0.46	53.8	21.0	1.00	5.8	2.0×10^{10}	2.1×10^{11}	37.6	0.100	0.45	5.7	0.62
IDIM	2.69×10^{11}	4.45×10^{10}	0.33	45.6	24.7	0.75	7.0	1.9×10^{10}	2.1×10^{11}	35.7	0.080	0.43	5.8	0.63
LDIM	2.69×10^{11}	4.45×10^{10}	0.25	38.6	29.0	0.58	8.1	1.9×10^{10}	2.0×10^{11}	33.3	0.100	0.42	5.2	0.75
VLDIM	2.69×10^{11}	4.45×10^{10}	/	26.4	42.0	0.15	11.8	1.7×10^{10}	1.4×10^{11}	28.3	0.120	0.38	4.9	0.83
HDLM	4.18×10^{9}	6.92×10^{8}	0.54	63.2	4.5	0.36	9.7	1.5×10^{8}	3.3×10^{9}	9.2	0.045	0.19	2.3	0.74
IDLM	4.18×10^{9}	6.92×10^{8}	0.39	53.6	5.3	0.22	11.0	1.4×10^{8}	3.3×10^{9}	10.0	0.040	0.16	2.4	0.67
LDLM	4.18×10^{9}	6.92×10^{8}	0.29	45.4	6.2	0.05	13.0	1.4×10^{8}	3.2×10^{9}	11.8	0.040	0.19	2.1	0.79
VLDLM	4.18×10^{9}	6.92×10^{8}	0.16	31.1	8.9	0.00	13.7	1.0×10^{8}	3.0×10^{9}	10.5	0.030	0.10	2.7	0.65

Varying the density. The procedure to generate haloes with the same mass but different initial mean density is more complicate. *Before* perturbing the positions (and velocities) of the particles in the grid, we artificially decrease the densities at each grid point, thus varying the average density, but conserve the total mass. Since the initial conditions are produced at the moment in which the highest perturbation peak exits the linear regime, the initial spatial configuration is still a superposition of independent plane waves with different wave-numbers and random phases, *i.e.*, a *gaussian field* with $\delta(\vec{q}) = \sum_{\vec{q}} \delta_{\vec{k}} \exp(i\vec{k}\cdot\vec{q})$, where $\vec{k}$ is the wave-number and $\vec{q}$ is the Lagrangian coordinate corresponding to the unperturbed comoving position of a mass element. Dividing the local (over-)densities $\delta(\vec{q})$ by a constant factor f returns a self-similar gaussian field in which the Fourier coefficients $\delta_{\vec{k}}$ are divided by the same factor, implying that the variance $\sigma^2 \propto \sum_{\vec{k}} \delta^2_{\vec{k}}$ of the perturbation is reduced by a factor f^2. COSMICS subsequently computes the effective displacement and velocities of the particles via the Zel'dovich approximation $\vec{x}(\vec{q}) = \vec{q} + D_+\vec{d}(\vec{q})$ and $\vec{v}(\vec{q}) = \dot{D}_+\vec{d}(\vec{q})$, where the displacement field $\vec{d}(\vec{q})$ is given by the relation $\vec{\nabla}\cdot\vec{d} = -D_+^{-1}\frac{\delta\rho(\vec{q})}{\rho}$, and D_+ is the cosmic growth factor at the initial redshift, which in turn depends on the cosmological model. To obtain *intermediate density* haloes, the mean density of the reference halo is decreased by a factor of 15%. The mean density of these latter is then decreased by

another 15% to obtain *low density* haloes. Therefore, these latter have an initial mean density which is 72.25% of the value of the initial reference halo. Finally, a set of haloes with very low initial over-density was obtained reducing the mean density by 50%. The different densities can be considered as a way to mimic the possible environments in which a proto-halo begins to form.

(vii) At this stage, a minimal amount of solid-body rotation is also added to all the particles in the proto-haloes. The solid-body rotation is represented by the spin parameter:

$$\lambda = \frac{J|E|^{1/2}}{GM^{5/2}} \tag{1}$$

where J is the angular momentum, E is the initial binding energy, and M the total mass of the system. Typical values of λ range from 0.02 and 0.08 [163], which corresponds to angular velocities of the order of fractions of a complete rotation over time-scales as long as about ten *free-fall* time-scales [156]. We adopt $\lambda = 0.02$. The choice is motivated by the fact that our model galaxies are meant to represent ETGs. This issue will be also shortly commented in general remarks of this section.

(viii) Finally, each particle in each proto-halo is split into a DM and a BM particle (gas), th2 latter with a small displacement from its original position to avoid numerical divergences. Indicating with m_0 the mass of the original particle and with $f_{BD} = \rho_{BM}/\rho_{DM} \simeq 0.1656$ the cosmological ratio between the BM and DM densities, we assign to each gas particle the mass $m_{gas} = f_{BD} \times m_0$. Consequently, $m_{DM} = (1 - 0.1656) \times m_0$. The final HDHM proto-halo consists of ≃58,000 DM particles plus an equal number of gas particles.

General remarks. We point out that all the proto-haloes we have chosen are fully consistent with the underlying cosmological background. The expected DM halo mass function follows the laws by, e.g., [164] or [165], and/or the analytical fits of numerical simulations (e.g., [166]). In this picture, a $M \simeq 10^{13} M_\odot$ halo is becoming "typical" on a ∼10 Mpc scale (the typical linear size of a large galaxy cluster) at redshifts below $z \sim 5$, which is compatible with the collapsing redshift of our HDHM model (see below). Such massive haloes are also expected not to be rare on ten times larger scales at $z \sim 10$. This can be easily checked considering the halo growth functions of DM haloes for the concordance Λ-CDM cosmology: the expected number of haloes with mass $\simeq 10^{13} M_\odot$ within a volume of 1 (Mpc/h)^3 at $z \sim 10$ is $n \simeq 10^{-8}$ (see Figure 2 of [122]).

The main criticism that could be made to the above procedure is that the size of the simulation backing the perturbation in question is too small (9.3 comoving Mpc on a side for the HDHM box, and consequently smaller in the other cases). It is known from long time that the simulation size determines the maximum perturbation wavelength. If the long wavelengths are dropped out, the strength of subsequent clustering is reduced, but at the same time the number density of intermediate mass haloes (with total mass of the order of $10^{13}\ h^{-1} M_\odot$ in our case) is enhanced [167]. While this may be a problem in real cosmological simulations, in our case it is not so, because we are interested in objects with the mass and size of galaxies and not of galaxy clusters. Furthermore, [167] show that truncation of the initial power spectrum (*i.e.*, the small size) of the simulation has little impact on the internal properties of the haloes. However, truncation lead to spin parameters that are 15% lower than usual. We have in a sense avoided the whole spin problem just by taking the lowest value for the spin parameter ($\lambda = 0.02$) suggested by [163], a reasonable approximation for slowly rotating systems such as ETGs. A final remark could be made on the fact that adopting a sphere of radius $r = l/2$ (about the size of the Local

Group) as the starting proto-halo we implicitly neglect the possibility of late infall of nearby haloes that initially were outside the sphere may occur. This would inhibit late refuelling of gas (and stars and DM) to our system that is equivalent to say that we inhibit late mergers likely accompanied by star formation. This indeed is not the aim of the present study, which intends to explore the modality of star formation in alternative to the very popular hierarchical scheme. To conclude, the scheme we propose to derive the initial conditions for our model galaxies is not in conflict with the cosmological paradigm and it is easy to implement in NB-TSPH simulations.

In view of the discussion below, there is a point to clarify in relation to the gas density at which star formation is supposed to occur. The cosmological mixture of DM and BM in the proto-halo of mass $M_h = M_{DM} + M_{BM}$, where $M_h \simeq M_{DM}$, and radius R_h collapses when the density contrast with respect to the surrounding reaches a suitable value given by:

$$\rho_h \equiv \left[\frac{3M_h}{4\pi R_h^3}\right] \geq \lambda \rho_u(z) \tag{2}$$

where $\rho_u(z)$ –$\propto (1+z)^3$– is the density of the Universe at the redshift z, and λ the factor for the density contrast of the DM halo. The factor λ depends on the cosmological model of the Universe (see [168], for all details). During the collapse, DM and BM are dragged together to higher and higher densities and only when the gas density exceeds a threshold value, $\rho_g > \rho_g^*$, star formation is supposed to start. Therefore during the overall collapse, BM under the action of radiative cooling may reach densities much higher than those reached by the dissipation-free DM. In other words the volume occupied by the bulk of gas and subsequently stars, can be much smaller than that of DM. The immediate consequence of it is that the initial dimensions of the proto-halo will not correspond to those of the stellar component built inside. All this will affect the final MRR of galaxies (see below). This allows to evaluate the effect of local initial density, *i.e.*, the density of BM (gas/and or stars) resulting from BM (gas) cooling inside the DM potential well. We name this the local initial density to distinguish it from the cosmological density at which the collapse of the proto-halo begins.

4.2. Star Formation

This is modeled by means of the stochastic method proposed by [158,169]. First, only gas particles belonging to convergent flows (*i.e.*, $\nabla \cdot v < 0$) and denser than the threshold density $\rho_g^* = 5 \times 10^{-25}$ g/cm^3 are considered eligible to form stars. No restriction on the temperature is imposed because thermal instabilities can produce star forming sites even within high temperature gas. If a gas particle satisfies these criteria, it is assumed to form stars at the rate:

$$\frac{d\rho_s}{dt} = \epsilon_{sf} \frac{\rho_g}{t_{ff}} \tag{3}$$

where $t_{ff} \simeq 0.5/\sqrt{G\rho_t}$ is the free-fall time, ρ_t the local total mass density (DM plus BM), and ϵ_{sf} the dimensionless efficiency of the star formation process. This means that a gas particle is expected to turn a fraction ϵ_{sf} of its mass into stars over its free-fall time scale. However, a stochastic description of the star forming process is adopted to avoid the creation of an exceedingly large number of star particles. Thus, gas particles undergo a Monte Carlo selection to check whether or not they will actually form stars, in such a case they are instantaneously turned into collision-less star particles (see also [136,158]).

Empirical estimates of the efficiency of star formation based on observational data of star forming events inside the molecular clouds in the local vicinity yield $\epsilon_{sf} \simeq 0.025$ [170,171]. In this case the gas density and free-fall time scale are those of the cold molecular clouds. However, for the large scale star formation mechanism in a galaxy, the above estimate may not correspond to reality. As a matter of fact, considering that a typical galaxy with $10^{11} M_{\odot}$ mass in stars has to disposal a time scale of about 13 Gyr to build up its stellar content, the mean estimate of the star formation efficiency is closer to 0.1 rather than 0.02. The new estimate would increase by nearly a factor of ten if the time to disposal to form stars is much shorter than 13 Gyr, say 1 to 2 Gyr (as suggested by the age of the bulk of stars in many ETGs). In addition to this, it is not known whether ϵ_{sf} remained constant during different cosmic epochs due to the different mechanisms that form stars in metal-poor regions at high redshifts and in the molecular clouds of the local pool. Finally, it is not known whether the efficiency of star formation is the same in all galaxies independently of their mass (either total or baryonic). For all these reasons, [1] preferred to adopt $\epsilon_{sf} = 1$, *i.e.*, the process of star formation occurs at 100% efficiency (this means that *all* gas particles satisfying the star forming criteria will turn their total mass into stars within a free-fall time scale). The main motivation stands on the following considerations. Several numerical simulations calculated with different values of ϵ_{sf} clarify that within a certain range of values, the SFHs of the models with small values of ϵ_{sf} are apparently quite similar to those with ϵ_{sf} = 1, the only difference being that small values of ϵ_{sf} lead to much more time-consuming simulations. The reason is that dense and cold clumps of matter, interacting with hotter material heated up by nearby SNa explosions, require extremely small time-steps. In contrast, if the gas can easily form stars, this critical situation is avoided, and the simulations proceed much faster. The weak impact of ϵ_{sf} on the final SFH can be attributed to the self-regulation cycle between star formation and energy feedback. A high star formation efficiency implies a strong and sudden burst of stellar activity; but young stars soon pressurize their surroundings via energy feedback, quenching the formation of new stars. However, if the gas is sufficiently dense, radiative cooling is effective and further star formation can soon take place (positive feedback). With a low efficiency, fewer stars can form. Their heating is consequently lower, and more stars can soon form *before* feedback could halt the whole process. This ultimately leads to the same situation as in the previous case, with perhaps the minor consequence of a delayed enrichment in heavy elements of the medium. Clearly, other parameters play a more important role; for example, the density threshold ρ_* and the efficiency of feedback. Therefore the choice ϵ_{sf} = 1 and likely fast calculations is the best compromise. However, one should always keep in mind that adopting ϵ_{sf} = 1 may have other consequences on the dynamical evolution of the systems, favoring the collision-less collapse instead of the dissipative one.

4.3. Cooling, Energy Feedback, Interstellar Medium, and Chemical Enrichment

Radiative cooling. The cooling functions for atomic radiative processes are from [73,156]. In brief, for temperatures greater than 10^4 K they lean on the [172] tabulations for a plasma in equilibrium conditions and with metal abundances $\log[Z/Z_{\odot}]$ from -10 (no metals) to 0 (solar) and 0.5. For temperatures in the range $100 < \mathrm{T} < 10^4$ the dominant source of cooling is the H_2 molecule becoming rotationally and/or vibrationally excited through a collision with an H atom or another H_2 molecule and

decaying through radiative emission [102,173], amalgamated together by [73]. Finally, for temperatures lower than 100 K [73,156], starting from the studies of [174,175], incorporate the results of [173,176] for the CO molecule as the dominant coolant. Finally, the contribution by inverse Compton cooling (see e.g., [177]) is included.

Energy feedback. When a gas particle is turned into a star particle, it can be considered to represent a SSP made of many real stars. It starts re-fueling the ISM with heavy chemical elements and energy, mainly because of winds from young massive stars and SNa explosions.

Winds. We consider two regimes for the energy injection by winds. When the SSP is young, the main source of energy are the young massive stars. Their winds have very high speeds, typically from 1000 to 3000 km/s. Here we adopt a constant velocity of $v_{YSO} = 1500$ km/s. The kinetic energy of the winds is assumed to be thermalized and released within the surrounding medium with an efficiency of 20% (see e.g., [178]). In the late stages of the SSP evolution, slow velocity winds from low mass stars become predominant; in these case we assume the wind speed of $v_{OSO} = 60$ km/s (typical of RGB stars), and the same thermalization efficiency.

SN explosions. Each *real* SN explosion is expected to deposit some 10^{51} kinetic ergs in a very small region, and on a short time scale. However, most of this energy is soon radiated away, and only a small fraction of it is subsequently thermalized. We use the results by [179] to obtain an analytic approximation of the fraction of the initial energy which becomes available at the end of the expanding phase of the SN bubble. However, in the real Universe SN explosions take place in already shock-heated regions, with temperatures raised up to some 10^6 K, due to the photo-ionizing flux from massive young stars, stellar winds, and previous SN explosions. All this is not taken into consideration in Thornton's study, so a large uncertainty still affects the description of the whole process (see [180], for an exception). A single star particle represents an entire SSP, so a large number of SNa explosions are expected to take place within a single star particle over a rather long time scale. The number of SNa explosions, as well as the amount of gas released by a SSP of given age and mass during a time-step and its chemical composition are computed with the technique described in [158]. In our description each SSP continuously releases gas and energy at each time step, becoming a *hybrid* particle (made of gas and stars). Finally, the total budget of thermal energy produced by stellar winds and SNa explosions is given continuously to the gas reservoir attached to each star particle. This reservoir, due to its high temperature, acts a piston on the neighboring particles, effectively injecting kinetic energy into the surrounding ISM.

Chemical enrichment. Stellar gaseous ejecta contain heavy elements that are redistributed within the surrounding gas by means of a diffusive process. In practice, the amounts of heavy elements ejected by each SSP, *i.e.*, star particle, is computed at each time-step by means of the [181] SNa. The total elements ejected by a single SSP at each time step is the sum of three contributions: (i) the elements locked in the dying stars at the moment of their birth, inherited from the proto-stellar gas; (ii) the heavy elements created in the core by thermonuclear reactions and ejected in Type II SNa explosions; (iii) the elements created in the core of binary stars terminating their life as Type Ia SNa (see [158], for all details). Numerically, the heavy elements released by a SSP are assigned to the gaseous mass ejected by the same SSP during the current time-step and subsequently spread over neighboring particles by means of a diffusion algorithm based on the Fick's law in spherical symmetry (see [155]).

Interstellar Medium: Multi-dimensional space of physical states. The thermodynamical and chemical treatment of the ISM in NB-TSPH simulations is difficult to model. References [182,183] proposed a method to include the ISM in NB-TSPH simulations and to get the cooling rate as a side self-consistent product. The idea is as follows: at a given time, the physical conditions of "a unit volume" of the ISM made of gas and dust in arbitrary proportions are specified by a pattern of parameters such as temperature, density chemical compositions *etc.*, *i.e.*, a point in the hyper-space of these parameters. After a certain amount of time has elapsed, the same volume has evolved to another state characterized by another pattern of same parameters, *i.e.*, another point of the above hyper-space. We may consider this as a displacement vector. Consequently, if a large volume of this hyper-space is explored in advance, we would know at any arbitrary time all possible physical states in which the ISM can be found and the vector field of all possible displacements from an arbitrary initial stage to a final stage. In reality during its evolution, an elemental cell of the ISM will follow a path in the above hyper-space; at each step a final stage is the initial one of the next step and all are connected by the vector field. This view is particularly suited to implement the treatment of the ISM into NB-TSPH simulations provided that the vector field is taught in advance to a Multiple artificial Neural Network (MaNN). For all "NB-TSPH particles" of a simulation, the physical conditions at time t are fed to the MaNN which restitutes the new physical conditions at time $t + \Delta t$. The evolution of the ISM is taken into account at a modest computational cost, contrary to what it would be if the ISM evolution is incorporated into the NB-TSPH calculations. All details concerning the model of the ISM, the companion code named ROBO (little thing in venetian dialect), and the MaNN can be found in [182,183]; they are not repeated here for the sake of brevity.

4.4. NB-TSPH Galaxy Models: Results

Stirring baryons in the gravitational pot. The Duty Cycle between ISM and stars in a galaxy can be reduced to the following duty cycle: stars are born and evolve ⇒ stars inject energy and metals into the ISM by UV radiation, stellar winds, and SNa explosions ⇒ gas heats up by energy injection and shocks and enriches in metals ⇒ gas cools down by radiative processes ⇒ gas collapses ⇒ new stars are born. The pot inside which all this occurs is the gravitational potential well. Therefore, the total galaxy mass and initial density are the key parameters. For all details see [1,23].

Histories of Star Formation. Reference [23] using NB-TSPH monolithic-like models with simple initial conditions demonstrated that at given initial over-density the SFH changed from a single dominant initial episode monolithic to bursting-like mode at decreasing total mass, whereas at given total mass the SFH changed from a dominant initial episode to bursting mode at decreasing initial over-density. The trend is shown in the panels Figure 9. This basic dependence of the SFH on the total galaxy mass and initial over-density (environment) has been amply confirmed over the years by many observational and theoretical studies and it is also confirmed by the models calculated by [1] adopting cosmological initial conditions (see above) whose SFH is shown in Figure 10.

Downsizing and delayed star formation are naturally reproduced. Furthermore according to our assumption for the SFR (proportional to the ratio of the gas mass to the free-fall time scale t_{ff}), the SSFR is simply the inverse of t_{ff}. All this strongly suggests that the gravitational potential well of BM + DM drives the whole process and dictates the efficiency and duration of the SF process. A galaxy,

thanks to its gravitational potential knows in advance the kind of stellar populations (very old or spanning a large age range) it is going to build up.

Figure 9. The SFR as function of time in the model galaxies by [23] that are calculated with rather simple initial conditions. For all the models they assumed redshift of the initial collapse $z_{for} = 5$ and Hubble constant $H_0 = 65$ km s^{-1} Mpc^{-1}. We show here the model of their case B that are particularly useful to highlight the effect of the mass at given initial over-density, and the effect of initial over-density at given total mass. (**a**) The mass dependence of the SFR of models B as a function of time at given initial over-density. From the bottom to the top, the SFRs refer to galaxies with $M_h = M_{DM} + M_{BM}$ equal to 1×10^8 $M_\odot$, 1×10^9 $M_\odot$, 1×10^{10} $M_\odot$, 2×10^{11} $M_\odot$, 1×10^{12} $M_\odot$, $5 \times 10^{12} M_\odot$ and 5×10^{13} $M_\odot$. The initial baryonic and dark mass are $M_{BM} = 0.1\, M_h$ and $M_{DM} = 0.9\, M_h$, respectively; (**b**) the SFR of intermediate and low mass B-type galaxies of the same mass but slightly different initial over-density. The mass is $M_h = 10^9$ $M_\odot$. The initial over-density goes from low (LD) to intermediate (ID) to high values (HD) as indicated. Reproduced with permission from [23]. Copyright 2002 John Wiley & Sons.

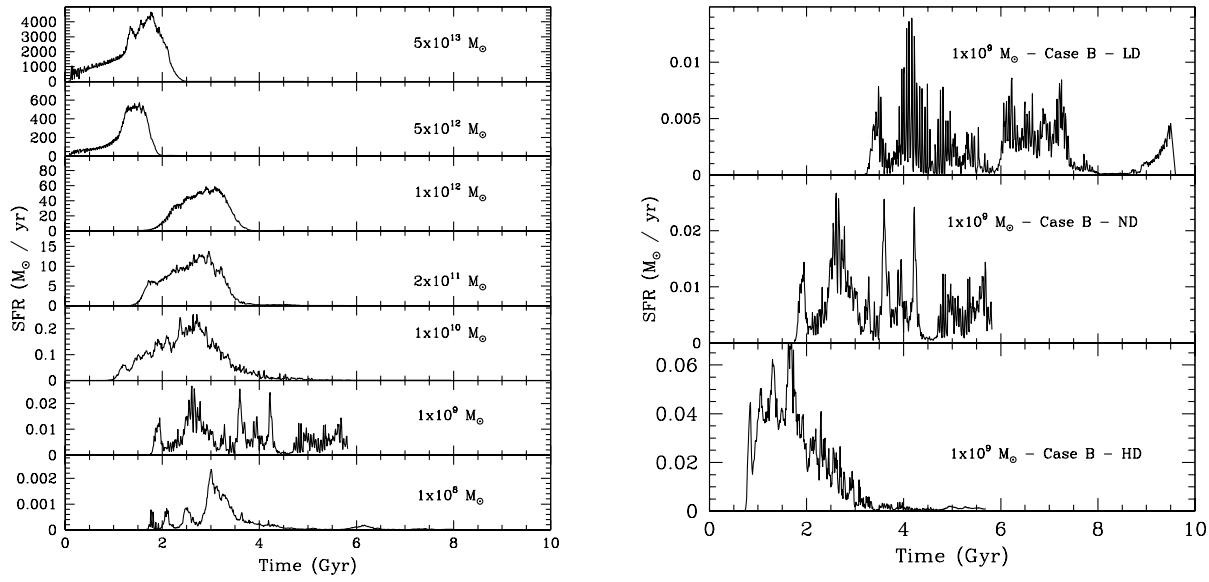

(**a**) (**b**)

Assembling the Stellar Mass. In the panels of Figure 11 we show the gradual building up of the stellar mass of a galaxy as a function of the redshift. Remarkably the massive galaxies build up their stellar content earlier than those of smaller mass and also earlier than redshift $z = 2$. Looking at the entries of Table 1 and the results of [23] the net efficiency of the star forming process and the duty-cycle above are such that on the average 20% of the initial BM is converted into stars, the rest is either expelled in form of galactic winds or heated up and parked away for future use.

Stellar ages. The distribution of the galactic ages ($T_{G,i}$) at which the star particles are created as a function of the radial distance is shown in the left panel of Figure 12 limited to the high and low mass models (the behavior of the intermediate mass ones is in between the two). The real ages of the star particles are $T_{*,i} = T_G - T_{G,i}$. In early epochs, the stars are preferentially created in the central regions,

then the star forming activity expands to larger radii (inside-out mechanism), and moving towards the present time, the stellar activity tends to shrink again towards the center. This simply mirrors the SFH and the mechanism of mass assembly presented above.

Figure 10. The SFR *versus* time for the models of [1] framed in the Λ-CDM model of the Universe and with fully cosmological initial conditions. The input data and parameters for these models are described in the text and listed in Table 1. The SFR is in solar masses per year and the time is in Gyr. Left to right: high density, intermediate density, low density, very low density. (**a**) high masses; (**b**) low masses. Reproduced with permission from [1]. Copyright 2012 John Wiley & Sons.

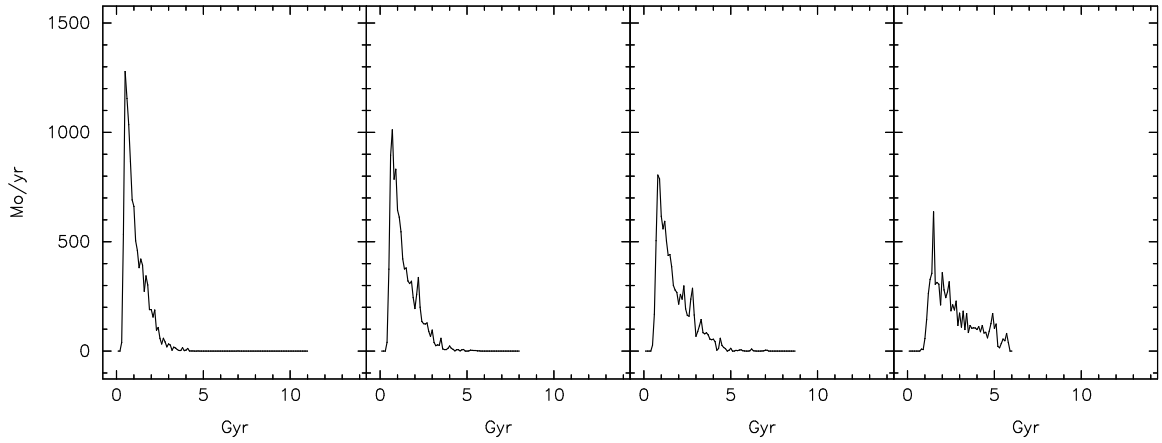

(**a**)

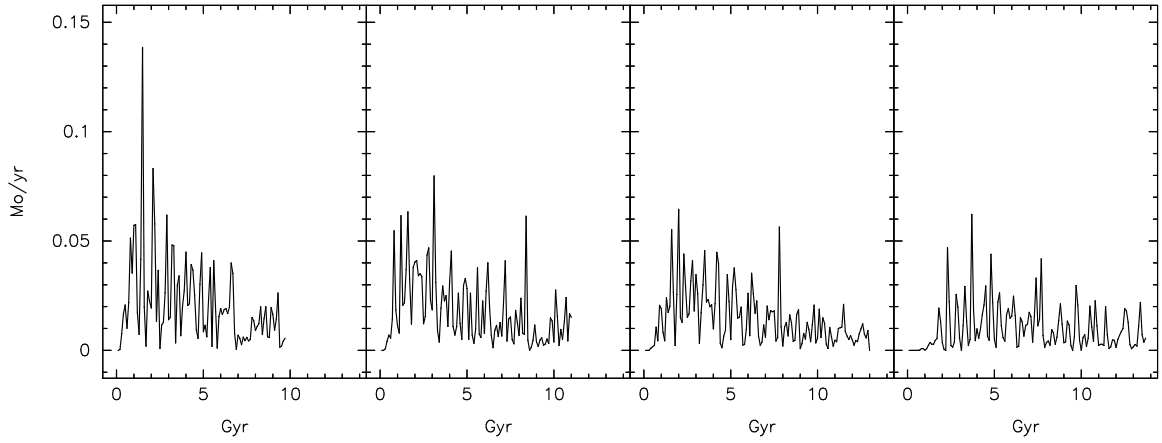

(**b**)

Mean metallicity. Turning now to the metal content reached by the model galaxies, we look at the average stellar metallicity as a function of the total stellar mass. The results are shown in the right panel of Figure 12 where the red circles refer to all the star particles, whereas the blue ones only to those within the central 5 kpc of each model. The black lines are the median (solid) and the 16th and 84th percentiles (dashed) of the data presented in [184]. Observational data and theoretical results agree only marginally. The absolute values of the theoretical metallicities are too low compared with the observational estimates, in particular for the most massive models which are almost an order of magnitude too metal-poor. This may be due to several factors: (i) The theoretical values are straightforwardly computed averaging the metallicity of all particles within the galaxy radius without any

further refinement, whereas the observational metallicity are *luminosity weighted*; (ii) Use of different methods to obtain observational and theoretical metallicities; (iii) The adopted IMF may not be suited to ETGs. For example, IMFs tailored to fit the solar vicinity (e.g., Kroupa), may underestimate the enrichment by massive stars in other environments. Recent studies seem to indicate that the IMF in massive ETGs is more skewed toward massive stars than commonly assumed [185] thus implying a net increase of metal production by massive stars in these systems; (iv) The high star formation efficiency may play a role, favouring the formation of low metallicity stars at early times and reducing the average metallicity of the models; (v) Finally, at least part of the observed color- (and hence metallicity-) mass relation might just be a spurious consequence of an aperture effect on the observational data (see [186], for a detailed discussion). In conclusion, considering that chemical enrichment in NB-TSPH simulations is still far from being fully satisfactory, we are inclined to say that theory and data marginally agree each other.

Figure 11. Evolution of the mass assembly in the reference models. The X axis lists the models ordered as in Table 1 (the acronyms have been shortened for reasons of space). (**a**) The Y axis displays the percentage p of assembled stellar mass at a given redshift z with respect to the $z = 1$ stellar mass; red: $z = 10$; blue: $z = 5$; green: $z = 2$; black: $z = 1.5$; (**b**) the Y axis displays the redshift z at which a given percentage p of the total stellar mass at $z = 1$ was assembled; red: $p = 50\%$; black: $p = 99\%$.

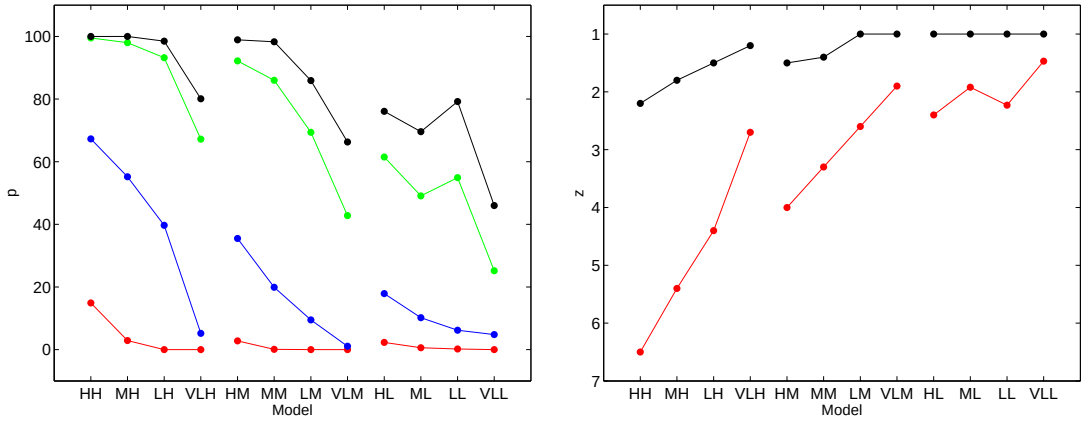

(**a**) (**b**)

Metallicity gradients. Radial gradients in spectro-photometric properties of ETGs are known to exist (see e.g., [187,188], and references therein), which are ultimately attributed to age and metallicity gradients of the constituent stellar populations (e.g., [12]). To this aim, for each model galaxy, reference [1] calculate the median-binned metallicity profile, expressed as $\nabla_Z = d\log Z/d\log R$ over the radial interval $0.1\,R_e$ to $1\,R_e$. The gradient ∇_Z is calculated by applying three different weighting schemes, where each particle was assigned no-weight, mass-weighted, and luminosity-weighted. The results of Table 2 show that no significant differences exist within the errors, especially at the high mass end. Looking at the results in some detail, high- (low-) mass models exhibit metallicity gradients spanning the range from -0.4 (-0.02) to -0.27 (0.16), depending on the weighting scheme and environment. In general, low-density models tend to have more negative metallicity gradients. Moreover, at given density, high- (relative to low-) mass systems have more negative gradients.

Table 2. Metallicity gradients of four ETG models in the radial range of $0.1\ R_{eff}$ to $1\ R_{eff}$. Column 1 is the model ID label. Columns 2, 3, and 4, correspond to cases where the ∇_Z is computed with no-weight, mass-weight, and luminosity-weight assigned to each particle. Errors are the rms of ∇_Z estimates among 100 projections of each model.

ID (1)	∇_Z (no-weight) (2)	∇_Z (mass-weighted) (3)	∇_Z (lum-weighted) (4)
LDHM	-0.39 ± 0.04	-0.40 ± 0.04	-0.33 ± 0.03
HDHM	-0.32 ± 0.04	-0.31 ± 0.04	-0.27 ± 0.03
LDLM	0.00 ± 0.04	$+0.01 \pm 0.02$	0.00 ± 0.06
HDLM	$+0.09 \pm 0.02$	-0.02 ± 0.01	0.16 ± 0.03

Figure 12. (**a**) Ages (in Gyr) of the "star particles" *versus* the radial positions (distance from the barycenter in kpc) for the high (top row) and low mass models (bottom row) and decreasing density from left to right at the final time-step of their evolution. The radial distance is calculated from the barycenter of the stellar system (kpc). The virial radii of the stellar systems are similar to the extension along the X axis; (**b**) Averaged metallicity $\log[Z/Z_\odot]$ *versus* stellar mass $\log M^*$ $[M_\odot]$ for the models of Table 1, compared to the observed mass-metallicity relation. Black lines: data from [184] (solid line: median distribution of their sample; dashed lines: 16th and 84th percentiles). Red open circles: averaged metallicity of all stellar particles in each model. Blue open circles: averaged metallicity within the inner 5 kpc in each model. Reproduced with permission from [1]. Copyright 2012 John Wiley & Sons.

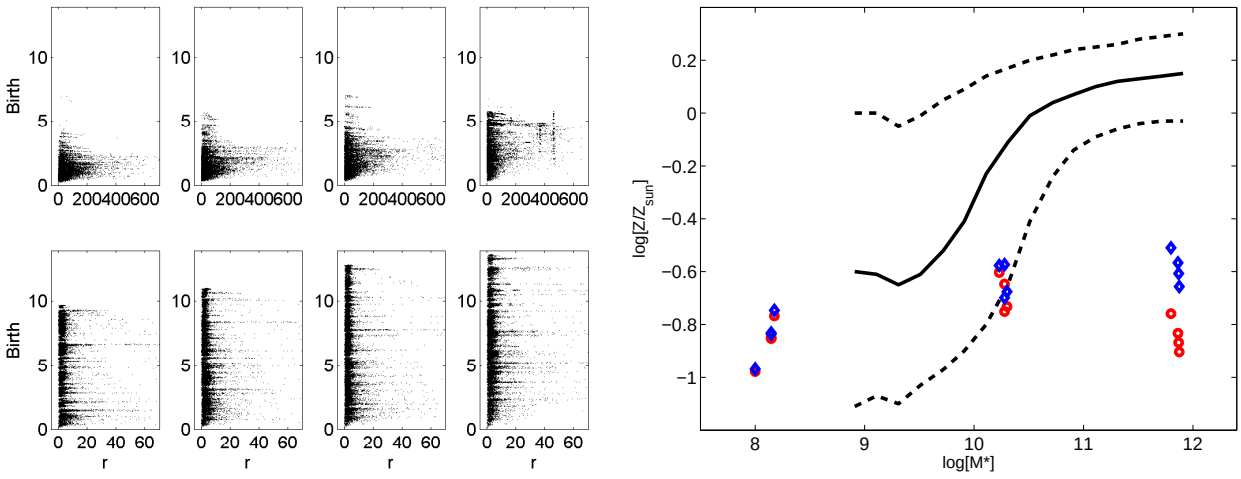

(**a**) (**b**)

Although the metallicities of our models do not match observations in an absolute sense, the relative variations of metallicity (between, e.g., different masses, and/or different galacto-centric distances) are likely more robust, as they are less dependent on the absolute calibration of the ingredients the models rely on. This motivates for a comparison of the predicted ∇_Zs with observational results. A steepening of the metallicity gradient with galaxy mass, qualitatively consistent with that seen in our models, has

been reported by [187,188]. For a galaxy mass of $3 \times 10^{11}\, M_{\odot}$ (similar to that of $\sim 7 \times 10^{11}\, M_{\odot}$ of models HDHM and LDHM), they estimate metallicity gradients of -0.37 ± 0.02 and -0.41 ± 0.02 for low- and high-density ETGs, respectively. At low density, the estimate is fully consistent with our model predictions. At high-density, the models exhibit shallower gradients, by ~ 0.07, in contrast to the data, where a (marginal) difference of -0.04 ± 0.03 is found. For what concerns low-mass models, they exhibit almost null gradients, consistent with the observational finding of [189] that $\nabla_Z \simeq 0$ at a galaxy mass of $\sim 10^9\, M_{\odot}$. Despite these results seem to indicate agreement between models and (some) available data-sets, the whole subject is open to future investigation.

Galactic Winds. The models eject conspicuous amounts of metal-enriched gas in form of galactic winds over their whole history. In the left panel of Figure 13 we display the radial velocities of the gas particles in the case of HDHM model as a function of the radial distance at three different epochs and compare to the escape velocity (the blue solid lines). The HDHM galaxy undergoes a single, sharply peaked episode of star formation centered at the rest-frame age of 1 Gyr with peak value of about 1300 $M_{\odot}/yr$ and mean duration of about 2 Gyr, which triggers an almost explosive ejection of a galactic wind whose gas particles may reach velocities as high as about 1500 km/s. During the star formation activity SNa explosions (initially only Type II, followed by Type II plus Type Ia, and once the star formation activity has ceased only Type Ia) energize more and more gas particle heating them up to the escape velocity and beyond. Once escaped from the galaxy, particles reach distances proportional to their velocities. Contrary to what may appear, there is no acceleration on the gas particles after leaving the gravitational potential well of the galaxy. Interestingly, the average radial velocity is proportional to the distance, like in a Hubble-like flow; the ejection of the gas is therefore an explosive phenomenon, rather than a slow outflow. These remarks apply to all models. The mass of the ejected gas increases with time in all the models. The average velocity is proportional to the mass of the system, with massive galaxies generating winds at $\simeq 1500$ km/s, and low mass galaxies at about one tenth of this speed. However, looking more carefully it can be noticed that there are different linear velocities at the same radial distances, meaning that many explosive events have taken place. There is also a huge mass of gas moving outwards at lower speed, at late times (particularly in the HDHM model). The other model galaxies exhibit similar behaviour. Looking at the fractional amounts of escaping gas as a function of time—limited to the models HDHM, LDHM, HDLM, LDLM (the other models show similar behaviours) and once the system has virialized—the following trends are found. In the high mass realm, the fraction of gas *really* leaving the galaxy is only a few percent. On the contrary, in low mass systems more than half of the total gas has sufficient velocity to escape. Finally, the escaping gas is chemically enriched as shown by the right panel of Figure 13 (see [1], for all details) thus contributing to the chemical enrichment of the intra-cluster medium [190,191].

4.5. Mass Density Profiles

The geometrical structure of the model galaxies is best traced by the surface mass density profiles. To this aim, we choose the evolutionary stage at the redshift $z = 1$ and compare the surface mass density profiles of the model galaxies projected on the XY plane. These are plotted in the top three rows in Figure 14 together with [192] profile that best fits the model results,

$$\sigma_S(r) = \sigma_0 \times e^{(0.324-2m)\left[\left(\frac{r}{R_e}\right)^{1/m}-1\right]} \quad (4)$$

where R_e is the effective radius of the galaxy, as defined by [193], σ_0 the surface density at R_e, and m the *Sersic index* ($m = 4$ corresponds to the de Vaucouleurs profile). All profiles are computed starting at 0.2% of the virial radius of the galaxies to avoid the very central regions where softening may introduce spurious numerical effects. The best-fitting Sersic index is $m \sim 4$, $m \sim 1.5$, and $m \sim 2.5$, for high-, intermediate-, and low-mass models, respectively. In other words, high-(relative to low- and intermediate-) mass models tend to have higher m, in qualitative agreement with the existence of a luminosity-Sersic index relation for ETGs [194]. However, one should notice that the most massive ellipticals in the local Universe tend to have $m \sim 8$ (e.g., [195]), while we find $m \sim 4$. Moreover, the intermediate-mass models have somewhat lower m than the low-mass ones, which is only marginally consistent with luminosity-m relation, considering its large scatter.

Figure 13. (**a**) Galactic winds in the HDHM model. Red points: radial velocities of gaseous particles (km/s) against the distance from the barycenter of the systems (Mpc). Black circles: mean radial velocity in the spherical shell at radius r. Solid blue line: escape velocity as a function of the radius. Top to bottom: $z = 4.4$, 1, 0.2; (**b**) Projection on the [X,Y]-plane of the gas particles in the galactic winds. The color code is according to the metallicity of the gas particles. Nuclearly processed material can leave the galaxies thus enriching the surrounding medium. Reproduced with permission from [1]. Copyright 2012 John Wiley & Sons.

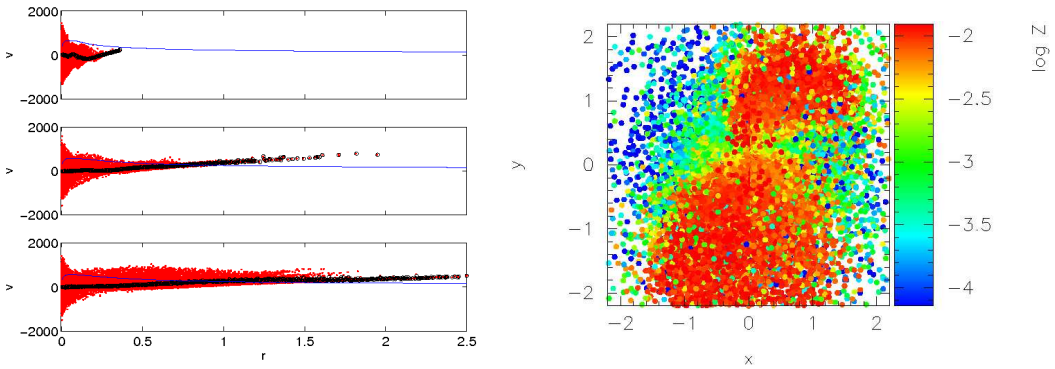

(**a**) (**b**)

4.6. Core or Cuspy Luminosity (Mass) Profiles?

The overall agreement between the models and the Sersic curves is good in the external regions. However, a clear departure from the expected fits is evident in all models at small radii (some fraction of R_e, indicated with the black diamond shown in each panel). In the central regions, the model galaxies tend to *flatten out* their mass density profile. Given the adaptiveness of the force softening, this feature can hardly be ascribed to numerical artifacts. Most likely, the high value of the dimensionless efficiency, $\epsilon_{sf} = 1$ we have adopted for the star formation rate, is the cause of it. This conclusion is strengthened by the three-dimensional mass density profiles compared with those by [193] and NFW [196], for stars

and DM, respectively that are shown in the bottom three rows of Figure 14. While the DM haloes smoothly follow the profiles of [196], the density of the stellar component never exceeds that of the DM, and contrary to the expectations [197], the central regions of the model galaxies are dominated by the DM, but perhaps the VLDHM case in which the two distribution are nearly equal. Amazingly enough, similar galaxy models by [23] with the same assumptions for the SFR but different in many other details (e.g., the initial conditions) yielded the opposite, *i.e.*, star dominated DM in the most central regions of the model galaxies. To single out the cause of disagreement is a cumbersome affair and perhaps of little interest here. Considering the whole problem in a wider context, first of all there is an obvious relationship between the efficiency of star formation and the gas density at which stars form. If star formation proceeds slowly (low values of ϵ_{sf}), the gas can reach high densities before being consumed by the star formation itself. The opposite if the star formation proceeds at high efficiency (high values of ϵ_{sf}). As a consequence of it, there is an immediate correlation between star formation and the dynamical behavior of a galaxy. If the star formation threshold is a loose one (e.g., $\epsilon_{sf} = 1$) extended stellar systems, with shallow potential wells and large effective radii are expected. On the contrary, a stringent star formation condition (e.g., $\epsilon_{sf} \simeq 0.1$ or lower) would let the cooling down gas to collapse to higher gas densities before getting the threshold condition for star formation, hence originate stellar systems of smaller dimensions and delay the time at which the bulk stars are formed. Interestingly, this constrains the modality in which gas collapses and forms stellar systems and shed light on the issue of core *versus* cuspy luminosity profiles in high and low mass ETGs, respectively. Historically, there are two possible and competing theoretical scenarios to describe the assembly of the stellar mass of an ETG (excluding the possibility of merger events). In the first one, stars originally form far away from the effective radius of the galaxy and subsequently accrete onto its inner regions, in a non-dissipative fashion. In the other case, first the gas flows into the central regions and then it is turned into stars. If the correct scenario is the first one, smoothing of the central density cusp of the profiles is expected, because the infalling stellar clumps loose orbital energy through dynamical friction and the halo heats up [198]. In the second case, the central distribution is expected to steepen up, because the gas radiates away its internal energy and an adiabatic contraction takes place [199]. Obviously, both processes are expected to play a role in reality. This is indeed what we note in the bottom three rows of Figure 14 the final density profiles gradually change from core-like to cuspy-like passing from HDHM to VLDLM ETGs. Our results clearly suggest that if stars are formed too early and easily, the resulting stellar systems are too shallow, ending up in "wrong" profiles: stars will tend to conserve their velocity dispersion as they fall into the potential wells and will therefore have elongated orbits. The opposite if stars are formed late and under more stringent conditions, and the gas is let to dissipate part of its kinetic energy and reach very high densities before turning into stars. All this is somehow supported and suggested by observational evidences for a deficit in the central luminosity of a few ETGs as recently found in observational data by ([200], their Figure 1, and references therein). The observed flattening begins at smaller radii (a fraction of R_e), and is present only in bright (*i.e.*, massive) systems. In contrast, low mass systems seem to present a luminosity excess. Recalling that the observational information stands on the luminosity profile, we can speculate that the trends of the observed curves should be fairly reproduced by translating the mass profiles into luminosity profiles. This is an interesting point, because the excess or deficit of light could be explained just in terms of stars and DM orbits, without the presence of a

super-massive black hole affecting the global dynamics in the center of the systems, as instead suggested in the studies quoted above.

Figure 14. (**a**) Projected surface density σ (g/cm^2) against the logarithm of radial distance $r(kpc)$ of the stars in the reference models at the last computed age. Blue dots: stellar particles radial averages; dashed line: Sersic best-fit (see text for details). The black diamonds indicate the effective radius R_e. The red squares show the smallest value reached by adaptive softening lengths, thus indicating the effective resolution of the simulations; (**b**) Mass densities of stars and DM ρ (g/cm^3) against the logarithm of the radial distance (kpc) for the reference models at $z \simeq 1$. Blue dots: the star particles; cyan dots: the DM particles; dashed lines: the Hernquist and NFW best-fits. In all rows from left to right: high, intermediate, low, and very low initial density. In each group of three rows from top to bottom: high, intermediate, and low mass galaxies. Reproduced with permission from [1]. Copyright 2012 John Wiley & Sons.

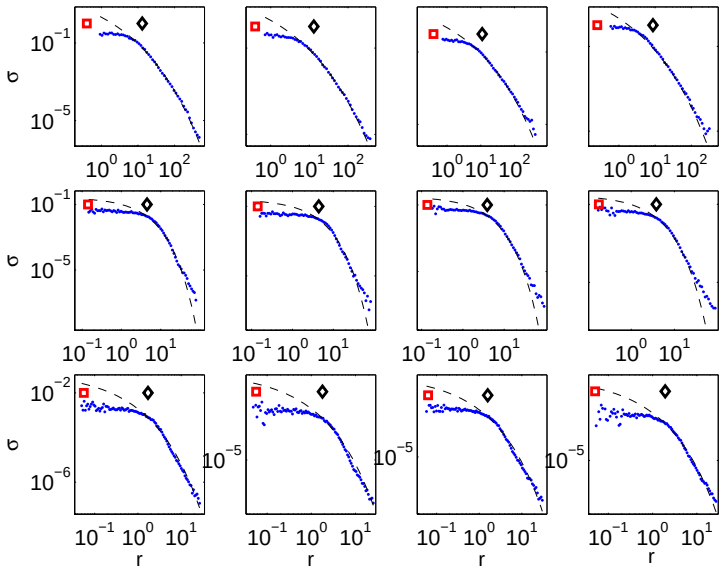

(**a**)

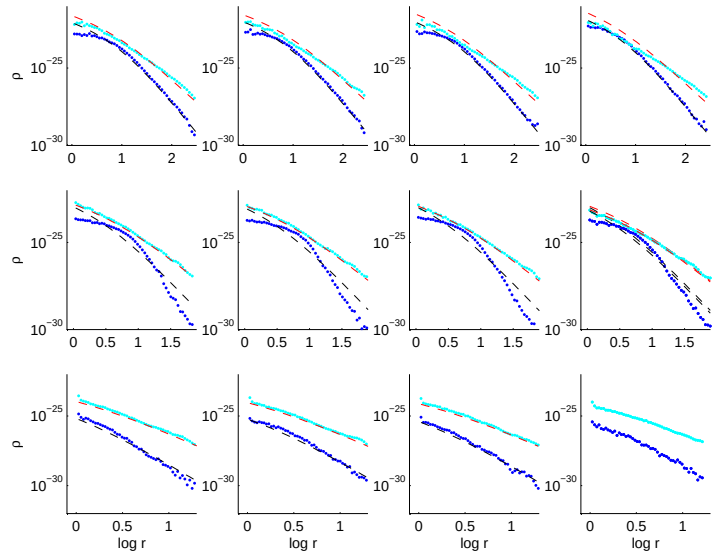

(**b**)

4.7. Open Issues in the Present Monolithic Model of Galaxy Formation

Stellar kinematics and rotation. Although the present galaxy models provide a generally satisfactory match of the observed Fundamental Scaling laws (e.g., the stellar mass radius relation and the Kormendy relation to be examined in Sections 5 and 6 below), the question whether they can also account for the kinematical anisotropy of massive ETGs and the increasing importance of rotational support at decreasing galaxy mass are still largely unexplored. Concerning the kinematical anisotropy we note that the mass resolution and the adaptive softening parameter are not good enough to follow in detail the kinematic of "star particles" and even worst of real stars. The only comment is that these monolithic-like models actually start from cosmological initial conditions in which lumps of DM and BM with different relative velocities and angular momentum collapse, merge together and form stars during the early stages of their history (by construction late major mergers of galaxy-shaped objects are not taken into account to preserve the monolithic-like nature of the whole process), so that a certain degree of anisotropy ought to be expected. On purpose, the present models are calculated with low spinning parameter to closely mimic real ETGs so they are not strictly applicable to disk galaxies of comparable mass with much higher rotation. Furthermore, our low mass objects are closer to dwarfs ellipticals or dwarf spheroidals (dEs and dSphs, respectively) rather than disk-like and irregular galaxies. On the other hand, the physical origin of dSphs and dEs and their star formation history are still highly uncertain [201–203].

The role of AGN. Following [92], the temporal (redshift) variation of the specific star formation rate SSFR and associated star formation time scale τ_{SF} can be interpreted as due to different energy feed-back mechanisms: only SNa explosions in the redshift interval $0 \leq z \leq 2$ and SNa + AGNs for $z \geq 2$. Alternatively it could be caused by much stronger inflow of gas at very early epochs triggering more intense star formation. An active galactic nucleus (AGN) is a compact region at the center of a galaxy that has a much higher than normal luminosity over at least some portion, and possibly all, of the electromagnetic spectrum. The radiation from AGN is believed to be a result of accretion of mass by a super-massive black hole (SMBH) at the center of its host galaxy, in the spheroid. There is a general consensus that SMBH mass tightly correlates with the spheroid mass [204] and the velocity dispersion [205]. The energy emitted by an AGN (even better the AGN energy feedback) is commonly advocated to explain or to cure several problems of galaxy formation and evolution: (i) AGN feedback is by far more efficient than SNa feedback in stopping cooling flows toward the center [206] and even ejecting the residual gas in form of hot galactic wind [207]. AGN feedback is also important during quiet stages of galaxy evolution via the so-called AGN radio mode that drive jets and cocoons, heat the halo gas, inhibit gas cooling, *etc.* (see [92], for more details and referencing); (ii) An immediate consequence of the AGN feedback is to quench star formation in massive galaxies [208–211] thus reproducing the sharp cut-off in the bright end of the galaxy luminosity function [212,213], and to level off the mass metallicity relationship of most massive galaxies [214]. The origin of SMBHs, however, remains an open field of research. Once a BH is in place at the center of a galaxy it can grow by accretion of matter (stars, gas, *etc.*) and by merging with other BHs. There are several hypotheses for the formation mechanisms and initial masses of the SMBHs progenitors (seeds). The most obvious hypothesis is that the seeds are BHs with masses in the range 5 to 30 $M_{\odot}$ that are left

behind by the classical core collapse SNa explosions of massive and very massive stars above about 50 $M_{\odot}$. See [215] for an exhaustive review of the whole subject of SNa and formation of stellar BHs. These BHs later grow by accretion of matter. Another model is by [216] who suggest that a massive gas cloud, loosing angular momentum by global dynamical instabilities, leads to the rapid buildup of a dense, self-gravitating core supported by gas pressure and surrounded by a radiation pressure dominated envelope which gradually contracts and is compressed further by subsequent infall of matter. Thanks to this, the central temperature increases to such high values that thermal neutrino emission is reached soon inducing catastrophical cooling down of the core and the formation of a rapidly growing central BH. The expected BH mass is about $20\,M_{\odot}$, but by rapidly accreting mass it should become first an intermediate-mass black hole (IMBH), and possibly a SMBH if the accretion-rate is not quenched by the AGN activity itself. Another possibility [217] involves a dense stellar cluster undergoing core-collapse as the negative heat capacity of the system drives the velocity dispersion in the core to relativistic speeds. Finally, primordial BHs may have been produced directly from external pressure soon after the Big Bang. Formation of BHs from the deaths of the first stars has been extensively studied and corroborated by observations [218]. The difficulty in forming a SMBH resides in the need for enough matter with very little angular momentum and confined within a small enough volume. Normally, the process of accretion involves transporting a large initial endowment of angular momentum outwards, and this appears to be the limiting factor in black hole growth. The majority of the mass growth of SMBHs is thought to occur through episodes of rapid gas accretion, which are observable as AGNs or quasars that are more frequent in the very early Universe. Therefore SMBHs arose very early in the Universe, inside the first massive galaxies. Currently, there appears to be a gap in the observed mass distribution of BHs. There are stellar-mass black holes, generated from collapsing stars, which range from about 5 to 30 $M_{\odot}$. The minimal SMBHs are in the range of about $10^5 M_{\odot}$. Between these regimes there appears to be a dearth of IMBHs thus suggesting that perhaps two different mechanisms are at work. Such a gap would suggest qualitatively different formation processes. Reference [219] suggest that ultra-luminous X-ray sources (ULXs) may be BHs from this missing group.

The main conclusion we draw here is that AGNs may be an important physical ingredient of galaxy models, however without being an unavoidable requisite of the galaxy formation process, in the sense that "only hierarchical models of galaxies with AGNs can reproduce the observational data". Indeed also the present models with no SMBH and no AGN quench their star formation after the initial peak of activity (at least in the case of massive high initial density galaxies), level off their mass-metallicity relationships, and produce copious galactic winds in addition to other important properties. The inclusion of a BH and AGN feedback in turn would certainly improve the whole picture but without drastically change what has already been reached without them. Finally, as far as we can see, the monolithic-like scenario of galaxy formation should reproduce the relationship SMBH mass *versus* spheroidal mass and velocity dispersion.

Intermediate-age stellar populations in ETGs. The presence of intermediate age stellar populations in ETGs has been reported by a number of observational or semi-empirical studies examining the total colors of galaxies (see for instance [130,220]), and the line absorption diagnostic planes (see for instance [13,14,40,57,65,74,80–82], and references). The general conclusion was that if intermediate age stellar population are present they should amount to only a few per cent (from 1% to 5%) otherwise

they would alter the global properties of the hosting galaxies. There should be a sort of "star formation frosting" according to [13,14]. Looking at the rate of star formation of Figure 10, the mass assembly history of Figure 11, and the radial distance from the galaxy center of Figure 12, in high and intermediate mass and density models (the mass and density intervals of typical ETGs), the percentage of stars born after the first 5 Gyr lifetime of the host galaxies goes from virtually zero to a few percent as the initial density decreases. The situation is different for the low mass models in which at least 50% of the stars formed during the time interval going from the very recent past to about 5 Gyr ago, see for instance the simulations of the stellar content in dwarf elliptical galaxies made by [201].

Systems of Globular Clusters in ETGs. In most large galaxies, the system of GCs (i) show a bimodal color and metallicity distributions; (ii) the metal-rich (red) and metal-poor (blue) clusters have systematically different locations and kinematics in their host galaxies; (iii) however, the red and blue clusters have similar internal properties, such as their masses, sizes, and ages [221,222]. Assuming the hierarchical scenario as the paradigm of galaxy formation, [221,222] examine whether both metal-rich and metal-poor clusters could form by this mechanism and still be consistent with the bimodal distribution. If all GCs form only during mergers of massive, gas-rich proto-galactic disks, their metallicity distribution could be statistically consistent with that of the GCs. In their best-fitting model, early mergers of smaller hosts create exclusively blue clusters, while subsequent mergers of progenitor galaxies with a range of masses create both red and blue clusters. Thus, bimodality arises naturally as the result of a small number of late, massive merger events. They also argue that, due to dynamical interactions, more blue than red clusters are disrupted by the present time because of their lower initial masses and older ages. The present-day mass function of the model clusters is consistent with the Galactic one whereas their spatial distribution is much more extended than observed. However, if the whole system of GCs span a narrow range of ages, how does it agree with the view that "late mergers" should form the red clusters according to the hierarchical scenario? Possible explanation is that the samples of GCs of the two merging galaxies were formed very early on so that their age is similar but out of material with different metal content. So at the late merger there is no formation of new clusters but only the aggregation of two sub-groups. Alternatively all the clusters are formed very early on in the same galaxy out of lumps of BM with different metallicity due to previous enrichment and no late mergers are required. In any case, internal and external mergers can easily explain the different location and kinematics of blue and red GCs.

4.8. The Hybrid View: Early Hierarchical Quasi Monolithic

The main lesson we learn from these numerical simulations of formation and evolution of galaxies is that starting from cosmological initial conditions for the perturbations one sees the aggregation of lumps of DM and BM in the common potential well and the growth of all this to the size of a real galaxy on a short time scale while star formation occurs and the stellar content of a galaxy is built up. By redshift $z = 2$ a great deal of the action is completed, even massive objects can be in place. Hierarchical aggregation has taken place within a rather short time scale, about 1–2 tenths of the Hubble time. If let to evolve on its own, the resulting object will show at the present time a pattern of properties very similar to those of real galaxies. This is the main reason for naming the whole process "*early hierarchical*

quasi monolithic galaxy formation". What happens to this object if in the course of its life it undergoes later mergers with similar objects? "*The outcome depends on the relative mass of the merging galaxies and the mode of star formation*". Major mergers will greatly affect the dynamics, morphology, stellar content, and the integral spectral energy distribution of this galaxy. Minor mergers will do the opposite. The details on the outcome are not of interest here. Since there is observational evidence of major and minor mergers, their occurrence cannot be excluded. What we may say is that mergers are not the only way to assembly massive galaxies, ETGs in particular. Most likely both concur to the overall formation and evolution process of galaxies.

There is another important consideration to make, *i.e.*, the difference between the above approach and what is commonly made in classical SAMs. Quoting [92] "in SAMs, galaxies are painted on haloes built from halo merger trees or detected in cosmological dissipation-less (DM only) simulations". In other words, BM is added later to haloes, the mass assembly of which has been derived without BM. "Painting BM" is not the same as taking both DM and BM together from the very beginning. Indeed the dissipative collapse of BM and occurrence of star formation in the potential well of DM will certainly affect the dynamical behavior and hence mass assembly history of the latter. Maybe this is the simple explanation for the occurrence in Nature of early hierarchical quasi monolithic galaxy formation.

5. The Mass-Radius Relationship of ETGs

In recent years, much attention has been paid to the MRR of galaxies, in particular the ETGs and the compact and passive ones at high z. The MRR is indeed basic to any theory of galaxy formation and evolution. The subject of the MRR of galaxies from ETGs to dwarf ellipticals and dwarf spheroidals, including also bulges and Globular Clusters, has been recently reviewed by [84,85] to whom we refer for many details. In addition to this, convincing evidence has been gathered that at relatively high redshifts, objects of mass comparable to that of nearby massive galaxies but smaller dimensions exist. These "compact galaxies" are found up to $z \geq 3$ with stellar masses from 10^{10} to $10^{12}\,M_{\odot}$ and half-light radii from 0.4 to 5 kpc (*i.e.*, 3 to 4 times more compact than the local counterparts of the same mass), and in nearly similar proportions there are galaxies with the same mass but a variety of dimensions (e.g., [223,224]), and bulge to disk ratios (e.g., [225]). However, we will consider here only the case of standard ETGs, leaving the compact galaxies aside.

The key question to answer is: Why do ETGs obey a rather narrow MRR instead of scattering around and showing a broader combination of masses and sizes? Spurred by this, [226] look for the general physical principles governing this important scale relation. To clarify the aims and the methods of this study, we summarize here the essence of the analysis made by [226]. It is suggested that the observed MRR for ETGs is the result of two complementary mechanisms. On one hand, the mass function of DM haloes hosting the visible galaxies gives (i) the typical cut-off mass at which, at any redshift, haloes become "common" on a chosen spatial scale; and (ii) the typical epoch at which low mass haloes begin to vanish at a rate higher than that at which they are born, because of merger events. On the other hand, these constraints define two loci (curves) on the MR-plane, because to each mass and formation redshift a typical dimension (*i.e.*, radius) can be associated (using a basic relation between mass and radius of a collapsing object). If the typical dimension of a galaxy is somehow related to that of the hosting DM

halo (as our NB-TSPH models seem to suggest), then the region of the MR-plane between the two limits fixed by the halo mass function is populated by galaxies whose dimensions are fixed at the epoch of formation, and only those objects that are “possible" at any given epoch may exist, populating a narrow region of the MR-plane.

The MRR of normal ETGs. The observational data we are considering is the HB sample selected by [227] from the SDSS catalog, containing $\simeq 60,000$ galaxies. The catalog contains the stellar mass M_s in $M_\odot$ and the radius $R_{1/2}$ (in kpc) enclosing half of it. It is worth to clarify here that $R_{1/2}$ is nearly identical to the classical R_e. The linear fit of M_s and $R_{1/2}$ yields:

$$\log R_{1/2} = 0.54 \ \log M_s - 5.25 \tag{5}$$

The slope and zero point of the above MRR are quite robust and coincide with previous determinations [23,84,85,89,228]. It is worth noting that toward the high mass end the slope of the MRR tends to increase to about 1, see [227], [229], [230], and Figure 1 of [84]. This is a point to keep in mind when interpreting the observational data.

Galaxy counts in the MR-plane. Before proceeding further, it is worth looking at the number frequency distribution of galaxies with given mass and radius in the above SDSS sample. To this aim, the MR-plane is divided in a grid of square cells with dimensions of 0.05 in units of $\Delta \log M_s/(10^{12}\, M_\odot)$ and $\Delta \log R_{1/2}$, and the galaxies falling in each cell are counted. In the left panel of Figure 15 we display the 3D space of these parameters to simultaneously highlight the distributions of the MRR along the direction parallel to the best-fit line on the MR-plane and the direction perpendicular to it. The view angle is chosen in such a way that the projections on the planes parallel and perpendicular to the MRR line can be easily figured out. While the projection on the plane parallel to direction of the best-fit line can be easily understood in terms of selection effects (galaxy mass fall-off at the high mass end and lack of data at the low mass end), the distribution perpendicular to this is more difficult to explain. Indeed *galaxies tend to fall in a rather narrow strip of the MR-plane, tightly gathering around the line with slope 0.54*.

Adding dwarf galaxies. In addition to this we consider a small sample of dwarf galaxies of the Local Group to compare their location on the MR-plane with that of normal ETGs. The data for dwarf galaxies are from [89,231]. Dwarf galaxies are much more dispersed in the MR-plane and their mean MRR is $logR_{1/2} = 0.3 logM_s - 2.7$, which is much flatter than that of the normal ETGs.

Comparing models with data. The present day positions on the MR-plane of the reference models of Table 1 and a few auxiliary models calculated for this purpose (see [226], for all details) are shown in the right panel of Figure 15 together with the observational data. For the ancillary models suffice it to mention here that they are calculated for the intermediate and low mass galaxies at varying either the collapse over-density or the star formation efficiency ϵ_{sf}. Focusing on the reference models it is soon evident that only those of high (HM) and intermediate mass (IM) are consistent with the data. The low mass ones (LM) are too far off. It is worth recalling that these models have quite similar initial densities and initial redshifts. The slope of the theoretical MRR does not agree with the data. What does all this mean? To understand the issue one must clarify the correlation between initial over-density and present day position of the models, *i.e.*, the correlation between the halo density, the SFH, and the present position on the MR-plane.

Figure 15. (**a**) 3D view of the MRR. The number frequency distribution of galaxies on the MR-plane: M_s is the total stellar mass in solar units and $R_{1/2}$ is the half-mass radius in kpc, and "Counts" is the number of galaxies falling within each cell of the plane with dimensions $\Delta \log M_{12}$ = 0.05 and $\Delta \log R_{1/2}$ = 0.05. The data are from the HB sample of [227]. The thick line on the MR-plane is the linear fit of the data: $\log R_{1/2} = 0.54 \log M_s - 5.25$; (**b**) Theoretical MRR, *i.e.*, $\log R_{1/2}$ *versus* $\log M_s$. The filled squares are the reference models of Table 1 and the filled circles the ancillary models. The color code recalls the initial over-densities. However, as the entries of Table 1 are fully sufficient to identify the models, the correspondence color-code-initial density is superfluous here. The thick black line is the fit of the reference models. The thin straight lines are the theoretical MRR on which proto-galaxies of given DM over-density settle down at the collapse stage as a function of the redshift. The lines are given by Equation (6) from [232]: solid lines are for $m = 10$ and $f_\sigma = 1$; the color code indicates different redshifts (black: $z = 0$; blue: $z = 1$; red: $z = 2.5$; green: $z = 5$; cyan: $z = 20$); the thin black dashed line is for $m = 10$, $f_\sigma = 1.5$, and $z = 0$; Finally, the thin black dashed-dotted line is for $m = 5$ and $f_\sigma = 1$, and $z = 0$. Adapted from [226].

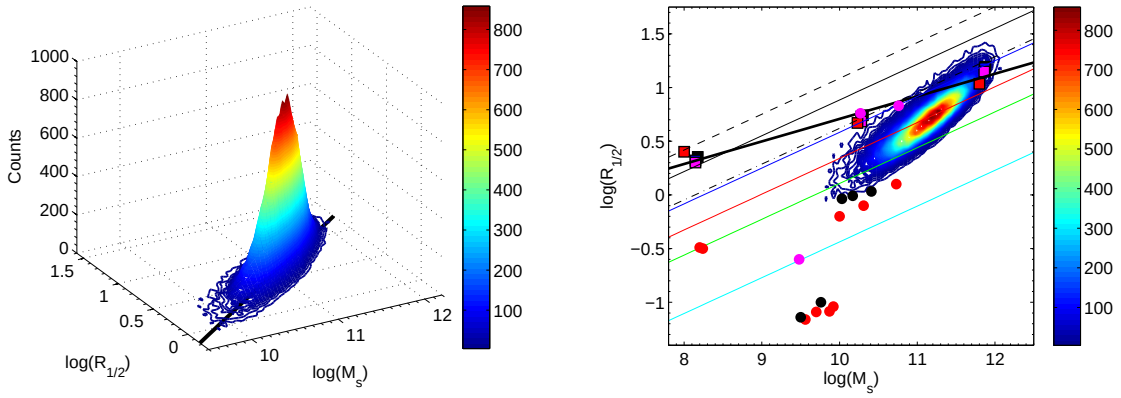

(**a**) (**b**)

5.1. The Filiation Thread

Starting from the stage of proto-halo collapse, Equation (5) yields the initial MRR for the proto-haloes, whose slope is $R_h \propto M_h^{1/3}$ by construction. Inside these haloes the BM, initially in form of gas, is gradually turned into stars, so that a new MRR is built up for the stellar content. In our case the one predicted by the NB-TSPH models.

The NB-TSPH reference and ancillary models allow us to clarify the different role played by the initial cosmological density contrast $\delta\rho_i(z)$ and the gas density $\rho_{g,sf}$ at the onset of star formation in determining the size of the resulting galaxy made of stars and the relation between the initial gas mass and the final star mass. Further, the nature of the global process converting gas into stars.

Given the total mass oh the proto-halo M_h (it is worth recalling that $M_h \simeq M_{DM}$ so that they can be interchanged), the cosmological density $\delta\rho_i(z)$ determines the initial radial dimension of the DM perturbation. This does not coincide with the initial radius at which star formation begins in the baryonic

component of a galaxy. In other words, within the potential well of DM, the gas keeps cooling at increasing density and only when the threshold density for star formation is met (which in turn is related to ϵ_{sf}), stars appear: the galaxy is detectable on the MR-plane. In the latter step of the filiation thread, $\rho_{g,sf}$ plays the dominant role. The remaining gas continues to fall into the gravitational potential well until either it is exhausted by SF or it is expelled via shocks because of the energy feed back. Thanks to this there will be a correlation between the DM and the final mass in stars, measured by $m = M_{DM}/M_s$ (with $m \sim 10$ on the average).

NB-TSPH models [1] indicate that the transformation of BM into stars occurs under the homology condition $GM_{DM}/R_{DM} \simeq GM_s/R_{1/2}$, *i.e.*, equal gravitational potential energy per unit mass of the two components. In general, the model galaxies follow this rule and the two components of a galaxy lie on nearly parallel MRRs: *i.e.*, $R_h \propto M_h^{1/3}$ and $R_{1/2} \propto M_s^{1/\beta}$ with $\beta \simeq 3$. At decreasing total mass, the exponent $1/\beta$ goes from 0.333 for galaxies with total mass $10^{13}\,M_\odot$ to about 0.2 for a mass of $10^9\,M_\odot$ or even lower. This deviation from the $R_{1/2} \propto M_s^{1/3}$ law can be interpreted as due to an increasing departure from the condition of an ideal collapse because dissipative processes are now at work. The higher the initial mass, the closer the evolution of the proto-galaxy is to the simple collapse models. In other words, the straight collapse configuration corresponds to a minimum total energy of the system, whereas in all other cases the total energy system is far from the minimum level. Recasting the concept in a different way, the straight collapse is favored with respect to other energy costing configurations. Real galaxies tend to follow the rule by as much as they can compatibly with their physical conditions (total mass, initial density, SFH, ...). The result of it will be that the final model galaxies will be located on a new line (not necessarily a straight line but likely close to it) with a certain slope (about 0.2 in our case, see the linear fit of the final mean location of the reference models). The slope is flatter than the 0.33 slope of the iso-density line of the initial DM proto-galaxies. There is not reason for the two slopes being the same.

An analytical relationship. In the context of the Λ-CDM cosmology, reference [232] have adapted the general Equation (5) to provide an expression correlating the halo mass M_{DM} and the star mass M_s of the galaxy born inside it, the half light (mass) radius $R_{1/2}$ of the stellar component, the redshift at which the collapse takes place z_f, the shape of the BM galaxy via a coefficient $S_S(n_S)$ related to the Sersic brightness profile from which the half-light radius is inferred and the Sersic index n_S, the velocity dispersion of the BM component with respect to that of DM (expressed by the parameter f_σ), and finally the ratio $m = M_{DM}/M_S$. The expression is:

$$R_{1/2} = 0.9 \frac{S_S(n)}{0.34} \frac{25}{m} \left(\frac{1.5}{f_\sigma}\right)^2 \times \left(\frac{M_{DM}}{10^{12} M_\odot}\right)^{1/3} \frac{4}{(1+z_f)} \tag{6}$$

Typical value for the coefficient $S_S(n_S)$ is 0.34. For the ratio $m = M_{DM}/M_s$ the empirical data confine it in the range 20 to 40, whereas our NB-TSP models yield $m \simeq 15$ to 20 depending on the particular case we refer to. For the purposes of the present study we take the rather low value $m = 10$. Finally f_σ yields the three dimensional star velocity dispersion as a function of the DM velocity dispersion, $\sigma_s = f_\sigma \sigma_{DM}$. Here we adopt $f_\sigma = 1$. For more details see [232] and references therein and [226]. The slope of Equation (6) is of course steeper but close to that of NB-TSH models; the difference can be fully ascribed to the complex baryon physics, which causes the stellar system to be slightly offset with respect to the locus analytically predicted from DM haloes. Therefore, a model slope different from that

of the observational MRR (but still close to 0.3) is not the result of inaccurate description of the physical processes taking place in a galaxy. It is indeed remarkable that complicated numerical calculations clearly display this fundamental feature. *If this is the case, why do real galaxies gather along a line with a different slope?*

5.2. The Cosmic Galaxy Shepherd

To answer the above question, reference [226] attack the problem from a different perspective, trying to investigate whether the observational MRR owes its origin to deeper reasons, likely related to the growth function of DM haloes [122]. Given a certain number density of haloes N_h, on the $n(M_{DM}, z)-z$ plane of Figure 16 (left panel) this would correspond to a horizontal line intersecting the curves for the various masses at different redshifts. Each intersection provides a pair (M_{DM}, z) which gives the mass of the haloes fulfilling the constraint N_s at the corresponding redshift z. For any value N_h we get an array of pairs (M_{DM}, z) and with the aid of the [232] relationship (where the parameters m and f_σ are fixed) we can translate it into a relationship between the mass in stars and the half-mass radius of the baryonic galaxy associated to a generic host halo to be plotted on the MR-plane.

Figure 16. (**a**) The growth function of haloes $n(M_{DM}, z)$, reproduced with permission from [122]. Copyright 2007 IOP Publishing. (**b**) The *cosmic galaxy shepherd* (CGS) and the corresponding locus of DM parent haloes (the red thick and thin solid lines, respectively) on the MR-plane. The halo number density is $N_h = 10^{-2}$ haloes per (Mpc/h)^3. For comparison, we also show the case for $N_h = 10^{-8}$ haloes per (Mpc/h)^3 (the magenta thick and thin dashed lines). The observational data is the HB sample of [227] with their linear fit (solid black line), and two theoretical MRR from Equation (6) by [232] (solid thin blue lines), relative to $z = 0$ and $z = 10$, with $m = 10$ and $f_\sigma = 1$ together with the reference galaxy models and their linear fit (filled squares and black solid line). Adapted from [226].

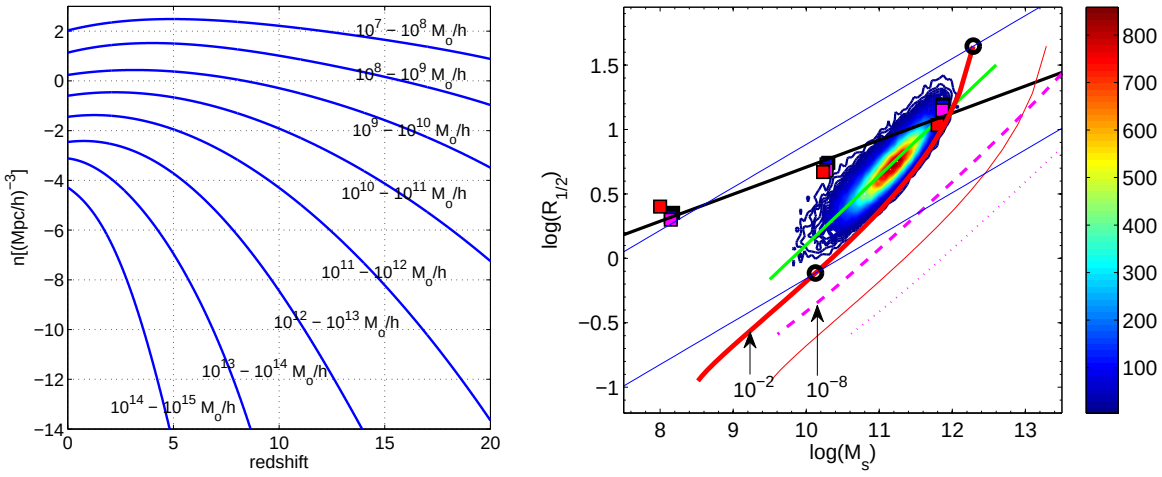

(**a**) (**b**)

Repeating the procedure for other values of N_h, one gets a manifold of curves on the MR-plane. It turns out that with $N_h = 10^{-2}$ haloes per (Mpc/h)^3, the curve is just at the edge of the observed

distribution. Higher values of the N_h would shift it to larger haloes (baryonic galaxies), the opposite for lower values of N_h. Why is $N_h = 10^{-2}$ haloes per (Mpc/h)^3 so special? Basing on crude, simple-minded arguments, we recall that the total number of galaxies observed by the SDSS amounts to about $\simeq 10^6$, whereas the volume of Universe covered by it is about $\simeq 1/4$ of the whole sky times a depth of $\simeq 1.5 \times 10^9$ light years, *i.e.*, $\simeq 10^8$ Mpc^3, to which the number density of about 10^{-2} haloes per (Mpc/h)^3 would correspond (We are well aware that this is a very crude estimate not taking into account many selection effects both in the observations and the halo statistics based on NB simulations, such as the [122] plane itself. However, just for the sake of argument, we can consider it as a good estimate to start with). All this is shown in Figure 16 (right panel), where we also plot the curves relative to another possible choice $N_h = 10^{-8}$ haloes per (Mpc/h)^3, corresponding to 1 halo per 10^8 (Mpc/h)^3, for the sake of comparison. It is an easy matter to see that the mean slope of the relation holding for $N_h = 10^{-2}$ haloes per (Mpc/h)^3 continuously varies from 0.5 to 1 and above as we move from the low mass to the high mass range. A similar trend for the slope is indeed also indicated by the observational data (see [230], and references therein). Owing to the many uncertainties we do not try to formally fit the median of the empirical MRR, but we limit ourselves to show that the locus predicted by the $N_h = 10^{-2}$ haloes per (Mpc/h)^3 falls on the MR-plane close to the observational MRR. Lower or higher values of N_h would predict loci in the MR-plane too far from the observational MRR unless other parameters of Equation (6), e.g., m, are drastically changed assuming values that are difficult to justify. Finally, we call attention on the fact that the locus on the MR-plane defined by the solid curved line on the right panel of Figure 16 is ultimately related to the top end of the mass scale of haloes (and their filiated baryonic objects) that can exist at each redshift. In other words, it can be interpreted as the so-called cut-off mass of the galaxy mass distribution (see [122], for details and references). This locus is named the *Cosmic Galaxy Shepherd* (hereafter CGS).

There are two points to clarify. First, we have implicitly assumed that *each halo hosts one and only one galaxy and that this galaxy is an early type object matching the selection criteria of the [227] sample*. In reality ETGs are often seen in clusters and/or groups of galaxies and many large spirals are present. Only a fraction of the total population are ETGs. One could try to correct for this issue by introducing some empirical statistics about the percentage of ETGs among all types of galaxy. Despite these considerations, to keep the problem simple we ignore all this and stand on the minimal assumption that each DM halo hosts at least one baryonic component made of stars. This is a strong assumption, on which we will come back again later on. Second, we have adopted $m = 10$ and $f_\sigma = 1$. According to [232], the empirical estimate of M_{DM}/M_s ratio is about 20–40, *i.e.*, a factor of two to four less efficient star formation than that we have assumed basing on our NB-TSPH models. However, a smaller value for m does not invalidate our analysis, because it would simply shift the location of the baryonic component on the MR-plane corresponding to a given halo number density. Finally, $f_\sigma = 1$ is a conservative choice. The same considerations made for m apply also to this parameter. At present, there is no need for other values. Along the CGS, redshift and cut-off mass go in inverse order, *i.e.*, low masses (and hence small radii) at high redshift and vice versa. This means that a manifold of MRRs defined by Equation (6), each of which referring to a different collapse redshift, can be selected, and along each MRR only masses (both parent M_{DM} and daughter M_s) smaller than the top end are permitted, however each of which with a different occurrence probability: low mass haloes are always more common than

the high mass ones. In the observational data, it looks as if ETGs should occur only towards the high mass end of each MRR, *i.e.*, along the locus on the MR-plane whose right hand side is limited by the CGS. This could be the result of selection effects, *i.e.*, (i) galaxies appear as ETGs only in a certain interval of mass and dimension and outside this interval they appear as objects of different type (spirals, irregulars, dwarfs *etc.*); or (ii) they cannot even form or be detected (e.g., very extended objects of moderate/low mass). Finally, in addition to this, we argue that another physical reason limits the domain of galaxy occurrence also on the side of the low mass, small dimension objects.

Dissipation-less Collapse. It is an easy matter to figure out that the CGS is another way of rephrasing the top-hat spherical dissipation-less collapse for primordial fluctuations by [233] for which $R_{DM} \propto M_{DM}^{\frac{5+n}{6}}$ where n is the slope of the density fluctuation δ. Adopting $n = -1.8$, the power spectrum of CDM according to [234], we get the slope $d \log R_{DM}/d \log M_{DM} \simeq 0.53$ (see also [89]). The slope of the MRR derived from the dissipation-less collapse is the same of Equation (5) all over the mass range from normal/giant galaxies down to classical Globular Clusters ([23,84,85], for more details). The advantage of the CGS is that it provides slope and zero point of the observational MRR and also predicts its change in slope at increasing star mass of the galaxy.

Given these premises, we suggest that the observational MRR represents the locus on the MR-plane of galaxies whose formation and evolution closely followed the scheme of dissipation-less collapse, *i.e.*, the ones with mass close to the cut-off mass at each redshift.

5.3. Simulating the MRR

To sustain the above suggestion [226] try to simulate the observational MRR using the growth function calculated by [122] according to which the total number of the haloes that would nowadays populate the synthetic MR-plane and that should be compared with the observed galaxies are contained in the mass-bin $\Delta log M_{DM}$ at redshift z = 0. Prior to any other consideration one has to scale the theoretical predictions [122] that refer to a volume of space of 1 (Mpc/h)^3, by a suitable factor N_{norm} to match the real volume covered by the data. Our sample contains about 60,000 galaxies, 6% of the total survey over a total volume of 10^8 Mpc^3, therefore $N_{norm} = 5 \times 10^6$. To each mass M_{DM} expected at z = 0 we must associate a redshift of formation in order to be able to estimate the corresponding baryonic galaxy (M_s, $R_{1/2}$), by means of the [232] relationship (of course assuming $m = M_{DM}/M_s$ and $f = \sigma s/\sigma_{DM}$).

The growth functions of [122] allow one to derive the number of $N(M_{DM}, z)$ of haloes existing in each mass bin $\Delta \log M_{DM}$ at any redshift z. This number is the result of two competing effects: the formation of new haloes of mass M_{DM} via merger and/or acquisition of lower mass haloes, and the destruction of haloes of mass M_{DM} as they merge to form higher mass haloes. Therefore:

$$n(M_{DM}, z) = n(M_{DM}, z + \Delta z) + n_+(M_{DM}, z) - n_-(M_{DM}, z + \Delta z) \quad (7)$$

where n_+ and n_- represent the creation/destruction mechanisms. In particular, the quantity we are interested in is $n_+(M_{DM}, z)$, which is the number of new haloes of mass M_{DM} which are born at redshift z. The number of haloes that merge to form higher mass systems is in turn a fraction of the number of haloes existing at that time, *i.e.*, $n_-(M_{DM}, z + \Delta z) = \eta \times n(M_{DM}, z + \Delta z)$, with $0 < \eta < 1$; so:

$$n_+(M_{DM}, z) = n(M_{DM}, z) - (1 - \eta) \times n(M_{DM}, z + \Delta z) \quad (8)$$

The only free parameter here is η, the fraction of haloes that merge to form higher mass systems in the redshift interval Δz. In principle, the fraction η could vary with the redshift. However, for the sake of simplicity we assume that η remains constant. Thus, we obtain a value $N_+(M_{DM}, z)$ for each interval $M_{DM}, M_{DM} + \Delta M_{DM}$ and $z, z + \Delta z$. This number, re-normalized to unit over the whole interval, can be considered as the relative probability that a halo of mass M_{DM} is born at redshift z. Finally, for each halo of mass M_{DM} we compare a randomly chosen number $q \in [0, 1]$ with the cumulative probability:

$$P_{z_i} = \sum_{z=z_{max}}^{z=z_i} n_+(M_{DM}, z)$$

until $q < P_{z_i}$, and take $z_f = z_i$ as its formation redshift. Using Equation (6) we get the radius of the baryonic galaxy filiated by this halo to be plotted on the MR-plane. The distribution of galaxies on the MR-plane depends on the fraction η of haloes which merge to form higher mass systems in the redshift interval Δz. Only values of η smaller than about 0.02 lead to acceptable results. In the following we adopt $\eta = 0.01$. The predictions for $\Delta n(z) = n(z + \Delta z) - n(z)$ are shown in the left panel of Figure 17. The agreement is remarkable. In order to take into account that the observational sample contains a finite number of galaxies so that some cells of the theoretical MR-plane may not be populated in reality due to stochastic effects, we present Montecarlo simulations of the MR-plane using the [122] growth functions as probabilities. The resulting MRR is shown in the right panel of Figure 17. We also look at the redshift (age) distribution of galaxies in the MRR: the vast majority of galaxies have been formed before redshift z = 1. Finally, no correction is applied to the top end of the MRR to account for the fact that several galaxies per halo could be found at this mass range (above say $M_s > 10^{12} M_\odot$). This would remove nearly all the objects falling on the MRR at the high mass end, *i.e.*, say above $10^{12}\ M_\odot$.

5.4. How Many Mergers?

Assuming for simplicity that η is constant with time, one may calculate the ratio between the total number of merger events, $N_{merg} = \sum_{z_{bin}} \eta \times n(M_{DM}, z)$ and the total number of galaxies that ever existed during the Hubble time, $N_{tot} = \sum_{z_{bin}} n_+(M_{DM}, z)$:

$$\frac{N_{merg}}{N_{tot}} = \frac{\sum_{z_{bin}} \eta \times n(M_{DM}, z)}{\sum_{z_{bin}} n_+(M_{DM}, z)} \tag{9}$$

Crude calculations yield $N_{merg}/N_{tot} \simeq 0.10 - 0.15$ for $\eta = 0.01$. This percentage increases to about 50% for $\eta = 0.05$. With the latter value, the MRR is much more dispersed than the observational one. Therefore, it seems that only a fraction (from 0.1 to 0.5) of haloes should have merged during the whole history of the Universe. Owing to the many uncertainties still affecting the above discussion, one cannot insist on this issue.

6. Spectro-Photometry of NB-TSPH Model Galaxies

One of the major challenges in modern astrophysics is to understand the origin and the evolution of galaxies, the bright, massive ETGs in particular. There is strong observational evidence that massive ETGs are already in place at redshift $z \sim$ 2–3 and that formed most of their stars well before

$z = 1$. Therefore, these galaxies are good probes of galaxy evolution, star formation and metal enrichment in the early Universe. In this context, the spectro-photometric population synthesis applied to chemo-dynamical NB-TSPH model galaxies provides excellent diagnostics of ETGs evolution during the cosmic history from the early epoch to the present day Universe.

Figure 17. (**a**) Comparison of the theoretical (red dots, negative Z-axis) with the observational (blue dots, positive Z-axis) number frequency distributions of galaxies on the MR-plane: $\log M_S$ *vs.* $\log(R_{1/2})$ (in $M_\odot$ and kpc, respectively), "Counts" stands for $\Delta n(z) = n(z+\Delta z) - n(z)$, *i.e.*, the number of haloes per Mpc^3 born between z and $z+\Delta z$. The thick line is the best fit of the observational data [HB sample of 227]. The theoretical number frequencies have been plotted as negative quantities to get the mirror image of the observational data; (**b**) Monte-Carlo simulation of the MRR: comparison of the theoretical (black dots) with the observational (red dots) distributions of galaxies on the MR-plane. The theoretical simulation is for $\eta = 0.01$. Superposed to it are the reference models (filled squares) for intermediate and high mass galaxies and their linear fit, and the CGS for $N_h = 10^{-2}$ haloes per $(Mpc/h)^3$ (the thick dashed green line is for the stellar component and the blue line for the DM halo). The thin trasverse lines are the [232] relationships for different redshift, namely z = 0, 5, 10, and 20 from the top to the bottom. Finally, the observational data are from [227]. Adapted from [226].

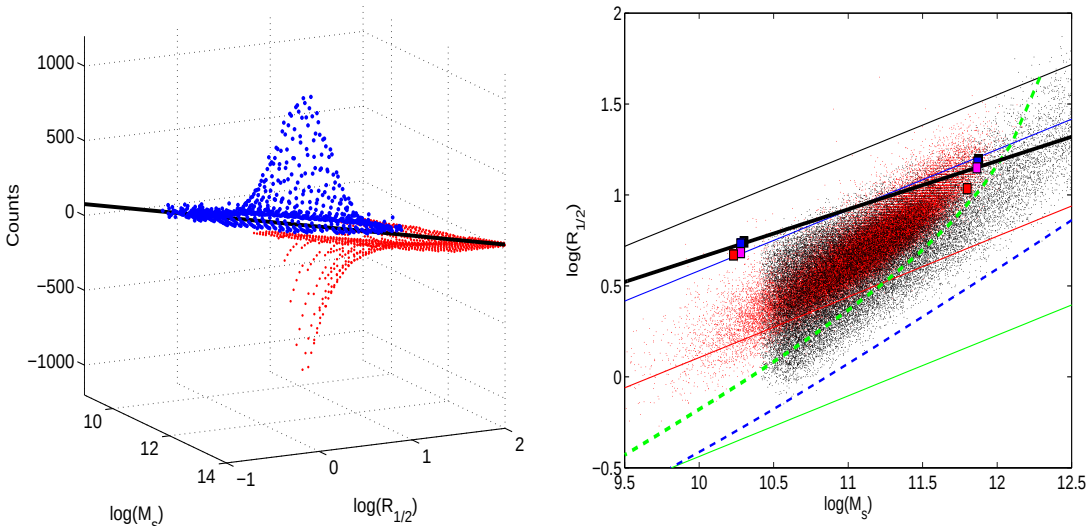

(**a**) (**b**)

Elements of synthetic spectro-photometry. Owing to the mass resolution of the dynamical simulations fixed by the number of particles to our disposal, each star-particle has the mass $M_{sp} \sim 10^7 M_\odot$ or so , *i.e.*, each star-particle represents a big assembly of real stars which distribute in mass according to a given initial mass function and are all born in a short burst of star formation, therefore being homogeneous both in age and chemical composition. In this way, each star-particle can

be approximated to a SSP of mass M_{sp}. To derive the Spectral Energy Distribution (SED) of a galaxy of age T we start from the definition of the integrated monochromatic flux generated by its stellar content:

$$F_\lambda(T) = \int_0^T \int_{m_l}^{m_u} S(m,t,Z)\ f_\lambda(m,\tau',Z)\ dt\ dm \tag{10}$$

where $S(m,t,Z)$ denotes the stellar birth-rate and $f_\lambda(m,\tau',Z)$ the monochromatic flux of a real star of mass m, metallicity Z, and age $\tau' = T - t$. Separating $S(m,t,Z)$ into the product of the star formation rate $\Psi(t,Z)$ (expressed in suitable units) and the initial mass function $\phi(m)$, the above integral becomes:

$$F_\lambda(T) = \int_0^T \Psi(t,Z)\ f_{ssp,\lambda}(\tau',Z)\ dt \tag{11}$$

where:

$$f_{ssp,\lambda}(\tau',Z) = \int_{m_l}^{m_u} \phi(m)\ f_\lambda(m,\tau',Z)\ dm \tag{12}$$

is defined as the integrated monochromatic flux of a SSP, *i.e.*, of a coeval, chemically homogeneous assembly of stars with age τ' and metallicity Z. The lower and upper mass limits of integration in equations m_l and m_u respectively, define the mass range within which stars are generated by each event of star formation. Therefore, the stellar content of a galaxy can be modeled as the convolution of many SSPs of different composition and age, each of which is weighted by the rate of star formation at the age at which it was born. Conventionally, the SED and monochromatic flux, and hence luminosities in whatsoever pass-band are calculated assuming that the SSP has a total mass equal to $1\,M_\odot$. Having established the correspondence between the star-particles of the NB-TSPH simulation with the classical SSP and the consistency between the chemical parameters and IMF of the two descriptions, the monochromatic flux and/or luminosity of a galaxy with age T is given by:

$$F_\lambda(T) = \sum_i f_{ssp,\lambda}(\tau_i, Z_i) \times M_{sp,i} \tag{13}$$

where $f_{ssp,\lambda}(\tau_i, Z_i)$ is the monochromatic flux of a SSP of age τ_i and metallicity Z_i and the summation extends over all star-particles. Repeating the same procedure to the whole wavelength interval we get the multi-wavelength SED, from which we can immediately derive magnitudes and colours in whatsoever photometric system. The key quantity to determine is $f_{SSP,\lambda}$ which in turn requires the monochromatic flux $f_\lambda(m,\tau',Z)$, *i.e.*, the flux emitted by a generic star of given luminosity, effective temperature, gravity and chemical composition in course of its life. This requires libraries of stellar models and isochrones at varying age and chemical composition and libraries of stellar spectra as as function of gravity, effective temperature and chemical parameters. The subject is quite complicate to be summarised here. The reader should refer [2,235–237] for exhaustive discussions of all these issues.

Cosmological and Evolutionary Corrections. Since galaxies are observed at different redshifts in an expanding Universe, we need the so-called K-correction and E-corrections that can be easily derived together with magnitudes and colors from the population synthesis technique (see [2,237–242]). A source with apparent magnitude m measured in a photometric pass-band, is related to the absolute

magnitude M, in the emission-frame pass-band, through the cosmological correction, K_{corr}, in the following way [243]: $m = M + DM + K_{corr}$, in which:

$$DM = 5\log_{10}\left[\frac{D_L(z)}{10pc}\right] \qquad \text{where} \qquad D_L(z) = \frac{c}{H_0}(1+z)\int_0^z \frac{dz}{\left[\Omega_M(1+z)^3+\Omega_\Lambda\right]^{\frac{1}{2}}} \tag{14}$$

are the distance modulus and the luminosity distance, respectively (see [244–246], for all details). If the source is at redshift z, then its luminosity is related to its spectral density flux (energy per unit time, unit area, and unit wavelength) by $L(\lambda_e) = 4\pi(1+z)D_L^2 f(\lambda_0)$, where $f(\lambda_0)$ is the monochromatic flux of a galaxy that has been computed as defined in Equation (13). Finally, K_{corr} is:

$$K_{corr} = 2.5\log_{10}(1+z) + 2.5\log_{10}\left[\frac{L(\lambda_0)}{L(\lambda_e)}\right] \tag{15}$$

(see the definition by [247]). To make a fair comparison between objects at different redshifts, one has to derive the rest-frame photometric properties of the observed galaxies (magnitudes, colors, *etc.*) by applying the K-corrections.

In addition, we must also correct these rest-frame quantities for the expected evolutionary changes over the redshift range studied, by applying the so called evolutionary corrections, E_{corr}. The E_{corr} are usually derived assuming a model for the galaxy SED and calculating its evolution with the redshift. In this way we can recover the evolution of the absolute magnitudes and colors as a function of the redshift z, including the effect of the K- and E-corrections on the SED of our models.

From Equation (14) the apparent magnitude, in some broad-band filter and at redshift z, is given by:

$$m(z) = M(z) + E(z) + K(z) + DM(z) \tag{16}$$

Obviously, the relation $t = t(z)$, between the cosmic time t and the redshift z of a stellar population formed at a given redshift z_f, depends on the cosmology considered and the parameters adopted. Following [246]:

$$t(z) = \frac{1}{H_0}\int_z^\infty \frac{dz}{(1+z)\left[\Omega_M(1+z)^3+\Omega_\Lambda\right]^{\frac{1}{2}}} \tag{17}$$

Extinction. Before calculating the E_{corr}, it is worth applying to the theoretical SEDs the effect of extinction of the stellar luminosity caused by the presence of a certain amount of metal-rich gas so that the SEDs get closer to the real ones. Although the task is a complicate issue requiring a careful analysis [248–253], in many studies, the extinction is simply evaluated using the relation proposed long ago by [238]:

$$\tau_\lambda = 3.25(1-\omega_\lambda)^{0.5}(A_\lambda/A_V)_\odot[Z(t)/Z_\odot]^{1.35}G(t) \tag{18}$$

where τ_λ, the effective optical thickness of the gaseous component at a given λ, is a function of: (i) the albedo ω_λ of the grains for which the mean values of 0.4 taken from [254] has been used; (ii) the extinction law A_λ/A_V [255]; (iii) and finally the metallicity $Z(t)$ and gas fraction $G(t) = M_g(t)/M_B$, where M_g and M_B are the current gas and total baryonic mass in the galaxy. The monochromatic flux of

the galaxy with the inclusion of the effect due to extinction, $F_{\lambda,ext}$, can be expressed in function of the monochromatic flux of the rest-frame SED of the model galaxy F_λ (see Equation (13)):

$$F_{\lambda,ext} = F_\lambda \frac{1 - \exp(-\tau_\lambda \sec i)}{\tau_\lambda \sec i} \tag{19}$$

where the right-hand part of the expression takes into account the transmission function for an angle of inclination i; we adopt here $i = 45°$. Although this relation was originally derived for disc galaxies, it can be safely used also in our case. The effect of extinction is included in the SEDs using $Z(t)$ and $G(t)$ obtained from the NB-TSPH simulations. Internal extinction may significantly redden the colours, the effect being particularly important on the color-redshift relation.

Data selection for comparison: a few remarks. The advent of large-scale space and ground-based surveys in a wide range of wavelengths is giving us unprecedented access to statistically large populations of galaxies at different redshifts (and also environments). Prior to anything else it is worth recalling that owing to the enormous amounts of data to handle, the data acquisition process is usually made following automatic procedures that deserve some remarks. (i) *Detection*: At $z > 5$, traditional optical bands, e.g., the Johnson-Cousins UBVRI system, fall below the rest-frame wavelength that corresponds to the Lyman-break spectral feature (1216 Å), where most of the stellar radiation is extinguished by interstellar or intergalactic hydrogen. Because of this, galaxies at $z > 5$ are practically invisible at those photometric bands, and even if they were detected, their colors would provide very little information about their stellar population. The color selection technique, e.g., the UGR-selection of Lyman-Break Galaxies (LBGs) by [95,256,257], has been used in some surveys to identify galaxies at high redshift, dramatically improving the efficiency of spectroscopic surveys at $z > 3$; (ii) *Redshift assignment*: Photometric redshifts are the logical extension of color selection by estimating redshifts and SEDs from many photometric bands. Unlike color selection, photometric redshifts take advantage of all available information, enabling redshift estimates along with the age, star formation rate and mass; (iii) *Morphological classification*: One of the main characteristics of deep photometric surveys is the richness of detected objects, where a significant fraction of them appear as point sources that cannot be neither easily distinguished from real stars nor morphologically classified. Therefore, the classification by means of morphological and photometric criteria is a crucial issue; (iv) *Selection*: Morphological selection of ETGs can be made using automated pipelines that isolate objects on the basis of their two-dimensional light distributions: this is the case of the COSMOS survey. On the other hand, in the case of GOODS, it is possible to select more accurately these objects by correlating a catalog of photometric and spectroscopic redshifts with a morphological one.

Data *vs.* theory: comparison with COSMOS and GOODS. To this aim, reference [237] have applied the population synthesis technique to the NB-TSPH models calculated by [1,134,135] in two different cosmological scenarios: the Standard Cold Dark Matter Cosmology ($\mathrm{S-CDM}$), and the Concordance Cosmology (Λ-CDM, with $\Omega_\Lambda = 0.762$); for these template galaxies, reference [237] have followed the spectro-photometric evolution through the entire history of the Universe; finally and with aid of all this, they have analyzed data from COSMOS [258] and GOODS [259].

(i) The COSMOS official photometric redshift catalog, designed to probe the evolution of galaxies in the context of their large scale structure out to moderate redshift is an ideal workbench to compare theory with data. Details of the COSMOS catalog are described in [260,261]. It covers a 2 square degree

area with deep panchromatic data and includes objects whose total i magnitudes (i^+ or i^*) are brighter than 25. The comparison with the theoretical models limited to the $(B_J - r^+)$ color is shown in the left panel of Figure 18. For the sake of comparison, first they consider all the galaxies from the survey, independently of their classification (yellow dots) and, superposed to them, they use the sub-sample of ETGs selected following the classification suggested by the automated pipeline ($T_{phot} \leq 1.5$). The photometric evolution for our three model galaxies is also shown: the solid line is for the $\mathrm{S} - \mathrm{CDM}$, the dotted-dashed line is for the Λ-CDM model, and the dotted line is for the Λ-CDM$_{mp}$ case. It is worth calling attention that the model Λ-CDM is plotted from z_{ini} down to $z \sim 1$ because it has been stopped at the age of 7 Gyr. The models follow the general trend of the observations and, in particular, are marginally consistent with the group of ETGs up to $z \sim 1$ beyond which the data are too poor to say anything. The observed ETGs are indeed redder than the mean value of the data and theoretical predictions. Concerning the theoretical values, their bluer colors can be ascribed to the tail of star formation extending to the present. Although this minor stellar activity does not significantly affect the gross features of the models (structure, mass distributions *etc.*) it certainly affects the colors making them bluer than desired and expected. However this secondary star formation activity could be a spurious effect. Another point of uncertainty could reside in the selection criteria to identify ETGs.

Figure 18. (**a**) Cosmological evolution with redshift for the $(B_J - r^+)$ color of the COSMOS survey. Both pass-bands are those of the Subaru Telescope. All galaxies of the catalog are shown in yellow. The ETGs selected with the pipeline morphological $T_{phot} < 1.1$ parameter are marked in blue. The galaxy models for the three different cosmological scenarios are shown superimposed to the data, continuous and dotted lines as labeled. The Λ-CDM case is shown for $z > 1$; (**b**) The same as in the left panel but for the $V(F606W) - i(F775W)$ colors of the GOODS survey (ACS-HST pass-bands) for early-type galaxies with spectroscopic (light blue-empty circle) and photometric (blue-filled circles) redshift determination as indicated. Reproduced with permission from [237]. Copyright 2010 Astronomy and Astrophysics.

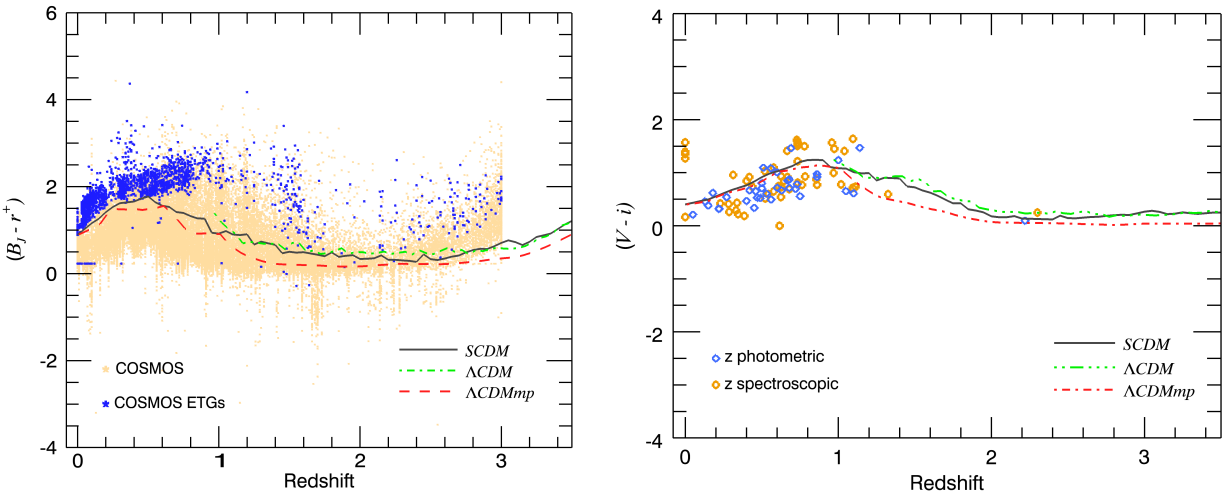

(**a**) (**b**)

(ii) Similar comparison can be made with the GOODS database of [259]. The survey is based on the observations of two separate fields centered on the Hubble Deep Field North (HDFN) and Chandra Deep Field South (CDFS) and includes ultra-deep images from ACS (Advanced Camera for Surveys) on HST, from mid-IR satellite Spitzer, as well as from a number of ground-based facilities. Galaxies exhibit a range of morphologies that are difficult to determine automatically, so a manual classification is often used to test the efficacy of automated classifiers. For this reason, in order to select ETGs, [237] cross-correlated two catalogs: the GOODS - Multi-wavelength Southern Infrared Catalog (GOODS-MUSIC) by [262] to determine the redshift and the one by [151] to fix the morphology. Thanks to this, they recover a data set of galaxies with reliable morphological classification and precise redshift determination. The total amounts to 118 objects. In the right panel of Figure 18, the $(V(F606W) - i(F775W))$ color of this selected sample are shown together with the theoretical predictions. For all of the colors, the agreement between data and theory concerning the photometric, cosmological evolution with redshift is remarkably good. Furthermore, the theoretical colours seem to match the GOODS data much better than the COSMOS values. This clearly shows that the reliability of the morphology classifier plays an important role in these matters. Finally, another possible explanation for the differences between the results from COSMOS and GOODS, could be an intrinsic difference in the samples of observed galaxies (see [237], for all details).

Surface photometry and Kormendy's scale relationship. Starting from the 3-D NB-TSPH simulations and companion spectro-photometry, [237] derived synthetic 2-D images projecting the volume inside a sphere of radius $|z| < 100$ kpc onto the xy plane (sse the left panel of Figure 19. These images are then processed with the same procedures applied to 2D-images of real galaxies, to derive the structural parameters of galaxies, such as the effective radius R_e, the luminosity within R_e, the shape indices through Fourier and Sérsic analysis, the color profiles, and the radial profiles of most of the parameters that define the structure of galaxies. They find that the luminosity profiles of the model galaxies at $z = 0$ can be reasonably fitted with a Sérsic $R^{1/n}$ law. In general, they can recover properties that resemble those of observed galaxies.

The Kormendy Relationship [263,264] is the projection of the Fundamental Plane onto the luminosity-radius plane. It relates $< \mu >_e$ to R_e. Once the dependence on I_e is made explicit we get $R_e \propto I_e^{-0.83}$. Many studies have confirmed that the luminous ETGs in clusters approximately follow the relation $< \mu >_e = \log R_e + const$ found by Kormendy with slope of ~ 3 and intrinsic scatter of $0.3 - 0.4$. The KR for galaxies in clusters at increasing redshift has been claimed to be consistent with passively evolving stellar populations [27,265–271]. On the other hand, some studies have also claimed that the data are consistent with the hierarchical evolutionary scenario [272]. Reference [273], working with cluster ETGs at different redshift, found that the slope of the KR is almost invariant up to $z \sim 0.64$ with value of $\sim 2.91 \pm 0.08$. The homogeneity and the invariance with redshift of these distributions is also suggested by the analysis of the SDSS data by [274]. To compare the models with observational data, reference [237] used the sample of ETGs selected by [275] from the SDSS [276,277]. The comparison is shown in the right panel of Figure 19, which displays the M_r-R_e relation found by [278], $R_e \propto I^{-0.75 \pm 0.01}$ and the three models analyzed by [237]. No case lies close to the mean line, however they all are compatible with the data. Considering the long journey made by the model galaxies plotted in this plane, the agreement is satisfactory even though it can be improved.

Figure 19. (**a**) The 2D-distribution of the optical r-band magnitude in the XY-plane. Superposed are elliptical isophotes (white solid lines). The top panel is for SCDM, the middle panel for Λ-CDM, and the bottom panel for Λ-CDM$_{mp}$; (**b**) Magnitude-Effective Radius relation in the r-band for the ETGs selected from the SDSS DR2 database following the criteria from [275]. Results for the three model galaxies are shown for comparison. Reproduced with permission from [237]. Copyright 2010 Astronomy and Astrophysics.

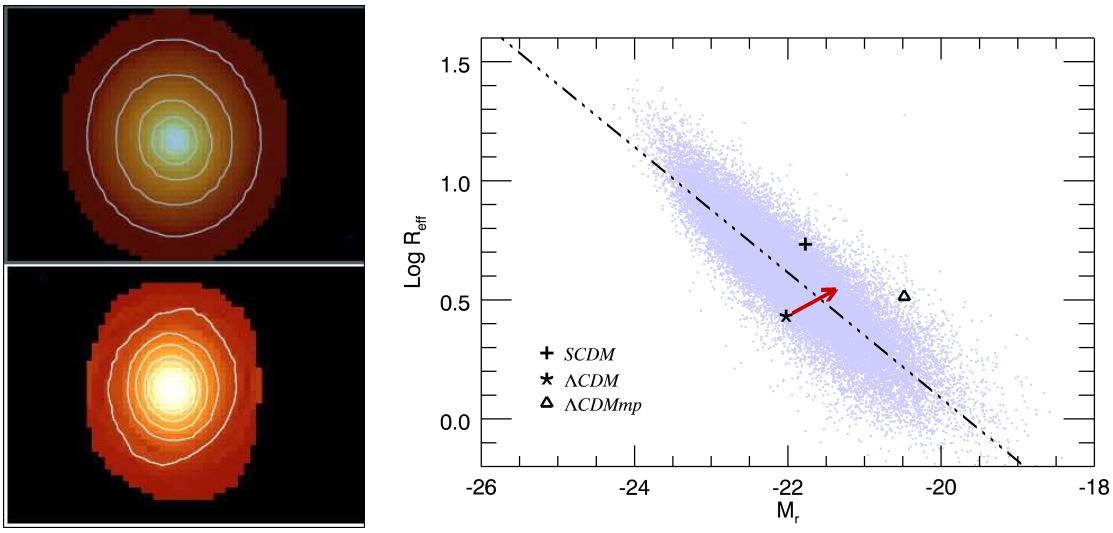

(**a**) (**b**)

7. Conclusions

In this review, we reported on recent studies aimed at (i) exploring the properties of model galaxies for ETGs in the early hierarchical quasi monolithic scenario in the Λ-CDM Universe; (ii) casting light on the origin of the star mass-radius relation of ETGs. In the adopted scenario, mergers of sub-structures made of DM and BM are on purpose let to occur early on during the lifetime of a galaxy, in order to check whether the resulting object may account for the properties of real ETGs without invoking major mergers during the whole life of a galaxy.

The key result is that the SFH is driven by the total mass of the system, the initial over-density with respect to the surrounding medium, and the threshold density inside the gravitational potential well reached by BM gas at the onset of star formation. In brief: (i) At given initial over-density, and star forming efficiency (ϵ_{sf}), the SFH of the model galaxies changes from monolithic to bursting-like mode at decreasing total mass (from big ETGs to small ETGs); (ii) at given total mass the SFH changes from monolithic-like to bursting mode at decreasing initial over-density, and in addition to this the start and peak of stellar activity are gradually shifted toward the present (downsizing and time delay); (iii) at given total mass and initial over-density, the efficiency of star formation (the threshold gas density to ignite the star formation) adds another dimension to the problem in tuning the kind of SFH taking place in a galaxy in between the two paradigm behaviors above and determining the mean dimension of the galaxy component made of stars: large for high efficiencies and relatively small for low efficiencies. Finally, the models of high mass galaxies complete their mass assembly and star formation at redshifts larger than 2 and ever since evolve monolithically on their own. The structural properties of the model

galaxies (surface mass density profiles of BM and DM) nicely agree with the current information on these quantities. Galactic winds are about 10% to 50% of the gas mass in massive and low mass galaxies, respectively. This material is significantly enriched in metals. The mean metallicity and the metallicity gradients are in marginal agreement with current observational data.

The MRR of ETGs stems from the action of several concurring factors: (i) the CGS visualizing the cut-off mass of the galaxy mass distribution at each redshift. It is set by the cosmic growing of gravitationally bounded density perturbations and associated $N(M_{DM}, z)$. The slope of the CGS goes from 0.5 to 1 as the mass increases. It is reminiscent of the slope of the MRR for dissipation-less collapse; (ii) The manifold of lines of equal initial density but different redshift along which pro-haloes of any mass crowd (slope of this mass-radius relation is 1/3 by construction); (iii) given the initial density, collapse redshift, and star formation efficiency, the proto-haloes of different mass filiate baryonic galaxies with certain values of M_s and $R_{1/2}$ at the present time. The baryonic components of galaxies crowd along mass-radius relations whose slope changes from 0.3 to 0.2 or less as the galaxy mass (either total or stellar) decreases. The MRR of ETGs is locus on which the manifold of MRRs of individual BM galaxies of any mass would intersect the CGS. The galaxies at the intersection are close to the cut-mass and evolve in condition closely following the dissipation-less collapse. They trace the MRR of ETGs we observe today.

Finally, the early hierarchical quasi monolithic scenario folded with the classical spectro-photometric synthesis technique predicts SEDs, magnitudes and colors in many photometric systems both in the rest-frame and as a function of the redshift. They can be compared with the photometric data for large samples of galaxies together with the fundamental scale relations such as the Kormendy relations and the Fundamental Plane. Theory and data are in remarkable agreement.

Given the achievements of the new scenario for galaxy formation, it is no longer necessary to consider mergers between proto-galaxies (or disks) as the main way in which massive ETGs are formed. It is most likely, indeed, that this scenario has to be definitely discarded. If so, the general scenario reconciling our understanding of matter aggregation in the Universe on large scales with the compelling evidences about the formation of galaxies is more complicate than commonly assumed. Likely, Nature follows the hierarchical mode when aggregating matter on the scale of groups and clusters, and the early hierarchical quasi monolithic mode when aggregating matter on the scale of individual galaxies. On the other hand galaxy mergers cannot be completely ruled out, simply because we have direct observational evidence of their occurrence. They are beautiful, spectacular events, but not the dominant mechanism by which galaxies (the ETGs, in particular) are assembled and their main features imprinted. The picture emerging from this analysis is that *nature* seems to play the dominant role in building up the ETGs we see today, whereas *nurture* by recurrent captures of small objects is a secondary actor of the fascinating and intriguing story of galaxy formation and evolution. In the forest of the galaxy formation theories, *ex pluribus unum.*

Acknowledgments

We are grateful to Fulvio Buonomo, Umberto Buonomo, Giovanni Carraro, Tommaso Grassi, Cesario Lia, Stefano Pasetto, and Laura Portinari, who all contributed with enthusiasm and dedication to develop the subject of galaxy formation and evolution at the Padova University. We are also grateful to

the anonymous referees that with their comments, remarks, and criticisms greatly helped us to improve the original version of the manuscript.

Author Contributions

Padova Group of Theoretical Astrophysics. Emiliano Merlin: cosmology, galaxy formation and evolution, numerical NB-TSPH models of galaxies. Lorenzo Piovan: theory of population synthesis and chemo-spectro-photometric models of galaxies in presence of dust. Rosaria Tantalo: Theory of population synthesis, line absorption indices, chemo-spectro-photometric models of galaxies. Cesare Chiosi: coordinator. Each author has contributed in a significant way to the reported researches and to the writing of the paper.

Conflicts of Interest

The authors declare no conflicts of interest.

References

1. Merlin, E.; Chiosi, C.; Piovan, L.; Grassi, T.; Buonomo, U.; Barbera, F.L. Formation and evolution of early-type galaxies—III. Dependence of the star formation history on the total mass and initial over-density. *Mon. Not. R. Astron. Soc.* **2012**, *427*, 1530–1554.
2. Bressan, A.; Chiosi, C.; Fagotto, F. Spectrophotometric evolution of elliptical galaxies. 1: Ultraviolet excess and color-magnitude-redshift relations. *Astrophys. J. Suppl.* **1994**, *94*, 63–115.
3. Tantalo, R.; Chiosi, C.; Bressan, A.; Fagotto, F. Spectro-photometric evolution of elliptical galaxies. II. Models with infall. *Astron. Astrophys.* **1996**, *311*, 361–383.
4. Greggio, L. On the metallicity distribution in the nuclei of elliptical galaxies. *Mont. Not. R. Astron. Soc.* **1997**, *285*, 151–166.
5. Burstein, D.; Bertola, F.; Buson, L.M.; Faber, S.M.; Lauer, T.R. The far-ultraviolet spectra of early-type galaxies. *Astrophys. J.* **1988**, *328*, 440–462.
6. Ferguson, H.C.; Davidsen, A.F. The hot stellar component in elliptical galaxies and spiral bulges. I—The far-ultraviolet spectrum of the bulge of M31. *Astrophys. J.* **1993**, *408*, 92–107.
7. Ferguson, H.C.; Davidsen, A.F.; Kriss, G.A.; Blair, W.P.; Bowers, C.W.; Dixon, W.V.D.; Durrance, S.T.; Feldman, P.D.; Henry, R.C.; Kruk, J.W.; *et al.* Constraints on the origin of the ultraviolet upturn in elliptical galaxies from Hopkins Ultraviolet Telescope observations of NGC 1399. *Astrophys. J.* **1991**, *382*, 69–73.
8. Fisher, D.; Franx, M.; Illingworth, G. Line Strengths and Line-Strength Gradients in S0 Galaxies. *Astrophys. J.* **1996**, *459*, doi:10.1086/176873.
9. Carollo, C.M.; Danziger, I.J.; Buson, L. Metallicity Gradients in Early Type Galaxies. *Mon. Not. R. Astron. Soc.* **1993**, *265*, 553–580.
10. Carollo, C.M.; Danziger, I.J. Dynamics and Stellar Populations in Early Type Galaxies. *Mon. Not. R. Astron. Soc.* **1994**, *270*, 523–569.

11. Carollo, C.M.; Danziger, I.J. Colours Line Strengths and Stellar Kinematics of NGC2663 and NGC5018. *Mon. Not. R. Astron. Soc.* **1994**, *270*, 743–768.
12. González, J.J. Line Strength Gradients and Kinematic Profiles in Elliptical Galaxies. Ph.D. Thesis, University of California, Santa Cruz, CA, USA, 1993.
13. Trager, S.C.; Faber, S.M.; Worthey, G.; González, J.J. The Stellar Population Histories of Local Early-Type Galaxies. I. Population Parameters. *Astron. J.* **2000**, *119*, 1645–1676.
14. Trager, S.C.; Faber, S.M.; Worthey, G.; González, J.J. The Stellar Population Histories of Early-Type Galaxies. II. Controlling Parameters of the Stellar Populations. *Astron. J.* **2000**, *120*, 165–188.
15. Faber, S.M.; Worthey, G.; Gonzalez, J.J. Absorption-Line Spectra of Elliptical Galaxies and Their Relation to Elliptical Formation. In *The Stellar Populations of Galaxies*; Barbuy, B., Renzini, A., Eds.; Kluwer Academic Publishers: Dordrecht, The Netherlands, 1992; Voluem 142, p. 255.
16. Worthey, G. Comprehensive stellar population models and the disentanglement of age and metallicity effects. *Astrophys. J. Suppl.* **1994**, *95*, 107–149.
17. Matteucci, F. Abundance ratios in ellipticals and galaxy formation. *Astron. Astrophys.* **1994**, *288*, 57–64.
18. Matteucci, F. Galaxy Evolution. *Fundam. Cosm. Phys.* **1996**, *17*, 283–396.
19. Matteucci, F.; Ponzone, R.; Gibson, B.K. On the trend of [Mg/Fe] among giant elliptical galaxies. *Astron. Astrophys.* **1998**, *335*, 855–866.
20. Greggio, L. The rates of type Ia supernovae—II. Diversity of events at low and high redshifts. *Mon. Not. R. Astron. Soc.* **2010**, *406*, 22–42.
21. Larson, R.B. Effects of supernovae on the early evolution of galaxies. *Mon. Not. R. Astron. Soc.* **1974**, *169*, 229–246.
22. Larson, R.B. Dynamical models for the formation and evolution of spherical galaxies. *Mon. Not. R. Astron. Soc.* **1974**, *166*, 585–616.
23. Chiosi, C.; Carraro, G. Formation and evolution of elliptical galaxies. *Mon. Not. R. Astron. Soc.* **2002**, *335*, 335–357.
24. Tantalo, R.; Chiosi, C. Enhancement of alpha -elements in dynamical models of elliptical galaxies. *Astron. Astrophys.* **2002**, *388*, 396–406.
25. Mehlert, D.; Thomas, D.; Saglia, R.P.; Bender, R.; Wegner, G. Spatially resolved spectroscopy of Coma cluster early-type galaxies. III. The stellar population gradients. *Astron. Astrophys.* **2003**, *407*, 423–435.
26. Mathews, W.G.; Baker, J.C. Galactic Winds. *Astrophys. J.* **1971**, *170*, 241–260.
27. Bower, R.G.; Lucey, J.R.; Ellis, R.S. Precision photometry of early-type galaxies in the Coma and Virgo clusters: A test of the universality of the colour-magnitude relation. I—The data. *Mon. Not. R. Astron. Soc.* **1992**, *254*, 589–613.
28. Bower, R.G.; Lucey, J.R.; Ellis, R.S. Precision Photometry of Early Type Galaxies in the Coma and Virgo Clusters—A Test of the Universality of the Colour—Magnitude Relation. II—Analysis. *Mon. Not. R. Astron. Soc.* **1992**, *254*, 601–613.
29. Schweizer, F.; Seitzer, P. Correlations between UBV colors and fine structure in E and S0 galaxies—A first attempt at dating ancient merger events. *Astron. J.* **1992**, *104*, 1039–1067.

30. Faber, S.M.; Burstein, D.; Dressler, A. Spectrum of the halo of the cD galaxy in Abell 401. *Astron. J.* **1977**, *82*, 941–946.
31. Dressler, A. Internal kinematics of galaxies in clusters. I—Velocity dispersions for elliptical galaxies in Coma and Virgo. *Astrophys. J.* **1984**, *181*, 512–524.
32. Vader, J.P. Multivariate analysis of elliptical galaxies in different environments. *Astrophys. J.* **1986**, *306*, 390–400.
33. Kodama, T.; Arimoto, N. Origin of the colour-magnitude relation of elliptical galaxies. *Astron. Astrophys.* **1997**, *320*, 41–53.
34. Burstein, D.; Faber, S.M.; Gaskell, C.M.; N. Krumm, N. Old stellar populations. I—A spectroscopic comparison of galactic globular clusters, M31 globular clusters, and elliptical galaxies. *Astrophys. J.* **1984**, *287*, 586–609.
35. Faber, S.M.; Friel, D.E.; Burstein, D.; Gaskell, C.M. Old stellar populations. II—An analysis of K-giant spectra. *Astrophys. J. Suppl.* **1985**, *57*, 711–741.
36. Worthey, G. The Controlling Parameters of the Integrated Flux of a Stellar Population. *Publ. Astron. Soc. Pac.* **1993**, *105*, doi:10.1086/133157.
37. Worthey, G.; Faber, S.M.; González, J.J. MG and Fe absorption features in elliptical galaxies. *Astrophys. J.* **1992**, *398*, 69–73.
38. Worthey, G.; Faber, S.M.; González, J.J.; Burstein, D. Old stellar populations. 5: Absorption feature indices for the complete LICK/IDS sample of stars. *Astrophys. J. Suppl.* **1994**, *94*, 687–722.
39. Renzini, A.; Buzzoni, A. Global properties of stellar populations and the spectral evolution of galaxies. In *Spectral Evolution of Galaxies*; Chiosi, C., Renzini, A., Eds.; Reidel: Dordecht, The Netherlands, 1986; pp. 195–231.
40. Bressan, A.; Chiosi, C.; Tantalo, R. Probing the age of elliptical galaxies. *Astron. Astrophys.* **1996**, *311*, 425–445.
41. Rakos, K.; Schombert, J.; Maitzen, H.M.; Prugovecki, S.; Odell, A. Ages and Metallicities of Fornax Dwarf Elliptical Galaxies. *Astron. J.* **2001**, *121*, 1974–1991.
42. Tantalo, R.; Chiosi, C.; Bressan, A. Ages and metallicities in elliptical galaxies from the H_β, $\langle Fe \rangle$, and Mg_2 diagnostics. *Astron. Astrophys.* **1998**, *333*, 419–432.
43. Tantalo, R.; Chiosi, C.; Bressan, A.; Marigo, P.; Portinari, L. Spectro-photometric evolution of elliptical galaxies. III. Infall models with gradients in mass density and star formation. *Astron. Astrophys.* **1998**, *335*, 823–846.
44. Kuntschner, H. The Star Formation History of Early-Type Galaxies in the Fornax Cluster. Ph.D. Thesis, University Durham, Durham, UK, 1998,
45. Kuntschner, H.; Davies, R.L. The ages and metallicities of early-type galaxies in the Fornax cluster. *Mon. Not. R. Astron. Soc.* **1998**, *295*, 129–l33.
46. Jorgensen, I. E and S0 galaxies in the central part of the Coma cluster: Ages, metal abundances and dark matter. *Mon. Not. R. Astron. Soc.* **1999**, *306*, 607–636.
47. Kuntschner, H. The stellar populations of early-type galaxies in the Fornax cluster. *Mon. Not. R. Astron. Soc.* **2000**, *315*, 184–208.

48. Poggianti, B.M.; Bridges, T.J.; Mobasher, B.; Carter, D.; Doi, M.; Iye, M.; Kashikawa, N.; Komiyama, Y.; Okamura, S.; Sekiguchi, M.; *et al.* A Photometric and Spectroscopic Study of Dwarf and Giant Galaxies in the Coma Cluster. III. Spectral Ages and Metallicities. *Astrophys. J.* **2001**, *562*, 689–712.
49. Kuntschner, H. The Stellar Populations of Early-Type Galaxies in the Fornax Cluster. *Astrophys. Space Sci.* **2001**, *276*, 885–891.
50. Kuntschner, H.; Lucey, J.R.; Smith, R.J.; Hudson, M.J.; Davies, R.L. On the dependence of spectroscopic indices of early-type galaxies on age, metallicity and velocity dispersion. *Mon. Not. R. Astron. Soc.* **2001**, *323*, 615–629.
51. Vazdekis, A.; Kuntschner, H.; Davies, R.L.; Arimoto, N.; Nakamura, O.; Peletier, R. On the Origin of the Color-Magnitude Relation in the Virgo Cluster. *Astrophys. J.* **2001**, *551*, 127–130.
52. Davies, R.L.; Kuntschner, H.; Emsellem, E.; Bacon, R.; Bureau, M.; Carollo, C.M.; Copin, Y.; Miller, B.M.; Monnet, G.; Peletier, R.F.; *et al.* Galaxy Mapping with the SAURON Integral-Field Spectrograph: The Star Formation History of NGC 4365. *Astrophys. J. Lett.* **2001**, *548*, doi:10.1086/318930.
53. Maraston, C.; Greggio, L.; Renzini, A.; Ortolani, S.; Saglia, R.P.; Puzia, T.H.; Kissler-Patig, M. Integrated spectroscopy of bulge globular clusters and fields. II. Implications for population synthesis models and elliptical galaxies. *Astron. Astrophys.* **2003**, *400*, 823–840.
54. Thomas, D.; Maraston, C.; Bender, R. Stellar population models of Lick indices with variable element abundance ratios. *Mon. Not. R. Astron. Soc.* **2003**, *339*, 897–911.
55. Thomas, D.; Maraston, C.; Bender, R. New clues on the calcium under-abundance in early-type galaxies. *Mon. Not. R. Astron. Soc.* **2003**, *343*, 279–283.
56. Thomas, D.; Maraston, C. The impact of alpha /Fe enhanced stellar evolutionary tracks on the ages of elliptical galaxies. *Astron. Astrophys.* **2003**, *401*, 429–432.
57. Tantalo, R.; Chiosi, C. Star formation history in early-type galaxies. I. The line absorption indices diagnostics. *Mon. Not. R. Astron. Soc.* **2004**, *353*, 405–421.
58. Weiss, A.; Peletier, R.F.; Matteucci, F. Synthetic metal line indices for elliptical galaxies from super metal-rich α-enhanced stellar models. *Astron. Astrophys.* **1995**, *296*, 73–89.
59. Salasnich, B.; Girardi, L.; Weiss, A.; Chiosi, C. Evolutionary tracks and isochrones for α-enhanced stars. *Astron. Astrophys.* **2000**, *361*, 1023–1035.
60. Trager, S.C.; Worthey, G.; Faber, S.M.; Burstein, D.; González, J.J. Old Stellar Populations. VI. Absorption-Line Spectra of Galaxy Nuclei and Globular Clusters. *Astrophys. J. Suppl.* **1998**, *116*, 1–28.
61. Idiart, T.P.; de Freitas-Pacheco, J.A. Empirical Calibration of Metallicity Indices for Single Stellar Populations. *Astron. J.* **1995**, *109*, 2218–2228.
62. Cenarro, A.J.; Cardiel, N.; Gorgas, J.; Peletier, R.F.; Vazdekis, A.; Prada, F. Empirical calibration of the near-infrared Ca II triplet—I. The stellar library and index definition. *Mon. Not. R. Astron. Soc.* **2001**, *326*, 959–980.
63. Cenarro, A.J.; Gorgas, J.; Cardiel, N.; Vazdekis, A.; Peletier, R.F. Empirical calibration of the near-infrared Ca II triplet—III. Fitting functions. *Mon. Not. R. Astron. Soc.* **2002**, *329*, 863–876.

64. Sánchez-Blázquez, P.; Peletier, R.; Vazdekis, A.; Gorgas, J.; Cardiel, N.; Selam, S.; Falcón, J. A New Spectral Stellar Library for Population Synthesis. In *Highlights of Spanish Astrophysics III*; Springer: Berlin, Germany, 2003.
65. Tantalo, R.; Chiosi, C. Measuring age, metallicity and abundance ratios from absorption-line indices. *Mon. Not. R. Astron. Soc.* **2004**, *353*, 917–940.
66. Tantalo, R.; Chiosi, C.; Piovan, L. New response functions for absorption-line indices from high-resolution spectra. *Astron. Astrophys.* **2007**, *462*, 481–494.
67. Salaris, M.; and A. Chieffi, A.; and O. Straniero, O. The α-enhanced isochrones and their impact on the FITS to the Galactic globular cluster system. *Astrophys. J.* **1993**, *414*, 580–600.
68. Tantalo, R.; Chiosi, C.; Piovan, L. New Response Functions for Absorption-Line Indices from High-Resolution Spectra. *Astron. Soc. Pac. Conf. Ser.* **2007**, *374*, 373–378.
69. Tripicco, M.J.; Bell, R.A. Modeling the LICK/IDS Spectral Feature Indices Using Synthetic Spectra. *Astron. J.* **1995**, *110*, doi:10.1086/117744.
70. Munari, U.; Sordo, R.; Castelli, F.; Zwitter, T. An extensive library of 2500–10500 Å synthetic spectra. *Astron. Astrophys.* **2005**, *442*, 1127–1134.
71. Vazdekis, A.; Peletier, R.F.; Beckman, J.E.; Casuso, E. A New Chemo-evolutionary Population Synthesis Model for Early-Type Galaxies. II. Observations and Results. *Astrophys. J. Suppl.* **1997**, *111*, 203–232.
72. Davies, R.L.; Sadler, E.M.; Peletier, R. Line-strength gradients in elliptical galaxies. *Mon. Not. R. Astron. Soc.* **1993**, *262*, 650–680.
73. Chiosi, C.; Bressan, A.; Portinari, L.; Tantalo, R. A new scenario of galaxy evolution under a universal Initial Mass Function. *Astron. Astrophys.* **1998**, *339*, 355–381.
74. Longhetti, M.; Bressan, A.; Chiosi, C.; Rampazzo, R. Star formation history of early-type galaxies in low density environments. IV. What do we learn from nuclear line-strength indices? *Astron. Astrophys. Suppl.* **2000**, *353*, 917–928.
75. Spergel, D.N.; Verde, L.; Pereis, H.V.; Komatsu, E.; Nolta, M. R.; Bennett, C. L.; Halpern, M.; Hinshaw, G.; Jarosik, N.; Kogut, A.; *et al.* First-Year Wilkinson Microwave Anisotropy Probe (WMAP) Observations: Determination of Cosmological Parameters. *Astrophys. J. Suppl.* **2003**, *148*, 175–194.
76. Sarzi, M.; Falcón-Barroso, J.; Davies, R.L.; Bacon, R.; Bureau, M.; Cappellari, M.; de Zeeuw, P.T.; Emsellem, E.; Fathi, K.; Krajnović, D.; *et al.* The SAURON project—V. Integral-field emission-line kinematics of 48 elliptical and lenticular galaxies. *Mon. Not. R. Astron. Soc.* **2006**, *366*, 1151–1200.
77. Forbes, D.A.; Terlevich, A.I. Age Estimates for Galaxies in Groups. *Astron. Soc. Pac. Conf.* **2000**, *209*, 335–338.
78. Poggianti, B.M.; Bridges, T.J.; Carter, D.; Mobasher, B.; Doi, M.; Iye, M.; Kashikawa, N.; Komiyama, Y.; Okamura, S.; Sekiguchi, M.; *et al.* Ages of S0 and Elliptical Galaxies in the Coma Cluster. *Astrophys. J.* **2001**, *563*, 118–123.
79. Bower, R.G.; Kodama, T.; Terlevich, A. The colour-magnitude relation as a constraint on the formation of rich cluster galaxies. *Mon. Not. R. Astron. Soc.* **1998**, *299*, 1193–1208.

80. Longhetti, M.; Rampazzo, R.; Bressan, A.; Chiosi, C. Star formation history of early-type galaxies in low density environments. I. Nuclear line-strength indices. *Astron. Astrophys. Suppl.* **1998**, *130*, 251–265.
81. Longhetti, M.; Rampazzo, R.; Bressan, A.; Chiosi, C. Star formation history of early-type galaxies in low density environments. II. Kinematics. *Astron. Astrophys. Suppl.* **1998**, *130*, 267–283.
82. Longhetti, M.; Bressan, A.; Chiosi, C.; Rampazzo, R. Star formation history of early-type galaxies in low density environments. V. Blue line-strength indices for the nuclear region. *Astron. Astrophys. Suppl.* **1999**, *345*, 419–429.
83. Buson, L.M.; Bertola, F.; Cappellari, M.; Chiosi, C.; Dressler, A.; Oemler, A., Jr. Ultraviolet imaging of the galaxy cluster CL 0939 + 4713 (Abell 851) at $z = 0.411$. *Astrophys. J.* **2000**, *531*, 684–692.
84. Graham, A.W. Elliptical and Disk Galaxy Structure and Modern Scaling Laws. *Planets Stars Stellar Syst.* **2013**, *6*, 91–139.
85. Graham, A.W. Scaling laws in disk galaxies. *ArXiv E-Prints*, **2013**, arXiv:1311.7207.
86. Bender, R.; Burstein, D.; Faber, S.M. Dynamically hot galaxies. I—Structural properties. *Astrophys. J.* 1992, **399**, 462–477.
87. Ciotti, L.; Lanzoni, B.; Renzini, A. The tilt of the fundamental plane of elliptical galaxies—I. Exploring dynamical and structural effects. *Mon. Not. R. Astron. Soc.* **1996**, *282*, 1–12.
88. Renzini, A.; Ciotti, L. Transverse Dissections of the Fundamental Planes of Elliptical Galaxies and Clusters of Galaxies. *Astrophys. J.* **1993**, *416*, doi:10.1086/187068.
89. Burstein, D.; Bender, R.; Faber, S.; Nolthenius, R. Global Relationships Among the Physical Properties of Stellar Systems. *Astron. J.* **1997**, *114*, doi:10.1086/118570.
90. Renzini, A. Stellar Population Diagnostics of Elliptical Galaxy Formation. *Annu. Rev. Astron. Astrophys.* **2006**, *44*, 141–192.
91. Bromm, V.; Yoshida, N. The First Galaxies. *Annu. Rev. Astron. Astrophys.* **2011**, *49*, 373–407.
92. Silk, J.; Mamon, G.A. The current status of galaxy formation. *Res. Astron. Astrophys.* **2012**, *12*, 917–946.
93. Courteau, S.; Cappellari, M.; de Jong, R.S.; Dutton, A.A.; Emsellem, E.; Hoekstra, H.; Koopmans, L.V.E.; Mamon, G.A.; Maraston, C.; Treu, T. *et al.* Galaxy Masses: A Review. *ArXiv E-Prints*, **2013**, arXiv:1309.3276.
94. Madau, P.; Ferguson, H.C.; Dickinson, M.E.; Giavalisco, M.; Steidel, C.C.; Fruchter, A. High-redshift galaxies in the Hubble Deep Field: Colour selection and star formation history to $z \sim 4$. *Mon. Not. R. Astron. Soc.* **1996**, *283*, 1388–1404.
95. Steidel, C.C.; Adelberger, K.L.; Giavalisco, M.; Dickinson, M.; Pettini, M. Lyman-Break Galaxies at $z > 4$ and the Evolution of the Ultraviolet Luminosity Density at High Redshift. *Astrophys. J.* **1999**, *519*, 1–17.
96. Stanway, E.R.; Bunker, A.J.; McMahon, R.G. Lyman break galaxies and the star formation rate of the Universe at $z \sim 6$. *Mon. Not. R. Astron. Soc.* **2003**, *342*, 439–445.
97. Dickinson, M.; Stern, D.; Giavalisco, M.; Ferguson, H.C.; Tsvetanov, Z.; Chornock, R.; Cristiani, S.; Dawson, S.; Dey, A.; Filippenko, A.V.; *et al.* Color-selected Galaxies at $z \sim 6$ in the Great Observatories Origins Deep Survey. *Astrophys. J. Lett.* **2004**, *600*, 99–102.

98. Zheng, W.; Postman, M.; Zitrin, A.; Moustakas, J.; Shu, X.; Jouvel, S.; Høst, O.; Molino, A.; Bradley, L.; Coe, D.; *et al.* A magnified young galaxy from about 500 million years after the Big Bang. *Nature* **2012**, *489*, 406–408.
99. Bouwens, R.; Bradley, L.; Zitrin, A.; Coe, D.; Franx, M.; Zheng, W.; Smit, R.; Host, O.; Postman, M.; Moustakas, L.; *et al.* A Census of Star-Forming Galaxies in the $z \sim 9$–10 Universe Based on HST + Spitzer Observations Over 19 CLASH Clusters: Three Candidate $z \sim 9$–10 Galaxies and Improved Constraints on the Star Formation Rate Density at $z \sim 9.2$. *ArXiv E-Prints*, **2012**, arXiv:1211.2230.
100. Oesch, P.A.; Bouwens, R.J.; Illingworth, G.D.; Labbé, I.; Trenti, M.; Gonzalez, V.; Carollo, C.M.; Franx, M.; van Dokkum, P.G.; Magee, D. Expanded Search for $z \sim 10$ Galaxies from HUDF09, ERS, and CANDELS Data: Evidence for Accelerated Evolution at $z \geq 8$? *Astrophys. J.* **2012**, *745*, doi:10.1088/0004-637X/745/2/110.
101. Rowan-Robinson, M. Panchromatic radiation from galaxies as a probe of galaxy formation and evolution. In Proceedings of the IAU Symposium 284, Preston, UK, 5–9 September 2012; pp. 446–455.
102. Tegmark, M.; Silk, J.; Rees, M.J.; Blanchard, A.; Abel, T.; Palla, F. How Small Were the First Cosmological Objects? *Astrophys. J.* **1997**, *474*, 1–12
103. Gao, L.; Yoshida, N.; Abel, T.; Frenk, C.S.; Jenkins, A.; Springel, V. The first generation of stars in the Λ cold dark matter cosmology. *Mont. Not. R. Astron. Soc.* **2007**, *378*, 449–468.
104. Gao, Y.; Carilli, C.L.; Solomon, P.M.; Vanden Bout, P.A. HCN Observations of Dense Star-forming Gas in High-Redshift Galaxies. *Astrophys. J. Lett.* **2007**, *660*, 93–96.
105. Marchesini, D.; Whitaker, K.E.; Brammer, G.; van Dokkum, P.G.; Labbé, I.; Muzzin, A.; Quadri, R.F.; Kriek, M.; Lee, K.-S.; Rudnick, G.; *et al.* The Most Massive Galaxies at $3.0 < z < 4.0$ in the Newfirm Medium-band Survey: Properties and Improved Constraints on the Stellar Mass Function. *Astrophys. J.* **2010**, *725*, 1277–1295.
106. Mortlock, D.J.; Warren, S.J.; Venemans, B.P.; Patel, M.; Hewett, P.C.; McMahon, R.G.; Simpson, C.; Theuns, T.; Gonzáles-Solares, E.A.; Adamson, A.; *et al.* A luminous quasar at a redshift of $z = 7.085$. *Nature* **2011**, *474*, 616–619.
107. Shapley, A.E.; Steidel, C.C.; Adelberger, K.L.; Dickinson, M.; Giavalisco, M.; Pettini, M. The Rest-Frame Optical Properties of $z \simeq 3$ Galaxies. *Astrophys. J.* **2001**, *562*, 95–123.
108. Carilli, C.L.; Bertoldi, F.; Rupen, M.P.; Fan, X.; Strauss, M.A.; Menten, K.M.; Kreysa, E.; Schneider, D.P.; Bertarini, A.; Yun, M.S.; *et al.* A 250 GHz Survey of High-Redshift Quasars from the Sloan Digital Sky Survey. *Astrophys. J.* **2001**, *555*, 625–632.
109. Robson, I.; Priddey, R.S.; Isaak, K.G.; McMahon, R.G. Submillimetre observations of $z > 6$ quasars. *Mon. Not. R. Astron. Soc.* **2004**, *351*, 29–33.
110. Wang, R.; Carilli, C.L.; Wagg, J.; Bertoldi, F.; Walter, F.; Menten, K.M.; Omont, A.; Cox, P.; Strauss, M.A.; Fan, X.; *et al.* Thermal Emission from Warm Dust in the Most Distant Quasars. *Astrophys. J.* **2008**, *687*, 848–858.
111. Wang, R.; Wagg, J.; Carilli, C.L.; Benford, D.J.; Dowell, C.D.; Bertoldi, F.; Walter, F.; Menten, K.M.; Omont, A.; Cox, P.; *et al.* SHARC-II 350 μ Observations of Thermal Emission from Warm Dust in $z \geq 5$ Quasars. *Astron. J.* **2008**, *135*, 1201–1206.

112. Michałowski, M.J.; Hjorth, J.; Castro Cerón, J.M.; Watson, D. The Nature of GRB-Selected Submillimeter Galaxies: Hot and Young. *Astrophys. J.* **2008**, *672*, 817–824.
113. Michałowski, M.J.; Murphy, E.J.; Hjorth, J.; Watson, D.; Gall, C.; Dunlop, J.S. Dust grain growth in the interstellar medium of $5 < z < 6.5$ quasars. *Astron. Astrophys.* **2010**, *522*, doi:10.1051/0004-6361/201014902.
114. Michałowski, M.J.; Watson, D.; Hjorth, J. Rapid Dust Production in Submillimeter Galaxies at $z > 4$? *Astrophys. J.* **2010**, *712*, 942–950.
115. Gall, C.; Andersen, A.C.; Hjorth, J. Genesis and evolution of dust in galaxies in the early Universe. I. Modelling dust evolution in starburst galaxies. *Astron. Astrophys.* **2011**, *528*, doi:10.1051/0004-6361/201015286.
116. Gall, C.; Andersen, A.C.; Hjorth, J. Genesis and evolution of dust in galaxies in the early Universe. II. Rapid dust evolution in quasars at $z > 6$. *Astron. Astrophys.* **2011**, *528*, doi:10.1051/0004-6361/201015605.
117. Gall, C.; Hjorth, J.; Andersen, A.C. Production of dust by massive stars at high redshift. *Astron. Astrophys. Rev.* **2011**, *19*, doi:10.1007/s00159-011-0043-7.
118. Dwek, E.; Galliano, F.; Jones, A. The Cycle of Dust in the Milky Way: Clues from the High-Redshift and Local Universe. In Proceedings of the Cosmic Dust—Near and Far, Heidelberg, Germany, 8–12 September 2008; p. 183.
119. Draine, B.T. Interstellar Dust Models and Evolutionary Implications. In Proceedings of the Cosmic Dust—Near and Far, Heidelberg, Germany, 8–12 September 2008; Henning, T., Grün, E., Steinacker, J., Eds.; p. 453.
120. Dwek, E.; Cherchneff, I. The Origin of Dust in the Early Universe: Probing the Star Formation History of Galaxies by Their Dust Content. *Astrophys. J.* **2011**, *727*, doi:10.1088/0004-637X/727/2/63.
121. González, V.; Labbé, I.; Bouwens, R.J.; Illingworth, G.; Franx, M.; Kriek, M. Evolution of Galaxy Stellar Mass Functions, Mass Densities, and Mass-to-light Ratios from $z \sim 7$ to $z \sim 4$. *Astrophys. J. Lett.* **2011**, *735*, doi:10.1088/2041-8205/735/2/L34.
122. Lukić, Z.; Heitmann, K.; Habib, S.; Bashinsky, S.; Ricker, P.M. The Halo Mass Function: High-Redshift Evolution and Universality. *Astrophys. J.* **2007**, *671*, 1160–1181.
123. Schechter, P. An analytic expression for the luminosity function for galaxies. *Astrophys. J.* **1976**, *203*, 297–306.
124. Silk, J. On the fragmentation of cosmic gas clouds. I—The formation of galaxies and the first generation of stars. *Astrophys. J.* **1977**, *211*, 638–648.
125. Silk, J. On the fragmentation of cosmic gas clouds. II—Opacity-limited star formation. *Astrophys. J.* **1977**, *211*, 152–160.
126. Silk, J. On the fragmentation of cosmic gas clouds. III—The initial stellar mass function. *Astrophys. J.* **1977**, *211*, 718–724.
127. Rodighiero, G.; Daddi, E.; Baronchelli, I.; Cimatti, A.; Renzini, A.; Aussel, H.; Popesso, P.; Lutz, D.; Andreani, P.; Berta, S.; *et al.* The Lesser Role of Starbursts in Star Formation at $z = 2$. *Astrophys. J. Lett.* **2011**, *739*, doi:10.1088/2041-8205/739/2/L40.

128. Kennicutt, R.C., Jr.; Calzetti, D.; Walter, F.; Helou, G.; Hollenbach, D.J.; Armus, L.; Bendo, G.; Dale, D.A.; Draine, B.T.; Engelbracht, C.W.; *et al.* Star Formation in NGC 5194 (M51a). II. The Spatially Resolved Star Formation Law. *Astrophys. J.* **2007**, *671*, 333–348.
129. Krumholz, M.R.; Dekel, A.; McKee, C.F. A Universal, Local Star Formation Law in Galactic Clouds, nearby Galaxies, High-redshift Disks, and Starbursts. *Astrophys. J.* **2012**, *745*, doi:10.1088/0004-637X/745/1/69.
130. Schawinski, K.; Thomas, D.; Sarzi, M.; Maraston, C.; Kaviraj, S.; Joo, S.-J.; Yi, S.K.; Silk, J. Observational evidence for AGN feedback in early-type galaxies. *Mon. Not. R. Astron. Soc.* **2007**, *382*, 1415–1431.
131. Weinmann, S.M.; Pasquali, A.; Oppenheimer, B.D.; Finlator, K.; Mendel, J.T.; Crain, R.A.; Macciò, A.V. A fundamental problem in our understanding of low-mass galaxy evolution. *Mon. Not. R. Astron. Soc.* **2012**, *426*, 2797–2812.
132. Lilly, S.J.; Carollo, C.M.; Pipino, A.; Renzini, A.; Peng, Y. Gas Regulation of Galaxies: The Evolution of the Cosmic Specific Star Formation Rate, the Metallicity-Mass-Star-formation Rate Relation, and the Stellar Content of Halos. *Astrophys. J.* **2013**, *772*, doi:10.1088/0004-637X/772/2/119.
133. Lilly, S.J.; Peng, Y.; Renzini, A.; Carollo, C.M. A Simple Continuity Approach to Galaxy Evolution. *Astron. Soc. Pac. Conf. Ser.* **2013**, *477*, 11–20.
134. Merlin, E.; Chiosi, C. Formation and evolution of early-type galaxies. II. Models with quasi-cosmological initial conditions. *Astron. Astrophys.* **2006**, *457*, 437–453.
135. Merlin, E.; Chiosi, C. Simulating the formation and evolution of galaxies: Multi-phase description of the interstellar medium, star formation, and energy feedback. *Astron. Astrophys.* **2007**, *473*, 733–745.
136. Merlin, E. Simulating the Formation and Evolution of Galaxies. Methods and Results. Ph.D. Thesis, University of Padova, Padova, Italy, 2009.
137. Merlin, E.; Buonomo, U.; Grassi, T.; Piovan, L.; Chiosi, C. EvoL: The new Padova Tree-SPH parallel code for cosmological simulations. I. Basic code: Gravity and hydrodynamics. *Astron. Astrophys.* **2010**, *513*, doi:10.1051/0004-6361/200913514.
138. Tollerud, E.J.; Bullock, J.S.; Graves, G.J.; Wolf, J. From Galaxy Clusters to Ultra-faint Dwarf Spheroidals: A Fundamental Curve Connecting Dispersion-supported Galaxies to Their Dark Matter Halos. *Astrophys. J.* **2011**, *726*, doi:10.1088/0004-637X/726/2/108.
139. Springel, V. The cosmological simulation code GADGET-2. *Mon. Not. R. Astron. Soc.* **2005**, *364*, 1105–1134.
140. Springel, V.; White, S.D.M.; Jenkins, A.; Frenk, C.S.; Yoshida, N.; Gao, L.; Navarro, J.; Thacker, R.; Croton, D.; Helly, J.; *et al.* Simulations of the formation, evolution and clustering of galaxies and quasars. *Nature* **2005**, *435*, 629–636.
141. Springel, V. E pur si muove: Galilean-invariant cosmological hydrodynamical simulations on a moving mesh. *Mon. Not. R. Astron. Soc.* **2010**, *401*, 791–851.
142. Springel, V. Smoothed Particle Hydrodynamics in Astrophysics. *Annu. Rev. Astron. Astrophys.* **2010**, *48*, 391–430.

143. Lacey, C.; Cole, S. Merger rates in hierarchical models of galaxy formation. *Mon. Not. R. Astron. Soc.* **1993**, *262*, 627–649.
144. Benson, A.J. GALACTICUS: A semi-analytic model of galaxy formation. *N. Astron.* **2012**, *17*, 175–197.
145. De Lucia, G.; Springel, V.; White, S.D.M.; Croton, D.; Kauffmann, G. The formation history of elliptical galaxies. *Mon. Not. R. Astron. Soc.* **2006**, *366*, 499–509.
146. Almeida, C.; Baugh, C.M.; Lacey, C.G. The structural and photometric properties of early-type galaxies in hierarchical models. *Mon. Not. R. Astron. Soc.* **2007**, *376*, 1711–1726.
147. De Lucia, G.; Blaizot, J. The hierarchical formation of the brightest cluster galaxies. *Mon. Not. R. Astron. Soc.* **2007**, *375*, 2–14.
148. González, J.E.; Lacey, C.G.; Baugh, C.M.; Frenk, C.S.; Benson, A.J. Testing model predictions of the cold dark matter cosmology for the sizes, colours, morphologies and luminosities of galaxies with the SDSS. *Mon. Not. R. Astron. Soc.* **2009**, *397*, 1254–1274.
149. Parry, O.H.; Eke, V.R.; Frenk, C.S. Galaxy morphology in the ΛCDM cosmology. *Mon. Not. R. Astron. Soc.* **2009**, *396*, 1972–1984.
150. De Lucia, G.; Fontanot, F.; Wilman, D.; Monaco, P. Times, environments and channels of bulge formation in a Lambda cold dark matter cosmology. *Mon. Not. R. Astron. Soc.* **2011**, *414*, 1439–1454.
151. Bundy, K.; Ellis, R.S.; Conselice, C.J. The Mass Assembly Histories of Galaxies of Various Morphologies in the GOODS Fields. *Astrophys. J.* **2005**, *625*, 621–632.
152. Bundy, K.; Ellis, R.S.; Conselice, C.J.; Taylor, J.E.; Cooper, M.C.; Willmer, C.N.A.; Weiner, B.J.; Coil, A.L.; Noeske, K.G.; Eisenhardt, P.R.M. The Mass Assembly History of Field Galaxies: Detection of an Evolving Mass Limit for Star-Forming Galaxies. *Astrophys. J.* **2006**, *651*, 120–141.
153. Bundy, K.; Treu, T.; Ellis, R.S. The Mass Assembly History of Spheroidal Galaxies: Did Newly Formed Systems Arise via Major Mergers? *Astrophys. J. Lett.* **2007**, *665*, 5–8.
154. Barnes, J.; Hut, P. A Hierarchical O(NlogN) Force-Calculation Algorithm. *Nature* **1986**, *324*, 446–449.
155. Monaghan, J.J. Smoothed particle hydrodynamics. *Annu. Rev. Astron. Astrophys.* **1992**, *30*, 543–574.
156. Carraro, G.; Lia, C.; Chiosi, C. Galaxy formation and evolution—I. The Padua tree-sph code (pd-sph). *Mon. Not. R. Astron. Soc.* **1998**, *297*, 1021–1040.
157. Buonomo, F.; Carraro, G.; Chiosi, C.; Lia, C. Galaxy formation and evolution - II. Energy balance, star formation and feedback. *Mon. Not. R. Astron. Soc.* **2000**, *312*, 371–379.
158. Lia, C.; Portinari, L.; Carraro, G. Star formation and chemical evolution in smoothed particle hydrodynamics simulations: A statistical approach. *Mon. Not. R. Astron. Soc.* **2002**, *330*, 821–836.
159. Hinshaw, G.; Weiland, J.L.; Hill, R.S.; Odegard, N.; Larson, D.; Bennett, C.L.; Dunkley, J.; Gold, B.; Greason, M.R.; Jarosik, N.; *et al.* Five-Year Wilkinson Microwave Anisotropy Probe Observations: Data Processing, Sky Maps, and Basic Results. *Astrophys. J. Suppl.* **2009**, *180*, 225–245.

160. Bertschinger, E. COSMICS: Cosmological Initial Conditions and Microwave Anisotropy Codes. *ArXiv E-Prints*, **1995**, arXiv:astro-ph/9506070.
161. Katz, N.; Gunn, J.E. Dissipational galaxy formation. I—Effects of gasdynamics. *Astrophys. J.* **1991**, *337*, 365–381.
162. Kawata, D. Galaxy Formation from a Low-Spin Density Perturbation in a CDM Universe. *Publ. Astron. Soc. Jpn.* **1999**, *51*, 931–941.
163. White, S.D.M. Angular momentum growth in protogalaxies. *Astrophys. J.* **1984**, *286*, 38–41.
164. Press, W.H.; Schechter, P. Formation of Galaxies and Clusters of Galaxies by Self-Similar Gravitational Condensation. *Astrophys. J.* **1974**, *187*, 425–438.
165. Sheth, R.K.; Mo, H.J.; Tormen, G. Ellipsoidal collapse and an improved model for the number and spatial distribution of dark matter haloes. *Mon. Not. R. Astron. Soc.* **2001**, *323*, 1–12.
166. Warren, S.; Lawrence, A.; Almaini, O.; Cirasuolo, M.; Foucaud, S.; Hambly, N.; Hewett, P.; Jameson, R.; Leggett, S.; Lodieu, N.; *et al.* Early Science Results from the UKIDSS ESO Public Survey. *Messenger* **2006**, *126*, 7–10.
167. Power, C.; Knebe, A. The impact of box size on the properties of dark matter haloes in cosmological simulations. *Mon. Not. R. Astron. Soc.* **2006**, *370*, 691–701.
168. Bryan, G.L.; Norman, M.L. Statistical Properties of X-Ray Clusters: Analytic and Numerical Comparisons. *Astrophys. J.* **1998**, *495*, doi:10.1086/305262.
169. Churches, D.K.; Nelson, A.H.; Edmunds, M.G. Numerical simulations of the formation and chemical evolution of galaxies. *Mon. Not. R. Astron. Soc.* **2001**, *327*, 610–622.
170. Lada, C.J.; Lada, E.A. Embedded Clusters in Molecular Clouds. *Ann. Rev. Astron. Astrophs.* **2003**, *41*, 57–115.
171. Krumholz, M.R.; Tan, J.C. Slow Star Formation in Dense Gas: Evidence and Implications. *Astrophys. J.* **2007**, *654*, 304–315.
172. Sutherland, R.S.; Dopita, M.A. Cooling functions for low-density astrophysical plasmas. *Astrophys. J. Suppl.* **1993**, *88*, 253–327.
173. Hollenbach, D.; McKee, C.F. Molecule formation and infrared emission in fast interstellar shocks. I. Physical processes. *Astrophys. J. Suppl.* **1979**, *41*, 555–592.
174. Caimmi, R.; Secco, L. Evolution of galaxies—One-zone model with a birth-rate stellar function depending on gas density and temperature. *Astrophys. Space Sci.* **1986**, *119*, 315–336.
175. Theis, C.; Burkert, A.; Hensler, G. Chemo-dynamical evolution of massive spherical galaxies. *Astron. Astrophys.* **1992**, *265*, 465–477.
176. Hollenbach, D. Heating and cooling of molecular clouds and their surfaces. *Astrophys. Lett. Commun.* **1988**, *26*, 191–205.
177. Ikeuchi, S.; Ostriker, J.P. Evolution of the intergalactic medium—What happened during the epoch $Z = 3$–10? *Astrphys. J.* **1986**, *301*, 522–543.
178. Dyson, J.E.; Williams, D.A. *The Physics of the Interstellar Medium*, 2nd ed.; Dyson, J.E., Williams, D.A., Eds.; Series: The Graduate Series in Astronomy; Institute of Physics Publishing: Bristol, UK, 1997.
179. Thornton, K.; Gaudlitz, M.; Janka, H.-T.; Steinmetz, M. Energy Input and Mass Redistribution by Supernovae in the Interstellar Medium. *Astrophys. J.* **1998**, *500*, 95–119.

180. Cho, H.; Kang, H. Feedback from multiple supernova explosions inside a wind-blown bubble. *Nature* **2008**, *13*, 163–177.
181. Greggio, L.; Renzini, A. The binary model for type I supernovae—Theoretical rates. *Astron. Astrophys.* **1983**, *118*, 217–222.
182. Grassi, T.; Krstic, P.; Merlin, E.; Buonomo, U.; Piovan, L.; Chiosi, C. ROBO: A model and a code for studying the interstellar medium. *Astron. Astrophys.* **2011**, *533*, doi:10.1051/0004-6361/200913779.
183. Grassi, T.; Merlin, E.; Piovan, L.; Buonomo, U.; Chiosi, C. MaNN: Multiple Artificial Neural Networks for modelling the Interstellar Medium. *ArXiv E-Prints*, **2011**, arXiv:1103.0509.
184. Gallazzi, A.; Charlot, S.; Brinchmann, J.; White, S.D.M.; Tremonti, C.A. The ages and metallicities of galaxies in the local universe. *Mon. Not. R. Astron. Soc.* **2005**, *362*, 41–58.
185. Cappellari, M.; McDermid, R.M.; Alatalo, K.; Blitz, L.; Bois, M.; Bournaud, F.; Bureau, M.; Crocker, A.F.; Davies, R.L.; Davis, T.A.; *et al.* Systematic variation of the stellar initial mass function in early-type galaxies. *Nature* **2012**, *484*, 485–488.
186. Scodeggio, M. Internal Color Gradients and the Color-Magnitude Relation of Early-Type Galaxies. *Astron. J.* **2001**, *121*, 2413–2419.
187. La Barbera, F.; de Carvalho, R.R.; de la Rosa, I.G.; Gal, R.R.; Swindle, R.; Lopes, P.A.A. Spider. IV. Optical and Near-infrared Color Gradients in Early-type Galaxies: New Insight into Correlations with Galaxy Properties. *Astron. J.* **2010**, *140*, 1528–1556.
188. La Barbera, F.; Ferreras, I.; de Carvalho, R.R.; Lopes, P.A.A.; Pasquali, A.; de la Rosa, I.G.; de Lucia, G. On the Radial Stellar Content of Early-type Galaxies as a Function of Mass and Environment. *Astrophys. J. Lett.* **2011**, *740*, doi:10.1088/2041-8205/740/2/L41.
189. Spolaor, M.; Proctor, R.N.; Forbes, D.A.; Couch, W.J. The Mass-Metallicity Gradient Relation of Early-Type Galaxies. *Astrophys. J. Lett.* **2009**, *691*, 138–141.
190. Chiosi, C. Gas and iron content of galaxy clusters. *Astron. Astrophys.* **2000**, *364*, 423–442.
191. Moretti, A.; Portinari, L.; Chiosi, C. Chemical evolution of the intra-cluster medium. *Astron. Astrophys.* **2003**, *408*, 431–453.
192. Sersic, J.L. *Atlas de Galaxias Australes*; Observatorio Astronomico: Cordoba, Argentina, 1968.
193. Hernquist, L. An analytical model for spherical galaxies and bulges. *Astrophys. J.* **1990**, *356*, 359–364.
194. Caon, N.; Capaccioli, M.; D'Onofrio, M. On the Shape of the Light Profiles of Early Type Galaxies. *Mon. Not. R. Astron. Soc.* **1993**, *265*, 1013–1021.
195. Ferrarese, L.; Côté, P.; Jordán, A.; Peng, E.W.; Blakeslee, J.P.; Piatek, S.; Mei, S.; Merritt, D.; Milosavljević, M.; Tonry, J.L.; *et al.* The ACS Virgo Cluster Survey. VI. Isophotal Analysis and the Structure of Early-Type Galaxies. *Astrophys. J. Suppl.* **2006**, *164*, 334–434.
196. Navarro, J.F.; Frenk, C.S.; White, S.D.M. The structure of cold dark matter haloes. *Astrophys. J* **1996**, *462*, doi:10.1086/177173.
197. Padmanabhan, N.; Seljak, U.; Strauss, M.A.; Blanton, M.R.; Kauffmann, G.; Schlegel, D.J.; Tremonti, C.; Bahcall, N.A.; Bernardi, M.; Brinkmann, J.; *et al.* Stellar and dynamical masses of ellipticals in the Sloan Digital Sky Survey. *New Astron.* **2004**, *9*, 329–342.

198. Bertin, G.; Liseikina, T.; Pegoraro, A. Slow evolution of elliptical galaxies induced by dynamical friction. I. Capture of a system of satellites. *Astron. Astrophys.* **2003**, *405*, 73–88.
199. Gnedin, O.Y.; Kravtsov, A.V.; Klypin, A.A.; Nagai, D. Response of Dark Matter Halos to Condensation of Baryons: Cosmological Simulations and Improved Adiabatic Contraction Model. *Astrophys. J.* **2004**, *616*, 16–26.
200. Côté, P.; Ferrarese, L.; Jordán, A.; Blakeslee, J.P.; Chen, C.-W.; Infante, L.; Merritt, D.; Mei, S.; Peng, E.W.; Tonry, J.L.; *et al.* The ACS Fornax Cluster Survey. II. The Central Brightness Profiles of Early-Type Galaxies: A Characteristic Radius on Nuclear Scales and the Transition from Central Luminosity Deficit to Excess. *Astrophys. J.* **2007**, *671*, 1456–1465.
201. Carraro, G.; Chiosi, C.; Girardi, L.; Lia, C. Dwarf elliptical galaxies: Structure, star formation and colour-magnitude diagrams. *Mon. Not. R. Astron. Soc.* **2001**, *327*, 69–79.
202. Pasetto, S.; Chiosi, C.; Carraro, G. Morphological evolution of dwarf galaxies in the Local Group. *Astron. Astrophys.* **2003**, *405*, 931–949.
203. Pasetto, S.; Grebel, E.K.; Berczik, P.; Chiosi, C.; Spurzem, R. Orbital evolution of the Carina dwarf galaxy and self-consistent determination of star formation history. *Astron. Astrophys.* **2011**, *525*, doi:10.1051/0004-6361/200913415.
204. Magorrian, J.; Tremaine, S.; Richstone, D.; Bender, R.; Bower, G.; Dressler, A.; Faber, S.M.; Gebhardt, K.; Green, R.; Grillmair, C.; *et al.* The Demography of Massive Dark Objects in Galaxy Centers. *Astron. J.* **1998**, *115*, 2285–2305.
205. Ferrarese, L.; Merritt, D. A Fundamental Relation between Supermassive Black Holes and Their Host Galaxies. *Astrophys. J. Lett.* **2000**, *539*, 9–12.
206. Powell, L.C.; Slyz, A.; Devriendt, J. The impact of supernova-driven winds on stream-fed protogalaxies. *Mon. Not. R. Astron. Soc.* **2011**, *414*, 3671–3689.
207. Fabian, A.C. Observational Evidence of Active Galactic Nuclei Feedback. *Annu. Rev. Astron. Astrophys.* **2012**, *50*, 455–489.
208. Croton, D.J.; Springel, V.; White, S.D.M.; de Lucia, G.; Frenk, C.S.; Gao, L.; Jenkins, A.; Kauffmann, G.; Navarro, J.F.; Yoshida, N. The many lives of active galactic nuclei: Cooling flows, black holes and the luminosities and colours of galaxies. *Mon. Not. R. Astron. Soc.* **2006**, *365*, 11–28.
209. Bower, R.G.; Benson, A.J.; Malbon, R.; Helly, J.C.; Frenk, C.S.; Baugh, C.M.; Cole, S.; Lacey, C.G. Breaking the hierarchy of galaxy formation. *Mon. Not. R. Astron. Soc.* **2006**, *370*, 645–655.
210. Cattaneo, A.; Dekel, A.; Devriendt, J.; Guiderdoni, B.; Blaizot, J. Modelling the galaxy bimodality: Shutdown above a critical halo mass. *Mon. Not. R. Astron. Soc.* **2006**, *370*, 1651–1665.
211. Somerville, R.S.; Hopkins, P.F.; Cox, T.J.; Robertson, B.E.; Hernquist, L. A semi-analytic model for the co-evolution of galaxies, black holes and active galactic nuclei. *Mon. Not. R. Astron. Soc.* **2008**, *391*, 481–506.
212. Bell, E.F.; Baugh, C.M.; Cole, S.; Frenk, C.S.; Lacey, C.G. The properties of spiral galaxies: Confronting hierarchical galaxy formation models with observations. *Mon. Not. R. Astron. Soc.* **2003**, *343*, 367–384.

213. Panter, B.; Jimenez, R.; Heavens, A.F.; Charlot, S. The star formation histories of galaxies in the Sloan Digital Sky Survey. *Mon. Not. R. Astron. Soc.* **2007**, *378*, 1550–1564.
214. Tremonti, C.A.; Heckman, T.M.; Kauffmann, G.; Brinchmann, J.; Charlot, S.; White, S.D.M.; Seibert, M.; Peng, E.W.; Schlegel, D.J.; Uomoto, A.; *et al.* The Origin of the Mass-Metallicity Relation: Insights from 53,000 Star-forming Galaxies in the Sloan Digital Sky Survey. *Astrophys. J.* **2004**, *613*, 898–913.
215. Woosley, S.E.; Heger, A.; Weaver, T.A. The evolution and explosion of massive stars. *Rev. Mod. Phys.* **2002**, *74*, 1015–1071.
216. Begelman, M.C.; Volonteri, M.; Rees, M.J. Formation of supermassive black holes by direct collapse in pre-galactic haloes. *Mon. Not. R. Astron. Soc.* **2006**, *370*, 289–298.
217. Spitzer, L. *Dynamical Evolution of Globular Clusters*; Princeton University Press: Princeton, NJ, USA, 1987; p. 191.
218. Bromm, V.; Larson, R.B. The First Stars. *Annu. Rev. Astron. Astrophys.* **2004**, *42*, 79–118.
219. Winter, L.M.; Mushotzky, R.F.; Reynolds, C.S. XMM-Newton Archival Study of the Ultraluminous X-Ray Population in Nearby Galaxies. *Astrophys. J.* **2006**, *649*, 730–752.
220. Kaviraj, S.; Schawinski, K.; Devriendt, J.E.G.; Ferreras, I.; Khochfar, S.; Yoon, S.-J.; Yi, S.K.; Deharveng, J.-M.; Boselli, A.; Barlow, T.; *et al.* UV-Optical Colors As Probes of Early-Type Galaxy Evolution. *Astrophys. J. Suppl.* **2007**, *173*, 619–642.
221. Gnedin, O.Y. On the origin of globular cluster bimodality. In Proceedings of the IAU Symposium 266, Rio de Janeiro, Brazil, 10–14 August 2010; de Grijs, R., Lépine, J.R.D., Eds.; pp. 250–257.
222. Muratov, A.L.; Gnedin, O.Y. Modeling the Metallicity Distribution of Globular Clusters. *Astrophys. J.* **2010**, *718*, 1266–1288.
223. Mancini, C.; Matute, I.; Cimatti, A.; Daddi, E.; Dickinson, M.; Rodighiero, G.; Bolzonella, M.; Pozzetti, L. Searching for massive galaxies at $z \geq 3.5$ in GOODS-North. *Astron. Astrophys.* **2009**, *500*, 705–723.
224. Valentinuzzi, T.; Fritz, J.; Poggianti, B.M.; Cava, A.; Bettoni, D.; Fasano, G.; D'Onofrio, M.; Couch, W.J.; Dressler, A.; Moles, M.; *et al.* Superdense Massive Galaxies in Wings Local Clusters. *Astrophys. J.* **2010**, *712*, 226–237.
225. Karim, A.; Schinnerer, E.; Martínez-Sansigre, A.; Sargent, M.T.; van der Wel, A.; Rix, H.-W.; Ilbert, O.; Smolčić, V.; Carilli, C.; Pannella, M.; *et al.* The Star Formation History of Mass-selected Galaxies in the COSMOS Field. *Astrophys. J.* **2011**, *730*, doi:10.1088/0004-637X/730/2/61.
226. Chiosi, C.; Merlin, E.; Piovan, L. The origin of the mass-radius relation of early-type galaxies. *ArXiv E-Prints*, **2012**, arXiv:1206.2532.
227. Bernardi, M.; Shankar, F.; Hyde, J.B.; Mei, S.; Marulli, F.; Sheth, R.K. Galaxy luminosities, stellar masses, sizes, velocity dispersions as a function of morphological type. *Mon. Not. R. Astron. Soc.* **2010**, *404*, 2087–2122.
228. Shen, S.; Mo, H.J.; White, S.D.M.; Blanton, M.R.; Kauffmann, G.; Voges, W.; Brinkmann, J.; Csabai, I. The size distribution of galaxies in the Sloan Digital Sky Survey. *Mon. Not. R. Astron. Soc.* **2003**, *343*, 978–994.

229. Guo, Y.; McIntosh, D.H.; Mo, H.J.; Katz, N.; van den Bosch, F.C.; Weinberg, M.; Weinmann, S.M.; Pasquali, A.; Yang, X. Structural properties of central galaxies in groups and clusters. *Mon. Not. R. Astron. Soc.* **2009**, *398*, 1129–1149.
230. Van Dokkum, P.G.; Whitaker, K.E.; Brammer, G.; Franx, M.; Kriek, M.; Labbé, I.; Marchesini, D.; Quadri, R.; Bezanson, R.; Illingworth, G.D.; *et al.* The Growth of Massive Galaxies Since $z = 2$. *Astrophys. J.* **2010**, *709*, 1018–1041.
231. Woo, J.; Courteau, S.; Dekel, A. Scaling relations and the fundamental line of the local group dwarf galaxies. *Mon. Not. R. Astron. Soc.* **2008**, *390*, 1453–1469.
232. Fan, L.; Lapi, A.; Bressan, A.; Bernardi, M.; de Zotti, G.; Danese, L. Cosmic Evolution of Size and Velocity Dispersion for Early-Type Galaxies. *Astrophys. J.* **2010**, *718*, 1460–1475.
233. Gott, J.R., III; Rees, M.J. A theory of galaxy formation and clustering. *Astron. Astrophys.* **1975**, *45*, 365–376.
234. Blumenthal, G.R.; Faber, S.M.; Primack, J.R.; Rees, M.J. Formation of galaxies and large-scale structure with cold dark matter. *Nature* **1984**, *311*, 517–525.
235. Girardi, L.; Bressan, A.; Bertelli, G.; Chiosi, C. Evolutionary tracks and isochrones for low- and intermediate-mass stars: From 0.15 to 7 M_{sun}, and from $Z = 0.0004$ to 0.03. *Astron. Astrophys. Suppl.* **2000**, *141*, 371–383.
236. Girardi, L.; Bertelli, G.; Bressan, A.; Chiosi, C.; Groenewegen, M.A.T.; Marigo, P.; Salasnich, B.; Weiss, A. Theoretical Isochrones in Several Photometric Systems. I. Johnson-Cousins-Glass, HST/WFPC2, HST/NICMOS, Washington, and ESO Imaging Survey Filter Sets. *Astron. Astrophys.* **2002**, *391*, 195–212.
237. Tantalo, R.; Chinellato, S.; Merlin, E.; Piovan, L.; Chiosi, C. Formation and evolution of early-type galaxies: Spectro-photometry from cosmo-chemo-dynamical simulations. *Astron. Astrophys.* **2010**, *518*, doi:10.1051/0004-6361/200912709.
238. Guiderdoni, B.; Rocca-Volmerange, B. A model of spectrophotometric evolution for high-redshift galaxies. *Astron. Astrophys.* **1987**, *186*, 1–21.
239. Guiderdoni, B.; Rocca-Volmerange, B. Apparent magnitudes of high-redshift galaxies in UBVRI and space telescope photometric systems. *Astron. Astrophys. Suppl.* **1988**, *74*, 185–210,
240. Rocca-Volmerange, B.; Guiderdoni, B. Star formation in nuclei of S0/E galaxies. *Astron. Astrophys.* **1987**, *175*, 15–22.
241. Rocca-Volmerange, B.; Guiderdoni, B. An atlas of synthetic spectra of galaxies. *Astron. Astrophys. Suppl.* **1988**, *75*, 93–106.
242. Rocca-Volmerange, B. An evolutionary model of star formation for elliptical galaxies. *Mon. Not. R. Astron. Soc.* **1989**, *236*, 47–56.
243. Hubble, E. Effects of Red Shifts on the Distribution of Nebulae. *Proc. Natl. Acad. Sci. USA* **1936**, *22*, 621–627.
244. Weinberg, S. *Gravitation and Cosmology: Principles and Applications of the General Theory of Relativity*; John Wiley & Sons: Hoboken, NJ, USA, 1972; p. 688.
245. Hogg, D.W. Distance measures in cosmology. *ArXiv E-Prints*, **1999**, arXiv:astro-ph:9905116.
246. Kolb, E.W.; Turner, M.S. The pocket cosmology. *Eur. Phys. J. C* **2000**, *15*, 125–132.

247. Oke, J.B.; Sandage, A. Energy Distributions, K Corrections, and the Stebbins-Whitford Effect for Giant Elliptical Galaxies. *Astrophys. J.* **1968**, *154*, 21–32.
248. Piovan, L.; Tantalo, R.; Chiosi, C. Shells of dust around AGB stars: Effects on the integrated spectrum of Single Stellar Populations. *Astron. Astrophys.* **2003**, *408*, 559–579.
249. Piovan, L.; Tantalo, R.; Chiosi, C. Modelling galaxy spectra in presence of interstellar dust—I. The model of interstellar medium and the library of dusty single stellar populations. *Mon. Not. R. Astron. Soc.* **2006**, *366*, 923–944.
250. Piovan, L.; Tantalo, R.; Chiosi, C. Modelling galaxy spectra in presence of interstellar dust—II. From the ultraviolet to the far-infrared. *Mon. Not. R. Astron. Soc.* **2006**, *370*, 1454–1478.
251. Piovan, L.; Chiosi, C.; Merlin, E.; Grassi, T.; Tantalo, R.; Buonomo, U.; Cassarà, L.P. Formation and Evolution of the Dust in Galaxies. I. The Condensation Efficiencies. *ArXiv E-Prints*, **2011**, arXiv:1107.4541.
252. Piovan, L.; Chiosi, C.; Merlin, E.; Grassi, T.; Tantalo, R.; Buonomo, U.; Cassarà, L.P. Formation and Evolution of the Dust in Galaxies. II. The Solar Neighbourhood. *ArXiv E-Prints*, **2011**, arXiv:1107.4561.
253. Piovan, L.; Chiosi, C.; Merlin, E.; Grassi, T.; Tantalo, R.; Buonomo, U.; Cassarà, L.P. Formation and Evolution of the Dust in Galaxies. III. The Disk of the Milky Way. *ArXiv E-Prints*, **2011**, arXiv:1107.4567.
254. Draine, B.T.; Lee, H.M. Optical properties of interstellar graphite and silicate grains. *Astrophys. J.* **1984**, *285*, 89–108.
255. Cardelli, J.A.; Clayton, G.C.; Mathis, J.S. The relationship between infrared, optical, and ultraviolet extinction. *Astrophys. J.* **1989**, *345*, 245–256.
256. Steidel, C.C.; Giavalisco, M.; Dickinson, M.; Adelberger, K.L. Spectroscopy of Lyman Break Galaxies in the Hubble Deep Field. *Astron. J.* **1996**, *112*, doi:10.1086/118019.
257. Steidel, C.C.; Adelberger, K.L.; Shapley, A.E.; Pettini, M.; Dickinson, M.; Giavalisco, M. Lyman Break Galaxies at Redshift $z \sim 3$: Survey Description and Full Data Set. *Astrophys. J.* **2003**, *592*, 728–754.
258. Scoville, N.; Aussel, H.; Benson, A.; Blain, A.; Calzetti, D.; Capak, P.; Ellis, R.S.; El-Zant, A.; Finoguenov, A.; Giavalisco, M.; *et al.* Large Structures and Galaxy Evolution in COSMOS at $z < 1.1$. *Astrophys. J. Suppl.* **2007**, *172*, 150–181.
259. Giavalisco, M.; Dickinson, M.; Ferguson, H.C.; Ravindranath, S.; Kretchmer, C.; Moustakas, L.A.; Madau, P.; Fall, S.M.; Gardner, J.P.; Livio, M.; *et al.* The Rest-Frame Ultraviolet Luminosity Density of Star-forming Galaxies at Redshifts $z \geq 3.5$. *Astrophys. J. Lett.* **2004**, *600*, 103–106.
260. Capak, P.; Aussel, H.; Ajiki, M.; McCracken, H.J.; Mobasher, B.; Scoville, N.; Shopbell, P.; Taniguchi, Y.; Thompson, D.; Tribiano, S.; *et al.* The First Release COSMOS Optical and Near-IR Data and Catalog. *Astrophys. J. Suppl.* **2007**, *172*, 99–116.
261. Mobasher, B.; Capak, P.; Scoville, N.Z.; Dahlen, T.; Salvato, M.; Aussel, H.; Thompson, D.J.; Feldmann, R.; Tasca, L.; le Fevre, O. Photometric Redshifts of Galaxies in COSMOS. *Astrophys. J. Suppl.* **2007**, *172*, 117–131.

262. Grazian, A.; Fontana, A.; de Santis, C.; Nonino, M.; Salimbeni, S.; Giallongo, E.; Cristiani, S.; Gallozzi, S. Vanzella, E. The GOODS-MUSIC sample: A multicolour catalog of near-IR selected galaxies in the GOODS-South field. *Astron. Astrophys.* **2006**, *449*, 951–968.
263. Kormendy, J. Brightness distributions in compact and normal galaxies. II—Structure parameters of the spheroidal component. *Astrophys. J.* **1977**, *218*, 333–346.
264. Hamabe, M.; Kormendy, J. Correlations Between R/1/4—Law Parameters for Bulges and Elliptical Galaxies. In *IAU Symposium 127, Structure and Dynamics of Elliptical Galaxies*; de Zeeuw, T., Ed.; Reidel: Dordrecht, The Netherlands, 1987; p. 379.
265. Aragon-Salamanca, A.; Ellis, R.S.; Couch, W.J.; Carter, D. Evidence for systematic evolution in the properties of galaxies in distant clusters. *Mon. Not. R. Astron. Soc.* **1993**, *262*, 764–794.
266. Bender, R.; Ziegler, B.; Bruzual, G. The Redshift Evolution of the Stellar Populations in Elliptical Galaxies. *Astrophys. J. Lett.* **1996**, *463*, doi:10.1086/310071.
267. Van Dokkum, P.G.; Franx, M. The Fundamental Plane in CL 0024 at $z \sim 0.4$: Implications for the evolution of the mass-to-light ratio. *Mon. Not. R. Astron. Soc.* **1996**, *281*, 985–1000.
268. Jorgensen, I.; Hjorth, J. The Fundamental Plane at $z = 0.18$. In *Galaxy Scaling Relations: Origins, Evolution and Applications*; da Costa, L.N., Renzini, A., Eds.; Springer: Berlin, Germany, 1997; p. 175.
269. Ziegler, B.L.; Bender, R. The Mg_b-σ relation of elliptical galaxies at $z \approx 0.37$. *Mon. Not. R. Astron. Soc.* **1997**, *291*, 527–543.
270. Bender, R.; Saglia, R.P.; Ziegler, B.; Belloni, P.; Greggio, L.; Hopp, U.; Bruzual, G. Exploring Cluster Elliptical Galaxies as Cosmological Standard Rods. *Astrophys. J.* **1998**, *493*, doi:10.1086/305166.
271. Van Dokkum, P.G.; Franx, M.; Kelson, D.D.; Illingworth, G.D. Luminosity Evolution of Early-Type Galaxies to $z \sim 0.83$: Constraints on Formation Epoch and Omega. *Astrophys. J. Lett.* **1998**, *504*, doi:10.1086/311567.
272. White, S.D.M.; Rees, M.J. Core condensation in heavy halos—A two-stage theory for galaxy formation and clustering. *Mon. Not. R. Astron. Soc.* **1978**, *183*, 341–358.
273. La Barbera, F.; Busarello, G.; Merluzzi, P.; Massarotti, M.; Capaccioli, M. On the Invariant Distribution of Galaxies in the $r_e - \mu_e$ Plane out to $z \sim 0.64$. *Astrophys. J.* **2003**, *595*, 127–136.
274. Bernardi, M.; Sheth, R.K.; Annis, J.; Burles, S.; Eisenstein, D.J.; Finkbeiner, D.P.; Hogg, D.W.; Lupton, R.H.; Schlegel, D.J.; SubbaRao, M.; *et al.* Early-Type Galaxies in the Sloan Digital Sky Survey. II. Correlations between Observables. *Astron. J.* **2003**, *125*, 1849–1865.
275. Bernardi, M.; Sheth, R.K.; Annis, J.; Burles, S.; Eisenstein, D.J.; Finkbeiner, D.P.; Hogg, D.W.; Lupton, R.H.; Schlegel, D.J.; SubbaRao, M.; *et al.* Early-Type Galaxies in the Sloan Digital Sky Survey. I. The Sample. *Astron. J.* **2003**, *125*, 1817–1848.
276. York, D.G.; Adelman, J.; Anderson, J.E., Jr.; Anderson, S.F.; Annis, J.; Bahcall, N.A.; Bakken, J.A.; Barkhouser, R.; Bastian, S.; Berman, E.; *et al.* The Sloan Digital Sky Survey: Technical Summary. *Astron. J.* **2000**, *120*, 1579–1587.
277. Stoughton, C.; Lupton, R.H.; Bernardi, M.; Blanton, M.R.; Burles, S.; Castander, F.J.; Connolly, A.J.; Eisenstein, D.J.; Frieman, J.A.; Hennessy, G.S.; *et al.* Sloan Digital Sky Survey: Early Data Release. *Astron. J.* **2002**, *123*, 485–548.

278. Bernardi, M.; Sheth, R.K.; Annis, J.; Burles, S.; Eisenstein, D.J.; Finkbeiner, D.P.; Hogg, D.W.; Lupton, R.H.; Schlegel, D.J.; SubbaRao, M.; *et al.* Early-Type Galaxies in the Sloan Digital Sky Survey. III. The Fundamental Plane. *Astron. J.* **2003**, *125*, 1866–1881.

© 2014 by the authors; licensee MDPI, Basel, Switzerland. This article is an open access article distributed under the terms and conditions of the Creative Commons Attribution license (http://creativecommons.org/licenses/by/3.0/).